

HYDRODYNAMIC LUBRICATION THEORY IN  
ROTATING DISK CLUTCHES

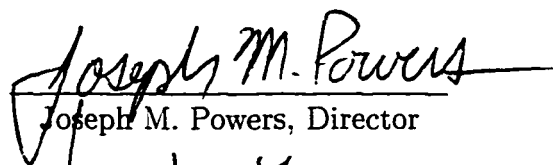
A Dissertation

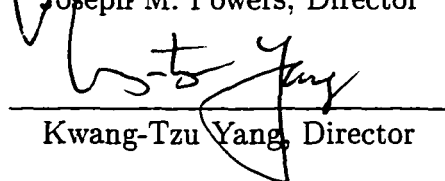
Submitted to the Graduate School  
of the University of Notre Dame  
In Partial Fulfillment of the Requirements  
for the Degree of

Doctor of Philosophy

by

Andrew M. Smith, B.S., M.S.

  
Joseph M. Powers, Director

  
Kwang-Tzu Yang, Director

Department of Aerospace and Mechanical Engineering

Notre Dame, Indiana

April 1997

**UMI Number: 9722365**

---

**UMI Microform 9722365**  
**Copyright 1997, by UMI Company. All rights reserved.**

**This microform edition is protected against unauthorized  
copying under Title 17, United States Code.**

---

**UMI**  
**300 North Zeeb Road**  
**Ann Arbor, MI 48103**

# HYDRODYNAMIC LUBRICATION THEORY IN ROTATING DISK CLUTCHES

Abstract

by

Andrew M. Smith

This dissertation is concerned with modeling the friction, load capacity, and temperature rise between a pair of rotating disk clutch plates using a hydrodynamic lubrication model. The lubricating film possesses a temperature dependent viscosity which significantly affects overall clutch performance. The model can accommodate an arbitrary film shape. The governing mass, momentum, and energy equations are simplified using the assumptions of incompressibility, negligible body forces, and a thin-film assumption. Velocity, pressure, and temperature profiles are obtained using a marker and cell method and a three-level fully implicit method. These methods were verified by comparing numerical results to analytical solutions obtained in limiting cases in which exact solutions exist. Results are presented for (1) the case of a sinusoidally varying film thickness, (2) the constant film thickness case, (3) groove studies, and (4) a conjugate heat transfer problem. As expected for hydrodynamic theory, the results indicate that predicted friction coefficients ( $\mu_F \approx 0.005 - 0.03$ ) are nearly an order of magnitude below typical clutch operating conditions ( $\mu_F \approx 0.1 - 0.3$ ). A limited set of results indicates that, for the constant film case, spatial gradients in viscosity may be neglected if the bulk viscosity is chosen to satisfy the viscosity-temperature relation using the average temperature. Both the viscosity-temperature relation and film size have a significant effect on clutch performance.

## Dedication

This dissertation is dedicated to my parents, Mike and Mary, who taught me the values of diligence and patience.

# TABLE OF CONTENTS

<b>LIST OF FIGURES</b>	<b>vi</b>
<b>LIST OF TABLES</b>	<b>ix</b>
<b>LIST OF SYMBOLS</b>	<b>x</b>
<b>ACKNOWLEDGMENTS</b>	<b>xv</b>
<b>1 INTRODUCTION</b>	<b>1</b>
1.1 Description of Clutch Operation . . . . .	1
1.2 Overview of Current Research . . . . .	3
1.3 Utility of the Research . . . . .	8
1.4 New Contributions . . . . .	11
<b>2 LITERATURE REVIEW</b>	<b>14</b>
2.1 Clutch Studies . . . . .	14
2.1.1 Theoretical Models . . . . .	15
2.1.2 Experimental Investigations . . . . .	17
2.2 Related Mechanical Devices . . . . .	18
2.3 Tribological Issues . . . . .	19
2.3.1 Mineral Oil Rheology . . . . .	19
2.3.2 Surface Topography . . . . .	24
2.4 Related Fluid Mechanics and Heat Transfer Problems . . . . .	26
<b>3 MATHEMATICAL MODEL</b>	<b>28</b>
3.1 Domain and Variable Definitions . . . . .	28
3.2 Conservation Principles . . . . .	31
3.3 Constitutive Equations . . . . .	33
3.4 Initial and Boundary Conditions . . . . .	36
3.5 Non-Dimensionalization . . . . .	38

3.5.1	Choice of Scaling . . . . .	38
3.5.2	Dimensionless Equations . . . . .	40
3.5.3	Simplifications . . . . .	43
3.6	Summarized Problem Statement . . . . .	46
3.7	Algebraic Coordinate Transformation . . . . .	49
3.8	Clutch Performance Parameters . . . . .	52
3.8.1	Radial Volumetric Flow Rate . . . . .	53
3.8.2	Normal Load . . . . .	53
3.8.3	Tangential Forces . . . . .	54
3.8.4	Frictional Moment Delivered . . . . .	55
3.8.5	Friction Coefficient . . . . .	56
<b>4</b>	<b>NUMERICAL SOLUTION METHOD</b>	<b>57</b>
4.1	Staggered Grid . . . . .	57
4.2	Discretized Equations . . . . .	59
4.2.1	Discrete Radial and Angular Momentum . . . . .	60
4.2.2	Discrete Poisson Pressure Equation . . . . .	62
4.2.3	Discrete Axial Velocity Equation . . . . .	66
4.2.4	Discrete Energy Equation . . . . .	69
4.3	Algorithm Summary . . . . .	72
4.4	Treatment of Clutch Performance Parameters . . . . .	74
4.5	Numerical Verification . . . . .	75
4.5.1	Isoviscous Axisymmetric Solutions . . . . .	75
4.5.2	Isoviscous, Radially Grooved Solution . . . . .	81
<b>5</b>	<b>RESULTS</b>	<b>87</b>
5.1	Model Solution for a Sinusoidally Varying Film Thickness . . . . .	87
5.2	Effects of Variable Viscosity on the Constant Film Thickness Case . . . . .	91
5.3	Groove Studies . . . . .	109
5.3.1	Cavitation Studies . . . . .	110
5.3.2	Non-Cavitation Studies . . . . .	113
5.4	Multiple Disk Solutions . . . . .	116

<b>6 CONCLUSIONS AND RECOMMENDATIONS</b>	<b>131</b>
6.1 Discussion of Results . . . . .	131
6.2 Recommendations . . . . .	134
6.2.1 Recommendations in Experimental Studies . . . . .	135
6.2.2 Recommendations in Theoretical Studies . . . . .	136
6.2.3 Boundary and Mixed Film Lubrication Models . . . . .	138
<b>APPENDIX A</b>	<b>141</b>
<b>APPENDIX B</b>	<b>143</b>
<b>APPENDIX C</b>	<b>145</b>
<b>BIBLIOGRAPHY</b>	<b>149</b>

## LIST OF FIGURES

1.1	Simplified Clutch Schematic . . . . .	2
1.2	Simplified Clutch Schematic with Lubrication . . . . .	3
1.3	Thermal Model Schematic . . . . .	5
1.4	Fluid Model Schematic . . . . .	6
1.5	Conjugate Problem Schematic . . . . .	13
3.1	Lubrication Problem Domain . . . . .	29
3.2	Thermal Problem Domain . . . . .	31
3.3	Viscosity-Temperature Relation for Seven SAE Oils . . . . .	35
4.1	Staggered Grid . . . . .	58
4.2	Numerical and Analytical Pressure Profiles . . . . .	77
4.3	(a) Numerical and (b) Analytical Radial Velocity Profiles . . . . .	78
4.4	(a) Numerical and (b) Analytical Angular Velocity Profiles . . . . .	78
4.5	(a) Numerical and (b) Analytical Axial Velocity Profiles . . . . .	79
4.6	Error Analysis for Isoviscous Axisymmetric Check Case . . . . .	79
4.7	(a) Numerical and (b) Analytical Pressure Profiles using $N_r = N_\theta = 125$ . . . . .	84
4.8	Error Analysis for Isoviscous Radially Grooved Case . . . . .	85
5.1	Film thickness profile from Equation 5.2, using $N_r = 49$ , $N_\theta = 49$ , $R_* = 1.3$ , $\theta_o = 0.1$ , and $h_{g\theta}^* = 1.0$ . . . . .	88
5.2	Pressure Profile . . . . .	89
5.3	Radial Velocity Profiles at $\theta_* =$ (a) 0, (b) $\frac{\theta_o}{4}$ , (c) $\frac{\theta_o}{2}$ , and (d) $\frac{3\theta_o}{4}$ . . . . .	90
5.4	Angular Velocity Profiles at $\theta_* =$ (a) 0, (b) $\frac{\theta_o}{4}$ , (c) $\frac{\theta_o}{2}$ , and (d) $\frac{3\theta_o}{4}$ . . . . .	97
5.5	Axial Velocity Profiles at $\theta_* =$ (a) 0, (b) $\frac{\theta_o}{4}$ , (c) $\frac{\theta_o}{2}$ , and (d) $\frac{3\theta_o}{4}$ . . . . .	98
5.6	Temperature Profiles at $\theta_* =$ (a) 0, (b) $\frac{\theta_o}{4}$ , (c) $\frac{\theta_o}{2}$ , and (d) $\frac{3\theta_o}{4}$ . . . . .	99
5.7	Variation of Flow Rate with Outlet Pressure . . . . .	100
5.8	Variation of Normal Force with Outlet Pressure . . . . .	100
5.9	Variation of Tangential Force with Outlet Pressure . . . . .	100
5.10	Variation of Friction Torque with Outlet Pressure . . . . .	101



5.11	Variation of Friction Coefficient with Outlet Pressure . . . . .	101
5.12	Variation of Temperature Rise with Outlet Pressure . . . . .	101
5.13	Variation of Flow Rate with Inlet Temperature . . . . .	102
5.14	Variation of Normal Force with Inlet Temperature . . . . .	102
5.15	Variation of Tangential Force with Inlet Temperature . . . . .	102
5.16	Variation of Friction Torque with Inlet Temperature . . . . .	103
5.17	Variation of Friction Coefficient with Inlet Temperature . . . . .	103
5.18	Variation of Temperature Rise with Inlet Temperature . . . . .	103
5.19	Variation of Flow Rate with Relative Angular Velocity . . . . .	104
5.20	Variation of Normal Force with Relative Angular Velocity . . . . .	104
5.21	Variation of Tangential Force with Relative Angular Velocity . . . . .	104
5.22	Variation of Friction Torque with Relative Angular Velocity . . . . .	105
5.23	Variation of Friction Coefficient with Relative Angular Velocity . . . . .	106
5.24	Variation of Temperature Rise with Relative Angular Velocity . . . . .	106
5.25	Variable and Constant Viscosity Pressure Profiles . . . . .	107
5.26	(a) Variable and (b) Constant Viscosity Radial Velocity Profiles . . . . .	107
5.27	(a) Variable and (b) Constant Viscosity Angular Velocity Profiles . . . . .	108
5.28	(a) Variable and (b) Constant Temperature Profiles . . . . .	108
5.29	(a) Film Thickness Schematic in $\theta_* - z_*$ plane and (b) Film Thickness with $\chi_1 = 0.4$ , $\chi_2 = 0.2$ , $R_* = 1.3$ , $\theta_o = 0.1 \text{ rad}$ , $h_g^* = 3.5$ . . . . .	110
5.30	(a) Typical Pressure Distribution and (b) Pressure Contours. (Using $S = 968.72$ and $h_g^* = 3.5$ .) . . . . .	112
5.31	Zones of Cavitation and No Cavitation . . . . .	114
5.32	Maximum Pressure vs. Groove Depth . . . . .	114
5.33	Normal Load vs. Groove Depth and Sommerfeld Number . . . . .	115
5.34	Normal Load vs. Groove Depth using Variable and Constant Viscosity . . . . .	115
5.35	Velocity Vectors at Average Clutch Radius . . . . .	116
5.36	Multiple Disk Clutch Conjugate Model Schematic . . . . .	117
5.37	Comparison Between Numerical and Analytical Assembly Temperature Distributions at $r = R_o$ using constant viscosity, $\frac{p_i}{p_o} = 1$ , and $\frac{h_2}{h_o} = 0$ . . . . .	123

5.38	Numerical Assembly Temperature Distributions at $r = R_o$ with constant viscosity, $\frac{\rho_i}{\rho_o} = 2$ , and $\frac{h_g}{h_o} = 0$ . . . . .	124
5.39	Numerical Assembly Temperature Distributions at $r = R_o$ and $\theta = 0$ with constant viscosity, $\frac{\rho_i}{\rho_o} = 2$ , and $\frac{h_g}{h_o} = 0.5$ . . . . .	125
5.40	Numerical Assembly Temperature Distributions at $r = R_o$ with variable viscosity, $\frac{\rho_i}{\rho_o} = 2$ , and $\frac{h_g}{h_o} = 0$ . . . . .	126
5.41	Numerical Assembly Temperature Distributions at $r = R_o$ and $\theta = 0$ with variable viscosity, $\frac{\rho_i}{\rho_o} = 2$ , and $\frac{h_g}{h_o} = 0.5$ . . . . .	130

## LIST OF TABLES

1.1	LUBRICATION REGIMES ( $\Lambda = \frac{\text{FILM THICKNESS}}{\text{SURFACE ROUGHNESS}}$ ) . . . . .	10
3.1	RESULTS FROM FITTING SHIGLEY'S DATA INTO WALTHERS'S EQUATION . . . . .	34
3.2	TYPICAL CLUTCH OPERATING CONDITIONS . . . . .	43
3.3	RANGE OF PARAMETERS STUDIED . . . . .	44
3.4	TYPICAL CLUTCH DIMENSIONLESS PARAMETERS . . . . .	44
3.5	RANGE OF DIMENSIONLESS PARAMETERS STUDIED . . . . .	44
5.1	CONSTANT PARAMETERS FOR RESULTS PRESENTED IN SECTION 5.1 . . . . .	89
5.2	CONSTANT PARAMETERS FOR RESULTS PRESENTED IN SECTION 5.2 . . . . .	92
5.3	MAXIMUM VALUES OF TERMS IN DIMENSIONLESS ENERGY EQUATION . . . . .	95
5.4	COMPARISON BETWEEN CONSTANT AND VARIABLE VISCOSITY PREDICTIONS FOR THE CONSTANT FILM CASE (CV: CONSTANT VISCOSITY BASED ON AVERAGE TEMPERATURE PREDICTED THROUGHOUT DOMAIN, VV: WORKING VARIABLE VISCOSITY MODEL) . . . . .	127
5.5	CONSTANT PARAMETERS FOR RESULTS PRESENTED IN SECTION 5.3.1 . . . . .	128
5.6	CONSTANT PARAMETERS FOR RESULTS PRESENTED IN SECTION 5.3.2 . . . . .	128
5.7	RESULTS FOR SECTION 5.3.2 (VV - VARIABLE VISCOSITY, CV - CONSTANT VISCOSITY) . . . . .	129
5.8	CONSTANT PARAMETERS FOR RESULTS PRESENTED IN SECTION 5.4 . . . . .	129
5.9	SUMMARY OF CLUTCH PERFORMANCE (VV - VARIABLE VISCOSITY, CV - CONSTANT VISCOSITY) . . . . .	130

## LIST OF SYMBOLS

$\bar{\bullet}$	Accent denoting computational integral quantity
$\bar{\bullet}$	Accent denoting computational variables
$\bullet_*$	Subscript denoting dimensionless quantities
$\bullet_b, \bullet_f, \bullet_s$	Subscript denoting backing, friction, and separator materials
$\bullet_{min}, \bullet_{max}$	Subscript denoting minimum and maximum values of quantities
$\bullet^*$	Superscript denoting dimensionless quantities
$\bullet^{[i]}$	Superscript with argument denoting discrete grid location
$a_{1T}, a_{2T}, a_{3T},$ $a_{4T}, a_{5T}$	Coefficients of discrete energy equation
$a_{1Vz}, a_{2Vz},$ $a_{3Vz}, a_{4Vz},$ $a_{5Vz}, a_{6Vz},$ $a_{7Vz}, a_{8Vz},$ $a_{9Vz}, a_{10Vz}$	Coefficients for differential form of continuity equation
$a_p, b_p, c_p,$ $d_p, e_p$	Coefficients of Poisson pressure equation
$b_1, b_2,$ $b_3, b_4$	Constants for isoviscous axisymmetric solution
$c$	Specific heat of material region of interest $\left[ \frac{J}{kg K} \right]$
$e$	Internal energy per unit mass $\left[ \frac{J}{kg} \right]$
$f_c$	Hypothetical right hand side of continuity equation
$f_p$	Forcing function for Poisson pressure equation

$\mathbf{f}_{Vr}$	Discrete vector form of radial momentum forcing function
$f_{Vr}$	Scalar kernel form of radial momentum forcing function
$f_T$	Forcing function of discrete energy equation
$f_{VD}$	Viscous dissipation term in energy equation
$f_{Vz}$	Forcing function for differential form of continuity
$\mathbf{f}_{V\theta}$	Discrete vector form of angular momentum forcing function
$f_{V\theta}$	Scalar kernel form of angular momentum forcing function
$\mathbf{f}_{V\theta BC}$	Discrete vector form of angular momentum boundary conditions
$h$	Film thickness [m]
$h_g$	Groove depth [m]
$h_o$	Minimum film thickness [m]
$h_\infty$	Convective heat transfer coefficient $\left[\frac{W}{m^2 K}\right]$
$i, j, k$	Indices denoting discrete radial, angular, and axial location
$k$	Thermal conductivity $\left[\frac{W}{m K}\right]$
$\mathbf{l}_1, \mathbf{l}_1$	Vector of length $N_z$ containing elements equal to zero or one
$m$	Viscosity-temperature parameter
$n$	Index representing any integer
$\mathbf{n}$	Unit outward normal
$p$	Pressure $\left[\frac{N}{m^2}\right]$
$p_d$	Pressure difference, $p_i - p_o$ $\left[\frac{N}{m^2}\right]$
$p_i$	Pressure at inner radius $\left[\frac{N}{m^2}\right]$
$p_o$	Pressure at outer radius $\left[\frac{N}{m^2}\right]$
$q_r, q_\theta, q_z$	Cylindrical heat flux vector components $\left[\frac{W}{m^2}\right]$
$r$	Radial coordinate [m]
$s$	Local location along surface roughness trace [m]
$t$	Time [s]

$v_r, v_\theta, v_z$	Cylindrical velocity components $\left[\frac{m}{s}\right]$
$\mathbf{v}_r, \mathbf{v}_\theta$	Discrete vector form of radial and angular velocity
$\mathbf{w}$	Discrete weighted vector for numerical integration
$\mathbf{x}, \mathbf{y}$	General discrete vectors
$z$	Axial coordinate $[m]$
$z'$	Global axial coordinate for multiple disk clutch solutions $[m]$
$A$	Viscosity-temperature parameter $[K^m]$
$\mathbf{A}$	Tridiagonal matrix
$\mathcal{A}$	General block-banded matrix
$B$	Viscosity-temperature parameter $\left[\frac{Ns}{m^2}\right]$
$B_1$	Viscosity-temperature parameter $\left[\frac{m^2}{s}\right]$
$Br$	Brinkman number
EHL	Elastohydrodynamic lubrication
$F_{p,h}$	Tangential force due to pressure $[N]$
$F_z$	Normal load $[N]$
$F_{\theta,0}$	Tangential force due to viscous shearing on separator plate $[N]$
$F_{\theta,h}$	Tangential force due to viscous shearing on friction plate $[N]$
$Gr$	Graetz number
$I_1$	Input side mass moment of inertia $[kg\ m^2]$
$I_2$	Output side mass moment of inertia $[kg\ m^2]$
$I_Q$	Numerical approximation of integral of radial velocity component
$I_R$	Ratio of fluid inertia to clutch inertia
$J$	Jacobian matrix
$K_1, K_2, K_3$	Viscosity-temperature parameters
$L$	Axial length of material regions $[m]$

$\mathcal{L}$	Length of surface roughness measurement [ $m$ ]
$M_1$	Input side moment [ $N\ m$ ]
$M_2$	Output side moment [ $N\ m$ ]
$M_F$	Moment due to clutch friction [ $N\ m$ ]
$N_g$	Total number of periodic domains on clutch friction plate
$N_r, N_\theta, N_z$	Number of radial, angular, and axial grid points
$Pr$	Prandtl number
$Q_r$	Volumetric flow rate in radial direction [ $\frac{m^3}{s}$ ]
$Q_\theta$	Volumetric flow rate per unit depth in azimuthal direction [ $\frac{m^2}{s}$ ]
$R_*$	Ratio of outer to inner clutch radii
$R_i$	Inner clutch radius [ $m$ ]
$R_o$	Outer clutch radius [ $m$ ]
$Re$	Reynolds number
$S$	Sommerfeld number
SAE	Society of Automotive Engineers
SUV	Saybolt universal viscosity
$T$	Temperature [ $K$ ]
$T_{AVG}$	Nodal average temperature [ $K$ ]
$T_\infty$	Ambient temperature [ $K$ ]
$T_o$	Radial inlet temperature [ $K$ ]
$T_{ref}$	Reference temperature [ $K$ ]
$Z$	Local height of surface measured from mean height [ $m$ ]
$\alpha$	Thermal diffusivity of material region of interest [ $\frac{m^2}{s}$ ]
$\beta_n, \gamma_n, \lambda_n$	Coefficients in isoviscous radial grooved solution
$\epsilon$	Ratio of minimum film thickness to inner radius

$\theta$	Angular coordinate [ $rad$ ]
$\theta_o$	Domain angle of periodicity [ $rad$ ]
$\lambda_{\bar{r}}, \lambda_{\bar{\theta}}, \lambda_{\bar{z}}$	Convective partial derivative coefficients in energy equation
$\mu$	Viscosity [ $\frac{N \cdot s}{m^2}$ ]
$\mu_F$	Coefficient of friction
$\mu_o$	Radial inlet viscosity [ $\frac{N \cdot s}{m^2}$ ]
$\mu_{ref}$	Reference viscosity [ $\frac{N \cdot s}{m^2}$ ]
$\nu$	Kinematic viscosity [ $\frac{m^2}{s}$ ]
$\rho$	Density of material region of interest [ $\frac{kg}{m^3}$ ]
$\sigma$	Root mean square surface roughness [ $m$ ]
$\tau_{rr}, \tau_{r\theta}, \tau_{rz},$	Cylindrical stress tensor components [ $\frac{N}{m^2}$ ]
$\tau_{\theta r}, \tau_{\theta\theta}, \tau_{\theta z},$	
$\tau_{zr}, \tau_{z\theta}, \tau_{zz}$	
$\chi_1, \chi_2$	Geometric groove parameters
$\Gamma_n$	Constant in isoviscous radial grooved solution
$\Delta\bar{r}, \Delta\bar{\theta}, \Delta\bar{z}$	Radial, angular, and axial grid spacings
$\Lambda$	Ratio of minimum film thickness to surface roughness
$\Omega_d$	Relative angular velocity of separator plate [ $\frac{rad}{s}$ ]
$\Omega_*$	Ratio of relative angular velocity to input angular velocity
$\Omega_1$	Input side angular velocity [ $\frac{rad}{s}$ ]
$\Omega_2$	Output side angular velocity [ $\frac{rad}{s}$ ]



## ACKNOWLEDGMENTS

I would like to acknowledge my advisors, Dr. Kwang-Tzu Yang and Dr. Joseph M. Powers, for the opportunity they have given me, their interest in this material, and their endless pursuit of excellence. I would also like to acknowledge my committee members, Dr. Steven R. Schmid, Dr. Samuel Paolucci, Dr. Mihir Sen, and Dr. Albin A. Szewczyk, not only for serving on my committee, but for the educational experiences they have given me. Additional professors at the University of Notre Dame who have inspired my academic pursuits by giving me a broader perspective of the physical and philosophical world include Dr. Robert A. Howland, Dr. James J. Mason, and Dr. Michael M. Stanasic.

I would like to acknowledge Clark-Hurth Components for their sponsorship during most of my graduate career. Specifically, Mr. Hormuz Kerendian and Mr. Rick Honeyager were actively involved in this research.

I would like to acknowledge several of the University of Notre Dame's Aerospace and Mechanical Engineering graduate students for their advice, friendship, and overall companionship: Tom Copps, Keith Gonthier, Rich Sellar, George Ross, Elgin Anderson, Matt Grismer, Rob Minitti, Dave Williams, Ken Cheung, Keith Roessig, and Chris Sullivan. I would also like to mention several close friends who have directly, and indirectly, influenced my educational experiences. I have the pleasure of knowing Felix Kpodo, Mike Cambi, Steve Ryan, John Hanzas, Dan Gabriel, Osiris Gabiam, Jerry Bodine, John Boburka, Mike Connel, Jim Primich, Pete Quast, Diana DiBerardino, Paul Perl, Christine Vogt, Paul Vogt, Mark Heilman, and Ann Heilman. In particular, I wish to thank Sarah Dakin, for her love, compassion, and friendship.

Finally, I would like to thank my family for their constant support and love; my parents, Mike and Mary, my brothers, Steve and Tom, my sister and her husband,

Evelyn and Chuck, and my grandparents, James and Myra.

# CHAPTER 1

## INTRODUCTION

This dissertation will apply hydrodynamic lubrication theory to model the behavior of disk clutches. In particular, this research considers a thin film of lubricant oil between a pair of rotating disk clutch plates. This oil is capable of supporting load, transmitting a shear stress, and sustaining large temperature rises induced by viscous dissipation. Using the disciplines of fluid mechanics and heat transfer, the velocity, pressure, and temperature fields are predicted in the lubricant and the surrounding plates. These distributions may be used to predict normal loads, frictional moments, volumetric flow rates, friction coefficients, and heat generated between clutch plates.

### 1.1 Description of Clutch Operation

A clutch is a mechanical device designed for engaging and disengaging two working parts of a shaft or a shaft and a driving mechanism. Figure 1.1 shows a simplified schematic of a clutch. A rotating input shaft with inertia,  $I_1$ , and angular velocity,  $\Omega_1$ , engages a rotating output shaft with inertia,  $I_2$ , and angular velocity,  $\Omega_2$ . In some cases,  $\Omega_2$  will initially be zero. A driving mechanism supplies an input moment,  $M_1$ . In general, the driven side, or output side will have a load moment,  $M_2$ , which will effect the engagement process. Friction is the physical mechanism through which engagement occurs. If a frictional moment,  $M_F$ , acts at the clutch mating surface,

the equations of motion for bodies 1 and 2 are as follows:

$$I_1 \frac{d\Omega_1}{dt} = M_1 - M_F,$$

$$I_2 \frac{d\Omega_2}{dt} = M_F - M_2.$$

A transmission of mechanical energy, from the input to the output side, occurs during engagement.

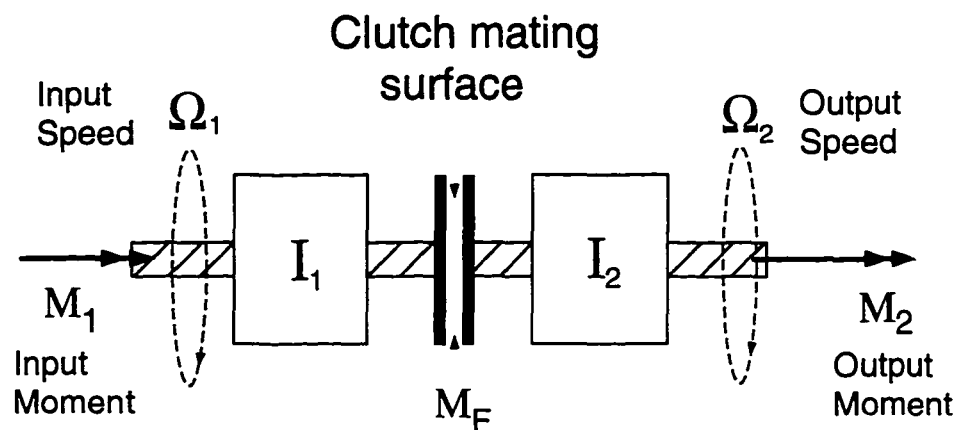


Figure 1.1: Simplified Clutch Schematic

Due to the second law of thermodynamics, not all of the mechanical energy on the input side is transferred to the output side of the clutch. In general, a transient degradation of mechanical to thermal energy occurs. This degradation can lead to high temperatures which may result in several forms of permanent clutch damage. These include warping, melting, seizure, and degradation of friction coefficient.

There is no single design criterion to determine when a clutch should be lubricated to avoid these problems. In dry clutches, typically used in low power applications, one relies on various forms of passive cooling to prevent overheating. Usually, one is concerned with the thermal capacity of the dry clutch's enclosure. However, for

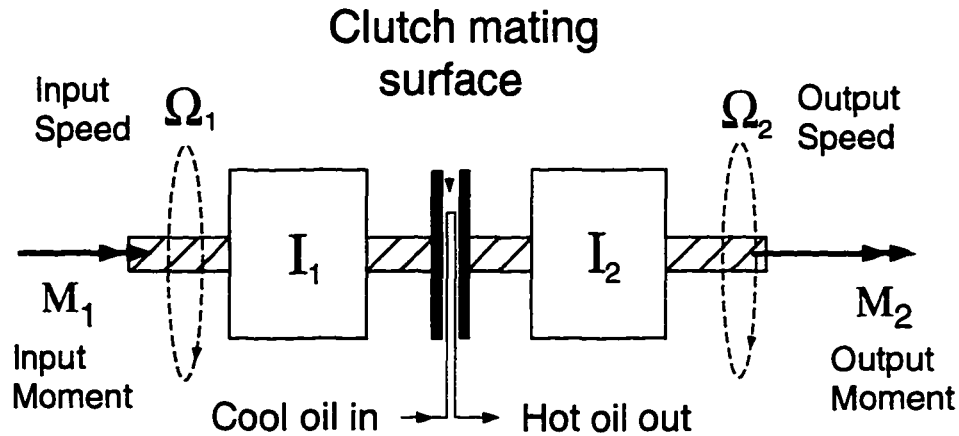


Figure 1.2: Simplified Clutch Schematic with Lubrication

high power applications, a different strategy is to actively cool the mating surfaces as illustrated in Figure 1.2. A lubricant acts as a cooling medium by conveying thermal energy generated between clutch plates. In general, the purpose of lubrication in clutches is to cool frictional surfaces while maintaining desirable friction characteristics. This strategy of active cooling and its effect on the frictional characteristics of disk clutches will be modeled in this research.

## 1.2 Overview of Current Research

In order to investigate the thermal and frictional effects in rotating disk clutches, three models have been developed. They are (1) a thermal model which, considering only the plates, predicts clutch temperature distributions using a presumed friction coefficient, (2) a fluid model which, considering only the lubricant, predicts a friction coefficient using velocity, pressure, and temperature distributions, and (3) a conjugate model which considers the domains encompassing both plates and fluid. The subject of this dissertation is the conjugate model. Each model has benefits and shortcomings.

These will be discussed here.

To adequately discuss the thermal model, some preliminary comments regarding clutch plates are given here. A disk clutch assembly is composed of friction plates and separator plates. Friction plates, which tend to be associated with the input side of a clutch, have three composite material regions as shown in Figure 1.3. The two outer regions, or lining materials are referred to as the friction material. The inner core region of the friction plate is referred to as the backing material. Unlike friction plates, separator plates are made of a single homogeneous region and are usually associated with the output side of a clutch.

The thermal model predicts a detailed temperature distribution in an assembly of clutch plates without consideration of the fluid film. Figure 1.3 illustrates the configuration for the thermal model. Here,  $2L_b$  is the axial thickness of the backing material,  $2L_s$  is the axial thickness of the separator plate, and  $L_f$  is the axial thickness of the friction material lining on each side of the friction plates. The temperature distribution can be obtained by solving the thermal energy equation. At the interfacial boundaries of the clutch plates, continuity of temperature and heat flux is enforced. Heat is generated at these interfaces using specified friction coefficients and pressure distributions. At all other boundaries to the clutch, passive cooling is modeled by specifying the ambient convection coefficients,  $h_\infty$ , and ambient temperatures,  $T_\infty$ , as shown in Figure 1.3. Further, the thermal model accounts for different thermal properties in the three material regions: (1) the friction material, (2) the backing material, and (3) the separator plate.

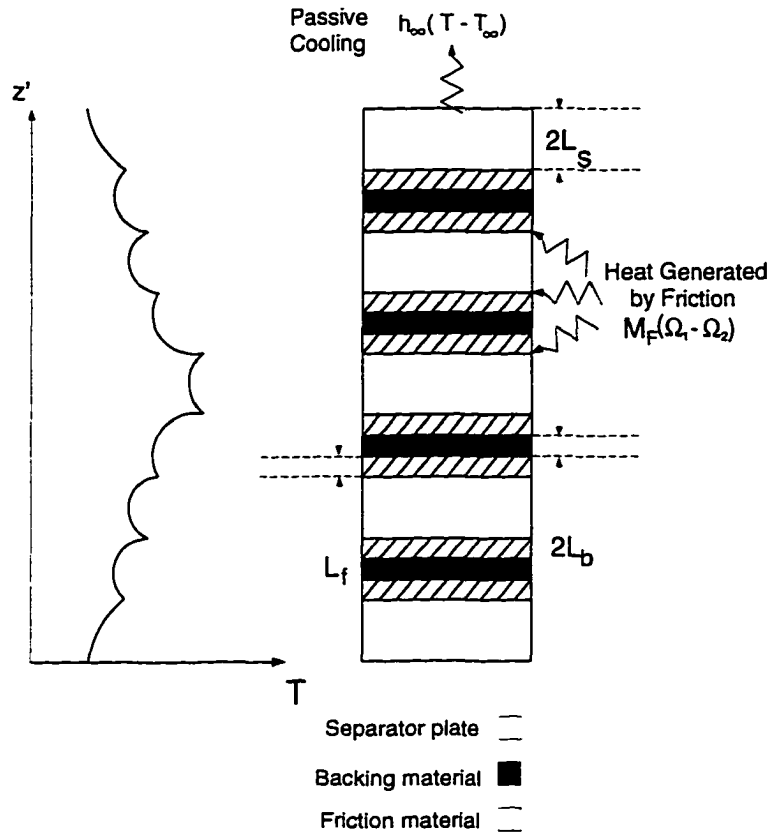


Figure 1.3: Thermal Model Schematic

In addition to predicting the temperature field, the thermal model predicts clutch speed and torque. A shortcoming of this model is that a friction coefficient must be specified *a priori*. This is considered a shortcoming because the coefficient of friction is a contrived quantity which could, in principle, be determined from the physics of clutch engagement. The thermal model is discussed in further detail by Quast and Smith [47] and is not considered in detail in this dissertation.

The fluid model predicts a friction coefficient given the lubricant properties, clutch operating conditions, and geometry. A steady state, incompressible flow field is found in a cylindrical frame,  $(r, \theta, z)$ , between a pair of rotating clutch plates. The cylindrical

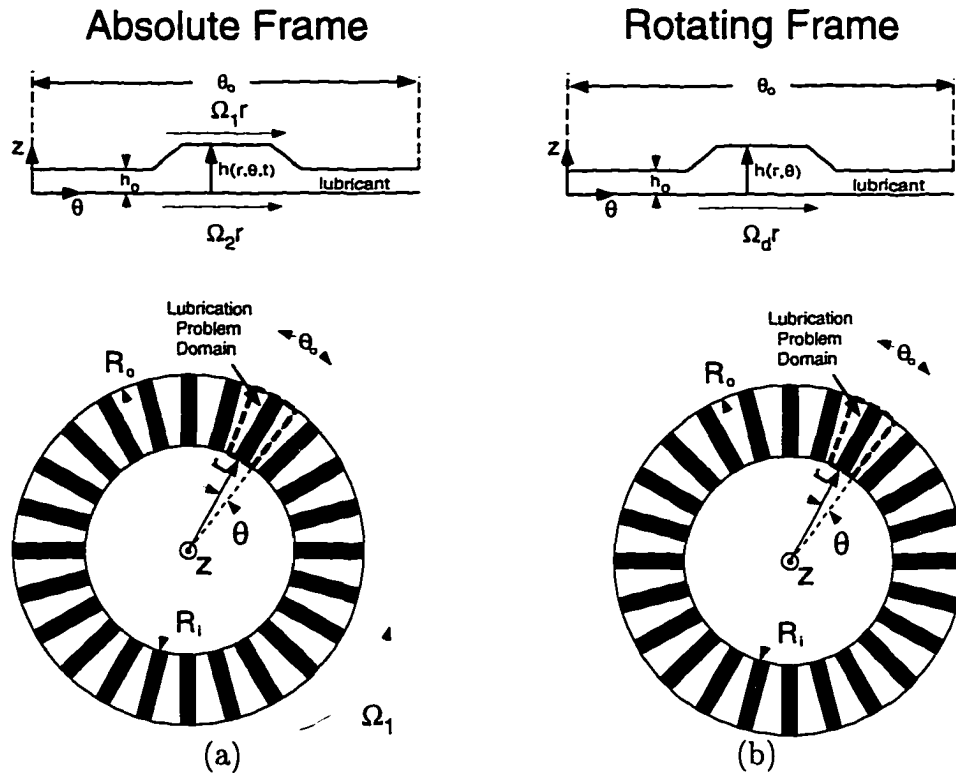


Figure 1.4: Fluid Model Schematic

frame rotates with the clutch friction plates. In other words, velocities are reported with respect to an observer rotating with the friction plates. Figure 1.4 illustrates the fluid model. Here,  $\theta_o$  is the domain angle of periodicity,  $h$  is the local film thickness which is assumed to be a known function of  $r$  and  $\theta$ , and  $h_o$  is the minimum film thickness. In Figure 1.4(a), the absolute frame is shown in which the angular velocity of the friction plate is  $\Omega_1$  and the angular velocity of the separator plate is  $\Omega_2$ . The rotating frame in which we will study the problem moves with the friction plates as shown in Figure 1.4(b). Here,  $\Omega_d = \Omega_2 - \Omega_1$  is the angular velocity of the separator plate as viewed in the rotating frame. In the absolute frame, the film thickness is considered a function of time. However, in the rotating frame the film thickness is



independent of time. In addition, the transformation to the rotating frame gives rise to additional terms, namely centripetal and Coriolis terms, in the governing equations.

In the lubricant, velocity, pressure, and temperature distributions are determined which may be used to predict other clutch performance parameters including frictional moments, normal loads, friction coefficients, and radial volumetric flow rates. However, a coupling between the thermal model and the fluid model is still required because temperature continuity and heat flux continuity is enforced at the solid-fluid interface.

The conjugate model predicts both temperature distributions in the solid clutch plate assembly and velocity, pressure, and temperature distributions in the lubricant. A schematic of the model under consideration is shown in Figure 1.5. A lubrication model is developed between two adjacent, rotating clutch plates. This model is coupled to a model in the adjacent plates by requiring temperature and heat flux continuity across the interfaces. As shown in Figure 1.5, a periodic section of a radially grooved friction pair is considered. While periodic, the theory is developed using an otherwise arbitrarily shaped film. Further, the domain of interest consists of a friction plate and a separator plate separated by a lubricant film.

In the long time limit, a steady state solution is sought for the conjugate heat transfer problem. In such a scenario, towards the middle of an assembly of clutch plates, the temperature gradient is expected to vanish near the center of friction and separator plates resulting in adiabatic conditions at the lubricant/solid interfaces. Several results are given for this *worst case scenario* of clutch plate engagement.

However, some discussion and results are presented for a more general problem which considers the presence of passive cooling at the end of an assembly of clutch plates.

### **1.3 Utility of the Research**

Analyzing clutch behavior often involves a variety of conflicting design criteria. These devices are designed to deliver a certain amount of torque while experiencing limited or no wear. Wear tends to cause friction coefficient degradation resulting in inconsistent clutch performance. Further, at the design stage, one should be wary of large temperature rises which may result during clutch engagement. High temperatures decrease lubricant viscosity leading to a decrease in clutch frictional performance. Moreover, clutches are designed with the intention of meeting a certain engagement schedule. That is, given a torque and a slip speed, a clutch is designed to engage in a certain amount of time, typically under a second.

The reason that meeting these criteria is difficult is that the expectations mentioned are not mutually exclusive. In other words, obtaining a desired torque level within specified design constraints such as low temperature rises, scheduled engagement time, and other operating conditions may be physically impossible.

In order to meet these demanding expectations, a necessary first step to understanding and ultimately optimizing clutch design is to have a valid model. The goals of this dissertation are to (1) construct a model which can be used as a design tool, and (2) to evaluate model results. These goals are discussed here.

Various lubrication theories may be adopted to construct this design tool. Some

background concerning these theories is given here. Hamrock [22] classifies the lubrication regimes as shown in Table 1.1. The thick and thin film regimes are considered hydrodynamic. Here, the ratio of film thickness to surface roughness,  $\Lambda$ , is large enough to neglect asperity contact, and the geometry may be considered smooth. In the hydrodynamic regime, a continuum of lubricant fluid is recognizable. As the film thickness gets smaller, the surface roughness becomes more significant, and asperities begin to support the load. The mixed lubrication regime gets its name from the fact that the load is supported by both asperities and the lubricant. Finally in the boundary lubrication regime, the load is supported by asperities and the lubricant's effects are qualified using chemistry. For example, boundary lubricants form molecular films on the solid surfaces which serve to protect the surfaces from high friction and wear. It is known that the lowering of friction produced by a boundary lubricant is in direct proportion to its molecular weight, and therefore the length of the hydrocarbon chain [30]. Thus, chemistry is employed to qualify the effect of boundary lubrication. Here, the surface geometry and frictional conditions become too complex for a simple continuum model.

Hydrodynamic lubrication theory starts from the perspective that the film size is large enough such that existing continuum theories are valid. Typical mathematical models use the Reynolds equation which may be derived from the more general Navier-Stokes equations in certain distinguished limits. However, assumptions built into the derivation of the Reynolds equation are relaxed in this dissertation. In particular, the assumption of constant viscosity across the film is investigated. In general, it is our

<b>Lubrication Regime</b>	<b>Range of Validity</b>	<b>Load Supported By</b>
Thick Film (hydrodynamic)	$10 < \Lambda < \infty$	Lubricant
Thin Film (hydrodynamic)	$3 < \Lambda < 10$	Lubricant
Mixed	$1 < \Lambda < 3$	Lubricant and Asperities
Boundary	$0 < \Lambda < 1$	Asperities

Table 1.1: LUBRICATION REGIMES ( $\Lambda = \frac{\text{FILM THICKNESS}}{\text{SURFACE ROUGHNESS}}$ )

intention to model this problem from first principles.

The first goal mentioned was to construct a model to be used as a design tool. Properly constructed, such a design tool can be employed to save money, resources, and time. Numerous experiments could be performed in different environments, with different clutch plates, using different lubricants, while running at different operating conditions. On the other hand, significant effort is required to create a complete mathematical model. While a complete mathematical model is beyond the scope of this dissertation, the number of experimental scenarios can be dramatically reduced with simplified mathematical models.

The second goal, evaluating the model results, consists of (1) indicating trends, (2) identifying deficiencies, and (3) proposing needs for future work. Expected or unexpected results obtained from this model are indicated and questioned. Do the parameters used as input predict a logical output? Can the results be used to model

actual clutch engagement? What additional physics should be considered to improve the model? These questions are addressed in the final chapter of this dissertation.

#### 1.4 New Contributions

This dissertation contains many new contributions. Three major contributions are allowing for a variable film shape, allowing for a variable viscosity, and coupling the heat transfer problem to the fluid problem. The first two are discussed here.

Hydrodynamic lubrication theory has never been applied to lubricated disk clutches with an arbitrary film shape. Fluid mechanics problems have been considered in radial grooves [43, 44] and simplified models have been constructed for disk couplings [63]. Further, algebraic mappings which transform a complex domain into a manageable domain are commonly found in computational fluid mechanics studies. Nevertheless, these studies rarely consider arbitrary geometries. In other words, the geometry is typically specified prior to solving the problem of interest. Allowing the film shape to be defined arbitrarily enables virtually any groove pattern to be studied. Furthermore, macroscopic and microscopic deformations could be accommodated using this theory.

Although viscosity variation is claimed in many lubrication studies, the fact is that these models have a viscosity which does not vary in the axial direction. This is not to say that numerical codes which claim to accommodate variable viscosity have not been written.<sup>†</sup> However, classical derivations of the Reynolds equation assume a

---

<sup>†</sup>CFX5, for example, claims to accommodate variable properties. CFX5 is a thermofluids analysis code maintained by AEA Technology located in Pittsburgh, Pennsylvania.

uniform viscosity across the film, and this assumption usually gets carried into the model of interest. It is worth the effort to allow for viscosity variation in clutches because drastic changes in viscosity result from a sensitive temperature relationship. As will be shown, neglecting variable viscosity may result in significant errors in several clutch performance predictions. Furthermore, allowing the viscosity to vary across the film not only has potential in clutch studies, but may be generalized to a larger set of lubrication problems.



## CHAPTER 2

### LITERATURE REVIEW

This review of the relevant literature is divided into four sections: the first gives an overview of clutch studies, the second reviews several devices which are mechanically similar to disk clutches, the third discusses tribological issues pertinent in modeling clutches, and the fourth focuses on several fluid mechanics and heat transfer problems related to clutches. In the first section, the clutch studies overview considers both theoretical and experimental work. The second section discusses studies concerned with rim clutches, disk brakes, and disk couplings. The discussion on tribological issues includes a discussion on lubricant properties and a discussion on surface topography. Finally, the overview of heat transfer and fluid mechanics problems discusses axisymmetric rotating geometries including single and multiple disks in an infinite quiescent fluid, hydrodynamic lidded annulus problems, and differentially heated cavities.

#### 2.1 Clutch Studies

Several topics encountered in studying disk clutch engagement are evident in the literature: comparing lubricant performance, friction coefficient degradation, wear of friction surfaces, microscopic and macroscopic deformation, and the influence of thermal effects including convection, conduction, and thermoelastic deformation. The fact that modeling clutches involves many disciplines has led authors to focus on particular problems. However, several authors have constructed robust models capable



of predicting clutch performance under a variety of conditions. Theoretical models and experimental investigations are discussed here.

### **2.1.1 Theoretical Models**

Payvar [43, 44] has done extensive work in modeling fluid mechanics and heat transfer in the radial grooves of a pair of clutch plates. In his earlier paper, he develops a method to determine heat transfer coefficients in the grooves. In particular, he assumes a Couette flow pattern in the oil film and couples this to a numerical solution in the groove. He treats the film and recirculation zone in the groove as independent thermal resistors which may be added in series to determine the overall heat transfer coefficient. His numerical results compare well with his experimental results. In his later paper, Payvar gives a comparison between experimental techniques and a numerical solution. He considers the steady incompressible Navier-Stokes equations and a diffusing species concentration equation which is analogous to an energy equation. By obtaining measurements for the net sublimated mass of naphthalene before and after a certain time period, comparisons between the average Sherwood number obtained numerically and experimentally were given. All in all, while he considers many terms in the Navier-Stokes equations, he has a limited parameter space. In his models, he neglects viscosity-temperature effects, assumes a flow solution adjacent to the grooves of the friction plates, and insulates the friction plates to expedite a solution. Nevertheless, he predicts convection coefficients based on groove dimensions, Reynolds number, and Nusselt number.

The conditions of clutch operation can have significant consequences on the lubri-

cant. The sensitive viscosity-temperature relation should be considered in hydrodynamic models. Natsumeda and Miyoshi [38] develop a fairly elaborate clutch model which takes viscosity-temperature effects into account. However, as suggested in the previous chapter, this model does not account for viscosity variation across the film. Nevertheless, they allow for clutch plate waviness, elastic deformation due to asperity contact, and surface roughness using Patir and Cheng's model [41]. Their model may be considered a mixed lubrication problem. However, many questionable assumptions are made in the formulation of the model. For example, asperity deformation is assumed elastic which should be confirmed by computing a Greenwood-Williamson plasticity index [30] or by some other rational method. Nevertheless, they make a valuable contribution by computing the load carrying capacity using both asperity contact and hydrodynamic lubricant pressure. Bardzimasvili and Yashvili [3] describe a method which accounts for not only the mixed regime of lubrication, but the hydrodynamic and boundary regimes as well. However, results are not given. Their model predicts multiple disk clutch torque and angular velocity using an interrelated set of ordinary differential equations. They do not account for thermal effects.

Severe wear of clutch lining materials has motivated many studies, including Solt [59] who attempts to optimize the load distributions using finite element methods. He explains that non-uniform loadings, which induce deformation, lead to wear near the location of maximum pressure. For known clutch plate dimensions, his results suggest that there is an optimum location for the actuating force. Zagrodzki [69] develops a similar model which is generalized to account for thermoelastic effects. His

two-dimensional, time-dependent heat conduction model accounts for heat generation and elastic deformation due to dry contact. Yevtushenko and Ivanyk [68] estimate the surface temperatures and normal temperature displacements due to thermoelastic effects using a straightforward analytic model. They show that the change in magnitude of contact area due to thermal distortion may be neglected.

### 2.1.2 Experimental Investigations

The choice of lubricant has significant effects on the performance of disk clutches. Ito, Fujimoto, Eguchi, and Yamamoto [32] experimentally determine clutch friction coefficients under various conditions. In addition to varying the lubricant, their studies include variable speed, loading, and friction plate porosity. Results indicate marked difference in clutch performance. In particular, two oils were used: Dextron 2 automatic transmission fluid (ATF) and a paraffinic mineral oil which was equivalent to the base oil of the ATF. For a range of sliding velocity varying from 0.01 to 1.0  $\frac{m}{s}$ , the ATF's friction coefficient remained fairly constant at 0.15 while the paraffinic oil's friction coefficient approximately changed from 0.2 to 0.1. This is significant because the ATF will provide a nearly constant torque level over this speed range and the paraffinic oil's torque level could reduce by one half. Ichihashi [31] discusses the increasing trend of equipping automobiles with ATF's as well as developing improvements in ATF additives for improved clutch performance. Scott and Suntiawattana [56] examine wear rates, lubricant temperature, and clutch torque by varying the relative quantities of five different additives to the same base oil. Scott and Suntiawattana report marginal differences in clutch friction coefficient and lock-up

time with different additive concentration.

Viscosity-temperature effects are one of many effects which can be used to explain degradation of clutch friction coefficients. Another effect is the presence of additives. Inorganic additives added to the base oil chemically attack asperities yielding different friction properties of the mating surfaces. Still another effect is direct wear of friction materials. Osani, Ikeda, and Kato [39] show that there is a distinct degree of carbonization of paper-based facings beyond which the friction coefficient drops off rapidly. Schulz [55] agrees that this gaseous form of wear plays a major role in determining friction characteristics in a disk clutch.

## **2.2 Related Mechanical Devices**

Takemuro and Niikuro [63] analyze viscous disk couplings which may be used in limited slip differentials. Disk clutches and disk couplings have very similar geometries. Each may contain multiple disks which rotate for the purpose of transmitting torque. However, disk couplings have separator rings which ensure a finite clearance between adjacent plates. Takemuro and Niikuro develop a straightforward method to determine torque, temperature rise, and dynamic response in the couplings. Viscosity-temperature effects and non-Newtonian effects are taken into account to model the working fluid, silicone oil. However, an energy equation was not stated explicitly for the lubricant. Rather, a numerical method which employed a lumped analysis was used to obtain the temperature at disk interfacial locations. In other words, spatial temperature gradients in the fluid were ignored.

Whittle, Atkin, and Bullough [64] examine a rim clutch filled with an electrorheological fluid. As in other clutch lubrication problems, the equations of motion are analyzed under the assumption of small clearance. Unlike a disk clutch, the small clearance in a rim clutch is the difference in radii.

Stebar, Davison, and Linden [60] examine the effects that various automatic transmission fluids have on the torque versus time curve for band clutch engagement. Their experimental results indicated that the choice of lubricant can have dramatic effects on shift smoothness, clutch capacity, energy absorption, lock-up torque, and engagement time.

### **2.3 Tribological Issues**

Tribology is the science of the mechanisms of friction, lubrication, and wear of interacting surfaces that are in relative motion. Here, two pertinent aspects of tribology are discussed: (1) rheology of mineral oils, and (2) surface topography.

#### **2.3.1 Mineral Oil Rheology**

This discussion of mineral oils is divided into four sections. First, a discussion of mineral oils' chemistry is given. Second, the constitutive equation relating the stress and strain rate tensors is discussed. Third, comments regarding property variations are given. Fourth, a specific discussion of the viscosity-temperature relation is given.

#### **Chemistry of a Mineral Oil**

Hamrock [22] and Robertson [48, 49] give synopses of the chemistry of mineral oils and why their chemistry is important from an engineering perspective. Mineral

oils are composed of paraffinic chains and naphthenic rings of hydrocarbons. Paraffins tend to weigh less, have less severe viscosity-temperature relations, and have higher flash and fire points than naphthenes. Naphthenes have lower pour points and produce less carbonaceous residue at extreme temperatures. These flash, fire, and pour points, indicative of a mineral oil's temperature related classification, will be discussed shortly. In lubrication applications, additives are used to improve the friction properties of the base oil. Singh [58] discusses viscosity index improvers such as oil soluble polymers which tend to decrease the viscosity's dependence on temperature depending on the base oil character, type of finishing procedure, and additive concentration.

### **Stress-Strain Rate Relation**

Mineral oils exhibit Newtonian behavior over a wide range of operating conditions. Non-Newtonian effects come into play with very large strain rates and are usually considered in the presence of additives such as oil soluble polymers. Roelands [50] states that significant changes in the oil's viscosity occur at strain rates exceeding  $10^7 s^{-1}$ . One should be concerned about the non-Newtonian character of the fluid when the relative velocity is large and the film is thin. For the problem discussed in this dissertation, typical strain rates are approximately  $10^5 s^{-1}$  which are significantly below the point at which non-Newtonian effects occur.

An extensive review of experimental and theoretical non-Newtonian fluid mechanics is given by Wilkinson [65]. A more restricted study is given by Johnson and Tevaarwerk [34] in which they analyze non-Newtonian effects in oil films using

experimental methods.

### **Property Variations**

Pressure dependent viscosities are considered in non-conformal contact problems such as modeling gears, cams, or bearings [23, 28]. A nonconformal contact occurs when the bodies in question mate at a point under no load. For example, the contact between two spheres is considered a nonconformal contact. Under such conditions, the pressures become extremely high and viscosity variations become important. Specifically, Roelands [50] states that when the average pressure over the contact area exceeds several thousand pounds per square inch, piezoviscous effects become important. On the macroscopic scale, a wet disk clutch has the geometry associated with a nominally conformal contact problem, and pressure dependent viscosities may be neglected. Typical clutch lubrication and actuation pressures rarely exceed two or three hundred pounds per square inch.

For mineral oils, the specific heat and conductivity are relatively constant for large changes in temperature [22, 50]. Compared to the changes associated with the viscosity-temperature relation, these variations are extremely small.

For the range of pressures and temperatures considered in this lubrication problem, mineral oils have a fairly constant density compared to the variation of viscosity with temperature. Roelands [50] notes that the kinematic viscosity may be taken as a good measure of the viscosity for mineral oils and other synthetic oils with nearly equal densities. For a typical mineral oil, the variation in density with pressure becomes significant (greater than one percent) at pressures exceeding 0.02 MPa. However, the

variation of density with temperature is more sensitive. Density changes of nearly ten percent occur from  $0^{\circ}\text{C}$  to  $160^{\circ}\text{C}$ . Nevertheless, while it is unclear how seriously density variations will effect clutch performance, these variations are small compared to the relative change in viscosity for the same conditions and are consequently ignored.

Nevertheless, there is concern regarding incompressibility, at *low* pressures. If the lubricant's pressure falls below the vapor pressure, cavitation will occur. Batchelor [4] notes the fundamental difference between a real liquid and an ideal incompressible fluid: negative pressures can be predicted in an ideal fluid, and a liquid cannot support a large tension. Rather, Batchelor states that small pockets of gas appear in the liquid which are responsible for cavity formation and supporting tension. Hamrock [22] notes that mineral oils contain nearly ten percent entrained gases which form cavities when the pressure falls below the saturation pressure. Further, he summarizes the traditional boundary conditions used in modeling converging/diverging domains. Birkhoff and Hays [7] cite specific theorems regarding geometry and operating conditions which necessarily lead to cavitation. Further, they developed a general improvement over the Swift-Steiber boundary conditions [22] commonly employed today. Coyne and Elrod [11] develop a rational method to apply boundary boundary conditions when cavitation is expected to occur in converging-diverging domains. Surface tension effects are included in their analysis. Most importantly, they state that the load carrying capacity does not vary appreciably no matter which boundary conditions are used. In more general fluid mechanics problems, bubble formation is treated using the full Navier-Stokes equations. Ryskin and Leal [51, 52, 53] develop



a numerical procedure for two-dimensional mapping of a liquid-solid interface with unknown orientation.

### Viscosity-Temperature Relation

For a wet disk clutch, the most quantitatively significant dependence of any physical property is that of the viscosity with temperature. Mineral oils are classified according to their viscosity-temperature performance. For example, the familiar SAE 10-W30 designation is a Society of Automotive Engineers' approved classification of a mineral oil.<sup>†</sup> The first number, 10, denotes the Saybolt Universal Viscosity<sup>†</sup> (SUV) restrictions at 130°F and at 210°F. The alpha-numeric code, W30, denotes the SUV restrictions at 0°F.

Further temperature related classifications and restrictions on the viscosity of a mineral oil exist. Several examples are mentioned here. The *viscosity index* (VI) is a classification which measures the rate which a given mineral oil's viscosity changes with an increase in temperature. A high viscosity index, indicative of small viscosity variation with temperature, is considered desirable so that the lubricant film maintains stable frictional characteristics at high temperatures. The *Flash Point* is the lowest temperature at which oil vapors appear. The *Fire Point* is the lowest temperature at which a continuous combustion of oil occurs. In order to maintain the film, the operating lubricant temperature should be safely below the Flash Point. The *Pour Point* is the lowest temperature at which the oil will remain fluid enough to

---

<sup>†</sup>Since 1978, this method of classification has been accepted by the American Petroleum Institute (API) and the American Society for Testing and Materials (ASTM) [13].

<sup>†</sup>See Hamrock [22] and/or Robertson [48, 49] for good discussions of the Saybolt Universal Viscosity.

perform a required task. For example, an automotive application of the Pour Point may be the lowest temperature at which oil will flow into the pump inlet of a crank case. This is important in cold weather environments.

The fact that these loosely defined terms have become commonplace in practical engineering applications has not helped to quantify a viscosity-temperature relation. Exact numbers simply do not exist for every mineral oil. Rather, as mentioned above, the viscosity of a mineral oil falls in a range given by the SUV restrictions.

Still, several attempts have been made to quantify the viscosity-temperature relation for mineral oils. Hersey [24] cites nearly ten viscosity-temperature relationships. Hamrock [22] cites three such relations. More recent authors, including Hussain [29] have made attempts at modeling the viscosity-temperature relation. The viscosity-temperature relation used in this dissertation will be that of Walthers [18].

### **2.3.2 Surface Topography**

Surface topography is a geometrical description of the surface of interest. In modeling clutch plate engagement, both macroscopic and microscopic descriptions are relevant. The macroscopic description refers to gross deformations or outstanding geometric patterns while the microscopic description refers to the surface roughness which is describable in a statistical sense.

In all previously mentioned deformation related studies, clutch plate deformation occurs as a result of direct contact. Specifically, two mechanisms are responsible for macroscopic clutch plate deformation: elastic and thermoelastic effects. Elastohydrodynamic lubrication (EHL) would likely not occur on the macroscopic scale

because, as mentioned previously, the engagement of clutch plates is a nominally conformal contact problem. Again, in a conformal contact problem, the lubricant pressure will act over a greater area and not cause any significant deformation. In fact, Hoglund and Jacobson [26] state that in an EHL contact the pressures are very high (1 – 3 *GPa*). This is three orders of magnitude higher than typical clutch actuation pressures, 2 *MPa*.

EHL may be relevant on a microscopic scale. Certainly significant asperity deformation occurs as a result of direct contact between engaging clutch plates. This has been modeled in several of the mentioned clutch studies. On a microscopic scale, statistical descriptions seem to be the only rational method to incorporate surface roughness in the models.

Hamrock [22] and Hutchings [30] give discussions on how to quantify surface roughness. The most popular measure of surface roughness,  $\sigma$ , is the root mean square (rms) of the height measured from the mean surface height:

$$\sigma = \sqrt{\frac{1}{\mathcal{L}} \int_0^{\mathcal{L}} \mathcal{Z}(s)^2 ds}.$$

Here,  $\mathcal{L}$  is the measured length of a simple trace and  $\mathcal{Z}(s)$  is the local height computed above and below the mean value at the  $s$ -location along the trace. The trace is usually taken with a device known as a stylus profilometer [30].

One of the difficulties with using the above description of surface roughness is that it only gives a two-dimensional sample of the entire three dimensional surface. Sullivan, Poroshin, and Hooke [62] discuss the necessity of incorporating a three-dimensional description of the surface roughness. Further, they discuss problems

encountered in differentiating between elastic and plastic deformation of asperities. Three-dimensional surface roughness effects have been included in several lubrication studies [66, 70]. In these studies, Patir and Cheng's [41, 42] work on developing an average Reynolds equation to obtain the pressure was used. In particular, Patir and Cheng use an equation which takes surface roughness and non-isotropic asperity effects into account. Specifically, given the gross film thickness and limited information about the microscopic description of the surface, they introduce what they label flow rate factors to predict the lubricant pressure in separate lubrication studies.

#### **2.4 Related Fluid Mechanics and Heat Transfer Problems**

The fluid mechanics and heat transfer problems discussed in this section are examples of axisymmetric flow adjacent to solid rotating disks. There is a wealth of basic studies of such flows, a few of which are mentioned here.

Batchelor [5] has considered the steady axisymmetric flow between two infinite rotating disks. He reduced the governing equations using an assumed similarity solution. His results may be used to obtain information locally to a set of finite disks. Millsaps and Pohlhausen [36] generalized Batchelor's similarity solution to include heat transfer. Stewartson [61] provided experimental evidence supporting Batchelor's predicted streamlines when the disks rotate in the same direction. Lance and Rogers [35] solved the hydrodynamic problem numerically. They present results for the two dimensionless parameters: the ratio of the angular velocities of the disks and the Reynolds number. Boundary layers in single disk solutions using the similarity

solution are discussed extensively by Schlichting [54]. Pearson [45] generalized the previous hydrodynamic theory to include time-dependent terms in the Navier-Stokes equations. In particular, he obtained numerical results using a generalized similarity transformation with either one or two impulsively started infinite disks. Unlike previously mentioned authors, Pearson's problem involves partial differential equations with time and axial position as independent variables.

Recent improvement in computer hardware and numerical methods has enabled the systematic computation of solutions to larger sets of partial differential equations. Evans and Grief [15] consider flow and heat transfer around a rotating disk chemical vapor deposition reactor. Compressibility and buoyancy are taken into account. Here, a single disk is centered in a cylindrical tube. The spin axis of the cylinder and the gravity vector are coaxial. Buoyancy effects in differentially heated rotating vertical cavities are discussed by Barcilon and Pedlosky [1, 2] and Homsy and Hudson [27]. Their work included obtaining physical solutions by formally linearizing the equations of motion in the limits of small and large Eckman number. Chew [9] and Guo and Zhang [20] present numerical results for these rotating lidded cylinders.

Lidded annulus problems are reviewed extensively by Di Prima and Swinney [12] within the context of studying instabilities in Taylor flow. Experimental results showing Taylor vortices in lidded cylinders are given by Cole [10]. Numerical results for chaotic flow in a lidded annulus are presented by Hadid [21].

## CHAPTER 3

### MATHEMATICAL MODEL

This chapter gives the mathematical statement of the problem investigated in this research. In the first section, the domain and physical variables are defined. In the second section, the mass, momentum, and energy equations are listed, and underlying assumptions pertinent to disk clutch lubrication are discussed. In the third section, constitutive equations are stated. In the fourth section, boundary conditions are stated. In the fifth section, the equations are non-dimensionalized and written in terms of  $O(1)$  dimensionless variables and appropriate dimensionless quantities. Further, the equations are simplified by examining the order of magnitude of the dimensionless parameters. In the sixth section, the complete statement of the problem is given. The seventh section introduces the algebraic coordinate transformation used to solve the governing equations in a computational domain. In the eighth section, pertinent clutch performance parameters are defined in terms of the dependent variables.

#### 3.1 Domain and Variable Definitions

The lubrication problem is illustrated in Figure 3.1. Let  $r$ ,  $\theta$ , and  $z$  denote the radial, angular, and axial Eulerian cylindrical coordinates which rotate with angular velocity  $\Omega_1$ , coincident with the clutch friction plates. The separator plate angular velocity, as viewed in the rotating frame, is  $\Omega_d$ . The physical domain for the lubrica-

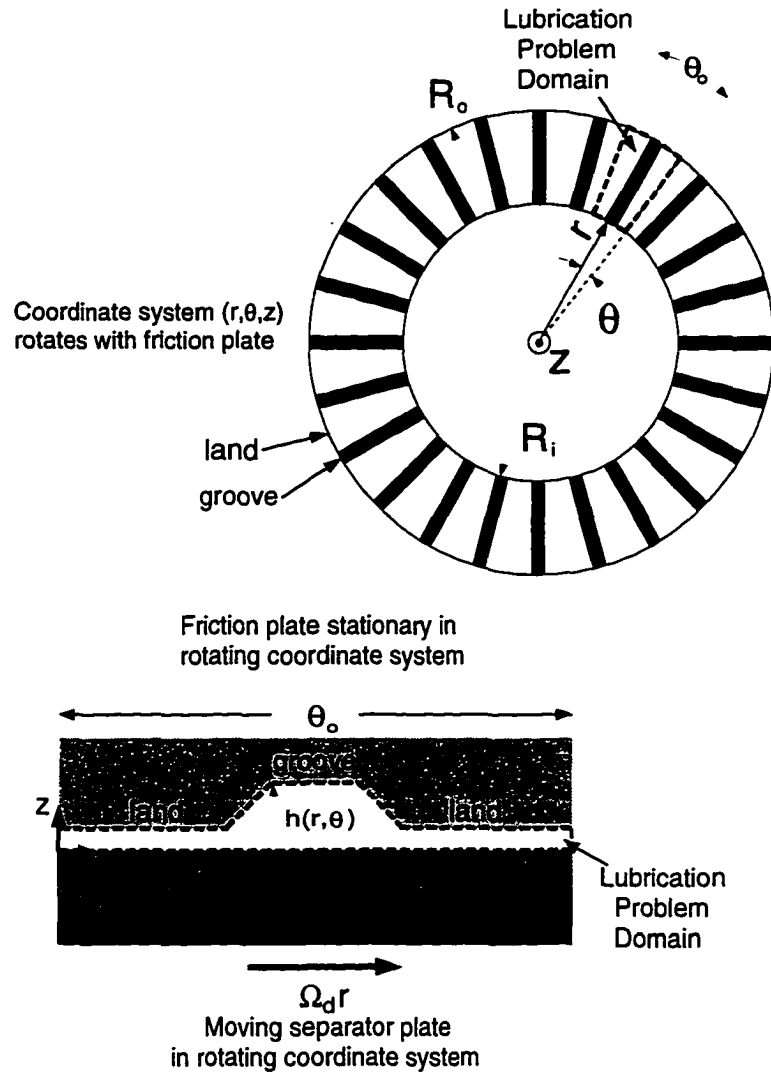


Figure 3.1: Lubrication Problem Domain

tion problem as indicated in Figure 3.1 is defined by  $R_i \leq r \leq R_o$ ,  $0 \leq \theta \leq \theta_o$ , and  $0 \leq z \leq h(r, \theta)$ . Here,  $R_i$  and  $R_o$  are inner and outer clutch radii,  $\theta_o$  is the domain angle of periodicity, and  $h$  is the local film thickness. The domain angle of periodicity is the minimum angle required to replicate the entire film thickness. It is always an integral fraction of  $2\pi$ . The film thickness,  $h$ , is a known periodic but otherwise arbitrary function of  $r$  and  $\theta$ . That is,  $h(r, 0) = h(r, \theta_o) = h(r, n\theta_o)$ , where  $n$  is any integer. The radial channels shown in Figure 3.1 are referred to as *grooves*. The

adjacent portions to the grooves are referred to as *lands*. Thus, the domain shown in Figure 3.1 contains a groove and two half lands.

The general lubrication problem is then to determine the radial velocity,  $v_r$ , the angular velocity,  $v_\theta$ , the axial velocity,  $v_z$ , the pressure,  $p$ , and temperature,  $T$ , of the fluid as functions of position and time. These quantities, with the exception of  $v_\theta$ , are invariant when referred to an absolute frame. The absolute angular velocity is  $v_\theta + \Omega_1 r$ . The radial flow of lubricant into the domain is affected by a specified pressure difference. The radial inlet temperature of the lubricant is controlled with an external cooling system.

The thermal problem is to obtain the temperature distribution in the solid clutch plates by determining the distributions in each material region. The separator plate is composed of one solid homogeneous region, while a friction plate is composed of three composite homogeneous regions. Referring to Figure 1.3, assuming the modeled lubricant is near the center of a large number of plates, a worst case scenario, illustrated in Figure 3.2, would employ adiabatic conditions at the central axial planes of the friction and separator plates. The thermal problem is then subdivided into three complementary domains: (1) the backing material, (2) the friction material, and (3) the separator plate. For each region, the radial and angular coordinates coincide with the lubrication problem. However, as shown in Figure 3.2, the axial coordinate depends on the material region of interest. The backing material with axial length  $L_b$  uses the axial coordinate  $z_b$  as shown in Figure 3.2. Similarly, the friction and separator materials with axial lengths  $L_f + h_o - h$  and  $L_s$  use the axial coordinates



$z_f$  and  $z_s$ , respectively.

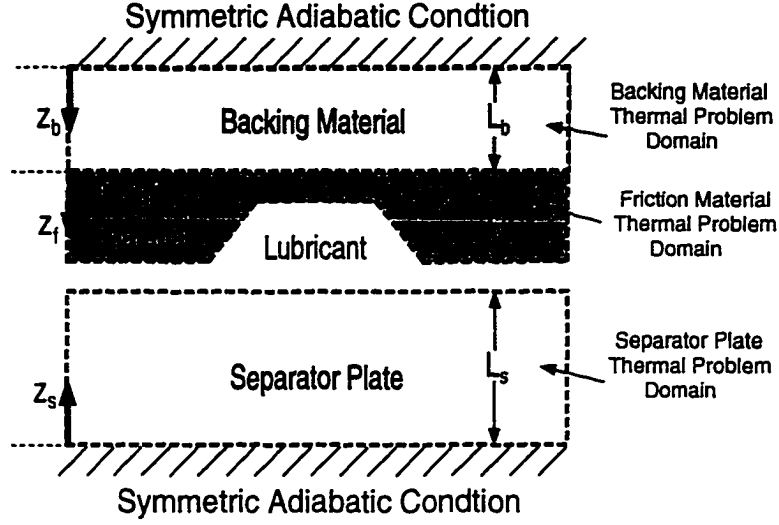


Figure 3.2: Thermal Problem Domain

### 3.2 Conservation Principles

To start, we adopt the incompressible Navier-Stokes equations to model the lubricant behavior. We assume the fluid is continuous and sufficiently thick to neglect surface roughness effects. Body forces are neglected.

The condition of incompressibility requires the continuity equation to be of the following form:

$$\frac{1}{r} \frac{\partial}{\partial r} (rv_r) + \frac{1}{r} \frac{\partial v_\theta}{\partial \theta} + \frac{\partial v_z}{\partial z} = 0. \quad (3.1)$$

The momenta equations are written in a frame moving with the constant friction plate angular velocity,  $\Omega_1$ :

$$\begin{aligned} \rho \left[ \frac{\partial v_r}{\partial t} + v_r \frac{\partial v_r}{\partial r} + \frac{v_\theta}{r} \frac{\partial v_r}{\partial \theta} + v_z \frac{\partial v_r}{\partial z} - \frac{1}{r} (v_\theta + \Omega_1 r)^2 \right] \\ = -\frac{\partial p}{\partial r} + \frac{1}{r} \frac{\partial}{\partial r} (r\tau_{rr}) + \frac{1}{r} \frac{\partial \tau_{\theta r}}{\partial \theta} + \frac{\partial \tau_{zr}}{\partial z} - \frac{\tau_{\theta\theta}}{r}, \end{aligned} \quad (3.2)$$

$$\begin{aligned} \rho \left[ \frac{\partial v_\theta}{\partial t} + v_r \frac{\partial v_\theta}{\partial r} + \frac{v_\theta}{r} \frac{\partial v_\theta}{\partial \theta} + v_z \frac{\partial v_\theta}{\partial z} + \frac{v_r v_\theta}{r} + 2\Omega_1 v_r \right] \\ = -\frac{1}{r} \frac{\partial p}{\partial \theta} + \frac{1}{r} \frac{\partial}{\partial r} (r\tau_{r\theta}) + \frac{1}{r} \frac{\partial \tau_{\theta\theta}}{\partial \theta} + \frac{\partial \tau_{z\theta}}{\partial z} + \frac{\tau_{r\theta}}{r}, \end{aligned} \quad (3.3)$$

$$\rho \left[ \frac{\partial v_z}{\partial t} + v_r \frac{\partial v_z}{\partial r} + \frac{v_\theta}{r} \frac{\partial v_z}{\partial \theta} + v_z \frac{\partial v_z}{\partial z} \right] = -\frac{\partial p}{\partial z} + \frac{1}{r} \frac{\partial}{\partial r} (r\tau_{rz}) + \frac{1}{r} \frac{\partial \tau_{\theta z}}{\partial \theta} + \frac{\partial \tau_{zz}}{\partial z}. \quad (3.4)$$

The lubricant energy equation, written to account for incompressibility, is as follows:

$$\begin{aligned} \rho \left[ \frac{\partial e}{\partial t} + v_r \frac{\partial e}{\partial r} + \frac{v_\theta}{r} \frac{\partial e}{\partial \theta} + v_z \frac{\partial e}{\partial z} \right] = - \left[ \frac{1}{r} \frac{\partial}{\partial r} (rq_r) + \frac{1}{r} \frac{\partial q_\theta}{\partial \theta} + \frac{\partial q_z}{\partial z} \right] \\ + \tau_{rr} \frac{\partial v_r}{\partial r} + \tau_{r\theta} \left( \frac{1}{r} \frac{\partial v_r}{\partial \theta} - \frac{v_\theta}{r} + \frac{\partial v_\theta}{\partial r} \right) + \tau_{rz} \left( \frac{\partial v_r}{\partial z} + \frac{\partial v_z}{\partial r} \right) \\ + \tau_{\theta\theta} \left( \frac{1}{r} \frac{\partial v_\theta}{\partial \theta} + \frac{v_r}{r} \right) + \tau_{\theta z} \left( \frac{\partial v_\theta}{\partial z} + \frac{1}{r} \frac{\partial v_z}{\partial \theta} \right) + \tau_{zz} \frac{\partial v_z}{\partial z}, \end{aligned} \quad (3.5)$$

In Equations (3.2) through (3.5),  $\tau_{rr}$ ,  $\tau_{\theta\theta}$ ,  $\tau_{zz}$ ,  $\tau_{r\theta} = \tau_{\theta r}$ ,  $\tau_{rz} = \tau_{zr}$ , and  $\tau_{\theta z} = \tau_{z\theta}$  are the components of the symmetric stress tensor,  $q_r$ ,  $q_\theta$ , and  $q_z$  are the components of the heat flux vector,  $e$  is the internal energy per unit mass, and  $\rho$  is the density.

The governing equation used to predict the temperature distribution in each material region of the solid clutch plates is the thermal energy equation. In the rotating frame, the thermal energy equations for the material regions in the friction plates is as follows:

$$\rho_f \frac{\partial e_f}{\partial t} + \left[ \frac{1}{r} \frac{\partial}{\partial r} (rq_{rf}) + \frac{1}{r} \frac{\partial q_{\theta f}}{\partial \theta} + \frac{\partial q_{zf}}{\partial z} \right] = 0, \quad (3.6)$$

$$\rho_b \frac{\partial e_b}{\partial t} + \left[ \frac{1}{r} \frac{\partial}{\partial r} (rq_{rb}) + \frac{1}{r} \frac{\partial q_{\theta b}}{\partial \theta} + \frac{\partial q_{zb}}{\partial z} \right] = 0. \quad (3.7)$$

Also in this frame, the thermal energy equation for the separator plates is as follows:

$$\rho_s \left[ \frac{\partial e_s}{\partial t} + \Omega_d \frac{\partial e}{\partial \theta} \right] + \left[ \frac{1}{r} \frac{\partial}{\partial r} (rq_{rs}) + \frac{1}{r} \frac{\partial q_{\theta s}}{\partial \theta} + \frac{\partial q_{zs}}{\partial z} \right] = 0. \quad (3.8)$$

In Equations (3.6-3.8), the subscripts  $f$ ,  $b$ , and  $s$  denote friction, backing, and separator material regions.

### 3.3 Constitutive Equations

The modeled lubricant is considered to be a Newtonian thermoviscous Stokesian fluid [14]. The components of the stress tensor in cylindrical coordinates are defined as follows:

$$\begin{aligned} \tau_{rr} &= 2\mu \frac{\partial v_r}{\partial r}, & \tau_{r\theta} &= \mu \left[ r \frac{\partial}{\partial r} \left( \frac{v_\theta}{r} \right) + \frac{1}{r} \frac{\partial v_r}{\partial \theta} \right], & \tau_{rz} &= \mu \left[ \frac{\partial v_z}{\partial r} + \frac{\partial v_r}{\partial z} \right], \\ \tau_{\theta\theta} &= \frac{2\mu}{r} \left[ \frac{\partial v_\theta}{\partial \theta} + v_r \right], & \tau_{\theta z} &= \mu \left[ \frac{\partial v_\theta}{\partial z} + \frac{1}{r} \frac{\partial v_z}{\partial \theta} \right], & \tau_{zz} &= 2\mu \frac{\partial v_z}{\partial z}. \end{aligned} \quad (3.9)$$

In Equation (3.9),  $\mu$  is the viscosity. The components of the heat flux vector in the fluid are defined as follows:

$$q_r = -k \frac{\partial T}{\partial r}, \quad q_\theta = -\frac{k}{r} \frac{\partial T}{\partial \theta}, \quad q_z = -k \frac{\partial T}{\partial z}. \quad (3.10)$$

Similarly, using Fourier's law in the material regions of the clutch plates, the components of the heat flux vectors are defined as follows:

$$\begin{aligned} q_{rf} &= -k_f \frac{\partial T}{\partial r}, & q_{\theta f} &= -\frac{k_f}{r} \frac{\partial T}{\partial \theta}, & q_{zf} &= -k_f \frac{\partial T}{\partial z_f}, \\ q_{rb} &= -k_b \frac{\partial T}{\partial r}, & q_{\theta b} &= -\frac{k_b}{r} \frac{\partial T}{\partial \theta}, & q_{zb} &= -k_b \frac{\partial T}{\partial z_b}, \\ q_{rs} &= -k_s \frac{\partial T}{\partial r}, & q_{\theta s} &= -\frac{k_s}{r} \frac{\partial T}{\partial \theta}, & q_{zs} &= -k_s \frac{\partial T}{\partial z_s}. \end{aligned} \quad (3.11)$$

In Equations (3.10) and (3.11),  $k$ ,  $k_f$ ,  $k_b$ , and  $k_s$  are the thermal conductivities for the lubricant, friction material, backing material, and separator material respectively.

For the lubricant, the internal energy per unit mass is related to the temperature by the following caloric equation of state:

$$e = cT. \quad (3.12)$$

Likewise, the internal energy per unit mass in the clutch plates is defined as

$$e_f = c_f T, \quad e_b = c_b T, \quad e_s = c_s T, \quad (3.13)$$

for the friction, backing, and separator materials respectively. In Equations (3.12) and (3.13),  $c$ ,  $c_f$ ,  $c_b$ , and  $c_s$  are the specific heats for the lubricant, friction material, backing material, and separator material respectively.

SAE number	$m$	$A$ $\times 10^{-11}$ $(K^m)$	$B$ $\times 10^7$ $(\frac{Ns}{m^2})$	$T_{ref}$ $(K)$	$\mu_{ref}$ $\times 10^4$ $(\frac{Ns}{m^2})$
SAE 10	4.6384	5.8352	4294.1	300	712.1
SAE 20	4.5268	3.4057	2596.4	300	1113.2
SAE 30	4.3354	1.2779	5138.3	300	1968.8
SAE 40	4.4733	3.0758	-2209.4	300	3367.2
SAE 50	4.0416	.28723	1497.9	300	5805.2
SAE 60	3.9152	.14758	-3837.2	300	8390.4
SAE 70	3.8165	.08901	455.9	300	12420.0

Table 3.1: RESULTS FROM FITTING SHIGLEY'S DATA INTO WALTHERS'S EQUATION

The viscosity-temperature relation used in this dissertation is based on Walther's equation [18]:

$$\log_{10} (\nu + B_1) = \frac{A}{T^m}$$

This correlation has two noteworthy shortcomings. First, the kinematic viscosity can not be measured experimentally. Therefore, there is an implicit assumption in this equation that the viscosity depends on the density,  $\nu = \frac{\mu}{\rho}$ . However, the density is a

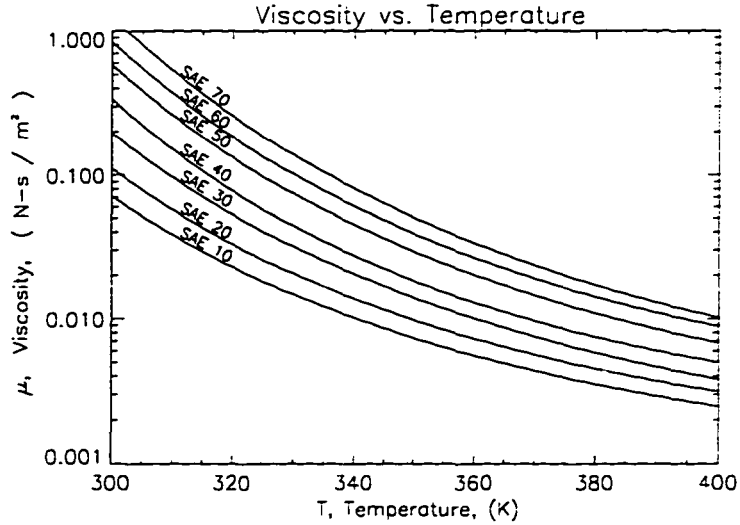


Figure 3.3: Viscosity-Temperature Relation for Seven SAE Oils

thermodynamic property, the viscosity is a transport property, and there is generally no correlation between them. Second, the dimensions on this equation are ambiguous. It is assumed that the parameters  $A$  and  $B_1$  have units of  $K^m$  and  $\frac{m^2}{s}$  respectively.

To avoid these problems, we adopt a hybrid of Walther's viscosity-temperature relation,

$$\log_{10} \left( \frac{\mu + B}{\mu_{ref} + B} \right) = A \left( \frac{1}{T^m} - \frac{1}{T_{ref}^m} \right), \quad (3.14)$$

which contains five parameters:  $m$ ,  $A$ ,  $B$ ,  $T_{ref}$  and  $\mu_{ref}$ . Here,  $\mu$  is the viscosity at temperature  $T$ . Equation (3.14) may be rewritten in the following form:

$$\mu = (\mu_{ref} + B) \exp \left[ A \ln 10 \left( \frac{1}{T^m} - \frac{1}{T_{ref}^m} \right) \right] - B. \quad (3.15)$$

Here,  $\mu$  is the viscosity at temperature  $T$ . The parameters were determined using Shigley's [57] viscosity-temperature data for seven SAE oils. These are shown in Table 3.1. Viscosity-temperature plots are shown in Figure 3.3.

### 3.4 Initial and Boundary Conditions

Initial and boundary conditions for the general physical problem are given here. First, initial conditions are given. Second, boundary conditions are given.

The following generalized initial conditions are given for the lubricant velocity and temperature fields:

$$\begin{aligned} \text{at } t = 0 : \quad v_r = v_{r0}(r, \theta, z), \quad v_\theta = v_{\theta 0}(r, \theta, z), \quad v_z = v_{z0}(r, \theta, z), \\ \text{and} \quad T = T_0(r, \theta, z). \end{aligned} \quad (3.16)$$

Similarly, generalized initial conditions are given for the temperature fields within the material regions of the clutch plates:

$$\begin{aligned} \text{at } t = 0 : \quad T = T_{0f}(r, \theta, z_f) \quad ; \quad \text{for friction material,} \\ T = T_{0b}(r, \theta, z_b) \quad ; \quad \text{for backing material,} \\ T = T_{0s}(r, \theta, z_s) \quad ; \quad \text{for separator material.} \end{aligned} \quad (3.17)$$

It is further noted here that all bounding geometry and constraints are independent of time. For example, the relative angular velocity of the separator plate,  $\Omega_d$ , is taken as constant.

The classic no-slip condition is enforced on the clutch plate surfaces.

$$\begin{aligned} \text{on } z = 0 : \quad v_r = v_z = 0 \quad v_\theta = \Omega_d r \\ \text{on } z = h(r, \theta) : \quad v_r = v_\theta = v_z = 0 \end{aligned} \quad (3.18)$$

Here, the only nonhomogeneous condition relates the angular component of velocity, as viewed in the rotating frame, to the relative slip speed of the clutch.

The pressure is subjected to the following boundary conditions:

$$\begin{aligned} p(R_i, \theta) = p_i, \quad p(R_o, \theta) = p_o, \\ p(r, 0) = p(r, \theta_o), \quad \frac{\partial p(r, 0)}{\partial \theta} = \frac{\partial p(r, \theta_o)}{\partial \theta}. \end{aligned} \quad (3.19)$$

The pressure is prescribed at the inner and outer radii. The periodic conditions on pressure are to be expected from the geometry.

In the fluid, the inlet radial temperature,  $T_o$ , is prescribed. Further, a periodic condition on temperature is prescribed:

$$T(R_i, \theta, z) = T_o, \quad T(r, 0, z) = T(r, \theta_o, z). \quad (3.20)$$

The additional conditions for the temperature distribution couple the thermal and fluid problems. We require temperature and heat flux continuity at all axial interfaces:

$$\begin{aligned} T \Big|_{z_b=L_b} &= T \Big|_{z_f=0}, & T \Big|_{z_f=L_f+h_o-h} &= T \Big|_{z=h}, & T \Big|_{z_s=L_s} &= T \Big|_{z=0}, \\ \frac{\partial T}{\partial z_b} \Big|_{z_b=0} &= \frac{\partial T}{\partial z_s} \Big|_{z_s=0} = 0, & k_b \frac{\partial T}{\partial z_b} \Big|_{z_b=L_b} &= k_f \frac{\partial T}{\partial z_f} \Big|_{z_f=0}, & & \\ k_s \frac{\partial T}{\partial z_s} \Big|_{z_s=L_s} &= k \frac{\partial T}{\partial z} \Big|_{z=0}, & k_f \nabla_f T \cdot \mathbf{n}_f \Big|_{z_f=L_f+h_o-h} &= -k \nabla T \cdot \mathbf{n} \Big|_{z=h}. & & \end{aligned} \quad (3.21)$$

Here,  $\mathbf{n}_f$  and  $\mathbf{n}$  are unit outward normals to the friction and lubricant's surfaces at their common interface. Using the following relationships,

$$\begin{aligned} \nabla_f T &= \left[ \frac{\partial T}{\partial r} \quad \frac{1}{r} \frac{\partial T}{\partial \theta} \quad \frac{\partial T}{\partial z_f} \right]^T, \\ \nabla T &= \left[ \frac{\partial T}{\partial r} \quad \frac{1}{r} \frac{\partial T}{\partial \theta} \quad \frac{\partial T}{\partial z} \right]^T, \\ \mathbf{n}_f &= \left[ \frac{\partial h}{\partial r} \quad \frac{1}{r} \frac{\partial h}{\partial \theta} \quad 1 \right]^T \frac{1}{\sqrt{\left(\frac{\partial h}{\partial r}\right)^2 + \left(\frac{1}{r} \frac{\partial h}{\partial \theta}\right)^2 + 1}}, \\ \mathbf{n} &= \left[ -\frac{\partial h}{\partial r} \quad -\frac{1}{r} \frac{\partial h}{\partial \theta} \quad 1 \right]^T \frac{1}{\sqrt{\left(\frac{\partial h}{\partial r}\right)^2 + \left(\frac{1}{r} \frac{\partial h}{\partial \theta}\right)^2 + 1}}, \end{aligned}$$

the last of these conditions, given in Equation (3.21), may be simplified to the following equation:

$$(k_f - k) \left[ \frac{\partial h}{\partial r} \frac{\partial T}{\partial r} + \frac{1}{r^2} \frac{\partial h}{\partial \theta} \frac{\partial T}{\partial \theta} \right] \Big|_{z=h} + k \frac{\partial T}{\partial z} \Big|_{z=h} + k_f \frac{\partial T}{\partial z_f} \Big|_{z_f=L_f+h_o-h} = 0.$$

### 3.5 Non-Dimensionalization

The governing equations are non-dimensionalized in order to investigate the relative order of magnitude of the terms involved. The choice of scaling and typical values of dimensionless parameters will be discussed in this section.

#### 3.5.1 Choice of Scaling

First, the nondimensional independent spatial variables are defined as follows:

$$r_* = \frac{r}{R_i}, \quad \theta_* = \theta, \quad z_* = \frac{z}{h_o}. \quad (3.22)$$

The radius,  $r$ , was scaled by the inner clutch radius,  $R_i$ , and the axial coordinate,  $z$ , was scaled by the minimum film thickness,  $h_o$ . Again, the film thickness,  $h$ , is in general a function of the radial coordinate,  $r$ , and the angular coordinate,  $\theta$ .

Second, the components of velocity were scaled as follows:

$$v_r^* = \frac{v_r}{\Omega_1 R_i}, \quad v_\theta^* = \frac{v_\theta}{\Omega_1 R_i}, \quad v_z^* = \frac{v_z}{\Omega_1 h_o}. \quad (3.23)$$

These scalings are chosen such that all terms in the continuity equation are given equal significance. The angular component of velocity is scaled by the friction plate absolute velocity, or the input driving velocity of the clutch.

Third, the viscosity and temperature were non-dimensionalized. Again, the lubricant viscosity depends on temperature,  $\mu = \mu(T)$ . Assuming the lubricant's characteristic temperature is the radial inlet temperature,  $T_o$ , the characteristic viscosity is  $\mu_o = \mu(T_o)$ . The viscosity and temperature were scaled as follows:

$$\mu_* = \frac{\mu}{\mu_o}, \quad T_* = \frac{T}{T_o}. \quad (3.24)$$



Fourth, a dimensionless pressure was defined. Very large changes in pressure are expected to occur in small clearances where relative velocities exist. This premise of lubrication theory has motivated a widely accepted scaling of pressure [18, 22, 40]:

$$p_* = \frac{(p - p_i) h_o^2}{\mu_o \Omega_1 R_i^2}. \quad (3.25)$$

Here, the characteristic pressure,  $\frac{\mu_o \Omega_1 R_i^2}{h_o^2}$ , may be justified. If the clearance to radius ratio is small, pressures are expected to be high. Increases in the angular speed and/or viscosity are expected to increase the pressure. From Equation (3.19), the pressure,  $p_i$ , is the uniform pressure at the inner radius of the clutch. At  $r = R_o$ , the pressure is specified as  $p = p_o$ , or  $p_* = p_o^*$  in dimensionless terms.

Fifth, the time,  $t$ , was nondimensionalized. We assume that the appropriate time scale may be found by considering the rate of change of the no-slip boundary condition at the clutch surface. Here, we temporarily relax the previous statement that the boundary constraints are independent of time. A simple equation which relates the clutch frictional moment to the relative angular acceleration of the clutch is as follows:

$$I_2 \frac{d\Omega_d}{dt} = M_F = \int_{R_i}^{R_o} 2\pi r^2 \mu \frac{\partial v_\theta}{\partial z} dr. \quad (3.26)$$

In Equation (3.26), load torques,  $T_2$ , and the term  $\frac{\mu}{r} \frac{\partial v_z}{\partial \theta}$  in the  $\theta z$ -stress component have been neglected. Using the above dimensionless definitions and letting  $\Omega_*$  denote the ratio of relative speed to input speed,  $\Omega_* = \frac{\Omega_d}{\Omega_1}$ , we can non-dimensionalize Equation (3.26) as follows:

$$\frac{d\Omega_*}{dt_*} = \int_1^{R_*} 2\pi r_*^2 \mu_* \frac{\partial v_\theta^*}{\partial z_*} dr_*, \quad (3.27)$$

where,

$$t_* = \frac{\mu_o R_i^4}{h_o I_2} t. \quad (3.28)$$

Here,  $R_* = \frac{R_o}{R_i}$  is the ratio of outer to inner clutch radii. It is clear that increasing the viscosity will increase the torque delivered and decrease the time in which significant changes occur in the relative slip speed. Further, increasing the film size or output inertia would increase the time in which changes in the clutch slip speed occur.

Sixth, the dimensionless axial coordinates for the solid clutch plates were defined as follows:

$$z_b^* = \frac{z_b}{L_b}, \quad z_f^* = \frac{z_f}{L_f}, \quad z_s^* = \frac{z_s}{L_s}. \quad (3.29)$$

The notation used in Equation (3.29) corresponds to Figure 3.2. The corresponding radial and angular scaling in the solid material regions is defined in Equation (3.22).

### 3.5.2 Dimensionless Equations

The result of substituting the above dimensionless variable definitions, Equations (3.22-3.25), (3.28), and (3.29), and the constitutive equations, (3.9-3.13), into the governing equations, (3.1-3.8), the viscosity-temperature equation, (3.15), and the initial and boundary conditions, (3.16-3.21), is shown below:

$$\frac{1}{r_*} \frac{\partial}{\partial r_*} (r_* v_r^*) + \frac{1}{r_*} \frac{\partial v_\theta^*}{\partial \theta_*} + \frac{\partial v_z^*}{\partial z_*} = 0, \quad (3.30)$$

$$\begin{aligned} I_R \frac{\partial v_r^*}{\partial t_*} + \epsilon Re \left[ v_r^* \frac{\partial v_r^*}{\partial r_*} + \frac{v_\theta^*}{r_*} \frac{\partial v_r^*}{\partial \theta_*} + v_z^* \frac{\partial v_r^*}{\partial z_*} - \frac{1}{r_*} (v_\theta^* + r_*) \right] &= -\frac{\partial p_*}{\partial r_*} \\ + \frac{2\epsilon^2}{r_*} \frac{\partial}{\partial r_*} \left( \mu_* r_* \frac{\partial v_r^*}{\partial r_*} \right) + \frac{\epsilon^2}{r_*} \frac{\partial}{\partial \theta_*} \left[ \mu_* \left( r_* \frac{\partial}{\partial r_*} \left( \frac{v_\theta^*}{r_*} \right) + \frac{1}{r_*} \frac{\partial v_r^*}{\partial \theta_*} \right) \right] & \\ + \frac{\partial}{\partial z_*} \left[ \mu_* \left( \epsilon^2 \frac{\partial v_z^*}{\partial r_*} + \frac{\partial v_r^*}{\partial z_*} \right) \right] - \frac{2\mu_* \epsilon^2}{r_*} \left( \frac{1}{r_*} \frac{\partial v_\theta^*}{\partial \theta_*} + \frac{v_r^*}{r_*} \right), & \end{aligned} \quad (3.31)$$

$$\begin{aligned}
I_R \frac{\partial v_\theta^*}{\partial t_*} + \epsilon Re \left[ v_r^* \frac{\partial v_\theta^*}{\partial r_*} + \frac{v_\theta^*}{r_*} \frac{\partial v_\theta^*}{\partial \theta_*} + v_z^* \frac{\partial v_\theta^*}{\partial z_*} + \frac{v_r^* v_\theta^*}{r_*} + 2v_r^* \right] &= -\frac{1}{r_*} \frac{\partial p_*}{\partial \theta_*} \\
+ \frac{\epsilon^2}{r_*^2} \frac{\partial}{\partial r_*} \left[ \mu_* r_*^2 \left( r_* \frac{\partial}{\partial r_*} \left( \frac{v_\theta^*}{r_*} \right) + \frac{1}{r_*} \frac{\partial v_r^*}{\partial \theta_*} \right) \right] & \\
+ \frac{2\epsilon^2}{r_*} \frac{\partial}{\partial \theta_*} \left[ \mu_* \left( \frac{1}{r_*} \frac{\partial v_\theta^*}{\partial \theta_*} + \frac{v_r^*}{r_*} \right) \right] + \frac{\partial}{\partial z_*} \left[ \mu_* \left( \frac{\partial v_\theta^*}{\partial z_*} + \frac{\epsilon^2}{r_*} \frac{\partial v_z^*}{\partial \theta_*} \right) \right], & \quad (3.32)
\end{aligned}$$

$$\begin{aligned}
\epsilon^2 I_R \frac{\partial v_z^*}{\partial t_*} + \epsilon^3 Re \left[ v_r^* \frac{\partial v_z^*}{\partial r_*} + \frac{v_\theta^*}{r_*} \frac{\partial v_z^*}{\partial \theta_*} + v_z^* \frac{\partial v_z^*}{\partial z_*} \right] &= -\frac{\partial p_*}{\partial z_*} \\
+ \frac{1}{r_*} \frac{\partial}{\partial r_*} \left[ \mu_* r_* \left( \epsilon^4 \frac{\partial v_z^*}{\partial r_*} + \epsilon^2 \frac{\partial v_r^*}{\partial z_*} \right) \right] + \frac{\epsilon^2}{r_*} \frac{\partial}{\partial \theta_*} \left[ \mu_* \left( \frac{\partial v_\theta^*}{\partial z_*} + \frac{\epsilon^2}{r_*} \frac{\partial v_z^*}{\partial \theta_*} \right) \right] & \quad (3.33) \\
+ 2\epsilon^2 \frac{\partial}{\partial z_*} \left[ \mu_* \frac{\partial v_z^*}{\partial z_*} \right], &
\end{aligned}$$

$$\begin{aligned}
\frac{I_R Gr}{Re} \frac{\partial T_*}{\partial t_*} + \epsilon Gr \left[ v_r^* \frac{\partial T_*}{\partial r_*} + \frac{v_\theta^*}{r_*} \frac{\partial T_*}{\partial \theta_*} + v_z^* \frac{\partial T_*}{\partial z_*} \right] & \\
= \frac{\epsilon^3}{r_*} \frac{\partial}{\partial r_*} \left( r_* \frac{\partial T_*}{\partial r_*} \right) + \frac{\epsilon^3}{r_*^2} \frac{\partial^2 T_*}{\partial \theta_*^2} + \epsilon \frac{\partial^2 T_*}{\partial z_*^2} & \\
+ 2\epsilon^3 Br \mu_* \left[ \left( \frac{\partial v_r^*}{\partial r_*} \right)^2 + \left( \frac{1}{r_*} \frac{\partial v_\theta^*}{\partial \theta_*} + \frac{v_r^*}{r_*} \right)^2 + \left( \frac{\partial v_z^*}{\partial z_*} \right)^2 \right] & \quad (3.34) \\
+ Br \mu_* \left[ \epsilon^3 \left( \frac{1}{r_*} \frac{\partial v_r^*}{\partial \theta_*} - \frac{v_\theta^*}{r_*} + \frac{\partial v_\theta^*}{\partial r_*} \right)^2 + \left( \epsilon^{\frac{5}{2}} \frac{\partial v_z^*}{\partial r_*} + \epsilon^{\frac{1}{2}} \frac{\partial v_r^*}{\partial z_*} \right)^2 \right. \\
\left. + \left( \epsilon^{\frac{1}{2}} \frac{\partial v_\theta^*}{\partial z_*} + \frac{\epsilon^{\frac{5}{2}}}{r_*} \frac{\partial v_z^*}{\partial \theta_*} \right)^2 \right], &
\end{aligned}$$

$$\frac{I_R Pr}{\alpha_f^*} \frac{\partial T_*}{\partial t_*} = \frac{\epsilon^2}{r_*} \frac{\partial}{\partial r_*} \left( r_* \frac{\partial T_*}{\partial r_*} \right) + \frac{\epsilon^2}{r_*^2} \frac{\partial^2 T_*}{\partial \theta_*^2} + \frac{1}{L_f^{*2}} \frac{\partial^2 T_*}{\partial z_f^{*2}}, \quad (3.35)$$

$$\frac{I_R Pr}{\alpha_b^*} \frac{\partial T_*}{\partial t_*} = \frac{\epsilon^2}{r_*} \frac{\partial}{\partial r_*} \left( r_* \frac{\partial T_*}{\partial r_*} \right) + \frac{\epsilon^2}{r_*^2} \frac{\partial^2 T_*}{\partial \theta_*^2} + \frac{1}{L_b^{*2}} \frac{\partial^2 T_*}{\partial z_b^{*2}}, \quad (3.36)$$

$$\frac{I_R Pr}{\alpha_s^*} \frac{\partial T_*}{\partial t_*} + \frac{Gr \Omega_*}{\alpha_s^*} \frac{\partial T_*}{\partial \theta_*} = \frac{\epsilon^2}{r_*} \frac{\partial}{\partial r_*} \left( r_* \frac{\partial T_*}{\partial r_*} \right) + \frac{\epsilon^2}{r_*^2} \frac{\partial^2 T_*}{\partial \theta_*^2} + \frac{1}{L_s^{*2}} \frac{\partial^2 T_*}{\partial z_s^{*2}}, \quad (3.37)$$

$$\mu_* = \frac{(K_1^* + 1) \exp \left[ K_2^* \left( \frac{1}{T_*^m} - K_3^* m \right) \right] - 1}{(K_1^* + 1) \exp \left[ K_2^* (1 - K_3^* m) \right] - 1} \quad (3.38)$$

$$\text{at } t_* = 0: \quad v_r^* = v_{r0}^*(r_*, \theta_*, z_*), \quad v_\theta^* = v_{\theta 0}^*(r_*, \theta_*, z_*), \quad (3.39)$$

$$\text{and } v_z^* = v_{z0}^*(r_*, \theta_*, z_*), \quad T_* = T_0^*(r_*, \theta_*, z_*),$$

$$\begin{aligned} \text{at } t_* = 0: \quad T_* &= T_{0f}^*(r_*, \theta_*, z_f^*) \quad ; \quad \text{for friction material,} \\ T_* &= T_{0b}^*(r_*, \theta_*, z_b^*) \quad ; \quad \text{for backing material,} \end{aligned} \quad (3.40)$$

$$\begin{aligned} T_* &= T_{0s}^*(r_*, \theta_*, z_s^*) \quad ; \quad \text{for separator material,} \\ \text{on } z_* = 0: \quad v_r^* &= v_z^* = 0, \quad v_\theta^* = \Omega_* r_*, \end{aligned} \quad (3.41)$$

$$\text{on } z_* = h_* (r_*, \theta_*) : \quad v_r^* = v_\theta^* = v_z^* = 0,$$

$$\begin{aligned} p_*(1, \theta_*) &= 0, \quad p_*(R_*, \theta_*) = p_o^*, \\ p(r_*, 0) &= p(r_*, \theta_o), \quad \frac{\partial p_*}{\partial z_*}(r_*, 0) = \frac{\partial p_*}{\partial \theta_*}(r_*, \theta_o), \end{aligned} \quad (3.42)$$

$$T_*(1, \theta_*, z_*) = 1, \quad T_*(r_*, 0, z_*) = T_*(r_*, \theta_o, z_*), \quad (3.43)$$

$$\begin{aligned} T_* \Big|_{z_b^*=1} &= T_* \Big|_{z_f^*=0}, \quad T_* \Big|_{z_f^*=L_f^*+1-h_*} = T_* \Big|_{z_*=h_*}, \\ T_* \Big|_{z_s^*=1} &= T_* \Big|_{z_*=0}, \quad \frac{\partial T_*}{\partial z_b^*} \Big|_{z_b^*=0} = \frac{\partial T_*}{\partial z_s^*} \Big|_{z_s^*=0} = 0, \\ \frac{k_b^* L_f^*}{k_f^* L_b^*} \frac{\partial T_*}{\partial z_b^*} \Big|_{z_b^*=1} &= \frac{\partial T_*}{\partial z_f^*} \Big|_{z_f^*=0}, \quad \frac{k_s^*}{L_s^*} \frac{\partial T_*}{\partial z_s^*} \Big|_{z_s^*=1} = \frac{\partial T_*}{\partial z_*} \Big|_{z_*=0}, \\ \epsilon^2 (k_f^* - 1) \left[ \frac{\partial h_*}{\partial r_*} \frac{\partial T_*}{\partial r_*} + \frac{1}{r_*^2} \frac{\partial h_*}{\partial \theta_*} \frac{\partial T_*}{\partial \theta_*} \right] \Big|_{z_*=h_*} &+ \frac{\partial T_*}{\partial z_*} \Big|_{z_*=h_*} \\ &+ \frac{k_f^*}{L_f^*} \frac{\partial T_*}{\partial z_f^*} \Big|_{z_f^*=L_f^*+1-h_*} = 0. \end{aligned} \quad (3.44)$$

Here,  $\epsilon = \frac{h_o}{R_i}$  is the ratio of film thickness to inner radius,  $Re = \frac{\rho \Omega_1 R_i h_o}{\mu_o}$  is the Reynolds number,  $I_R = \frac{\rho R_i^4 h_o}{I_2}$  is the ratio of fluid inertia to output clutch inertia,  $Gr = \frac{\rho c \Omega_1 h_o^2}{k}$  is the Graetz number,  $Br = \frac{\mu_o \Omega_1^2 R_i^2}{k T_o}$  is the Brinkman number,  $v_{r0}^* = \frac{v_{r0}}{\Omega_1 R_i}$ ,  $v_{\theta 0}^* = \frac{v_{\theta 0}}{\Omega_1 R_i}$ ,  $v_{z0}^* = \frac{v_{z0}}{\Omega_1 h_o}$ ,  $T_0^* = \frac{T_0}{T_o}$ ,  $T_{0f}^* = \frac{T_{0f}}{T_o}$ ,  $T_{0b}^* = \frac{T_{0b}}{T_o}$ , and  $T_{0s}^* = \frac{T_{0s}}{T_o}$  are the initial dimensionless velocity and temperature profiles,  $\Omega_* = \frac{\Omega}{\Omega_1}$  is the ratio of relative speed to input speed,  $Pr = \frac{\mu_o c}{k}$  is the Prandtl number,  $K_1^* = \frac{\mu_{ref}}{B}$ ,  $K_2^* = \frac{A \ln 10}{T_o^n}$ , and  $K_3^* = \frac{T_o}{T_{ref}}$  are dimensionless parameters found in the viscosity-temperature equation,

$$\begin{aligned}
h_o &= 5.0 \times 10^{-5} \text{ m} & R_i &= 5.0 \times 10^{-2} \text{ m} & R_o &= 6.5 \times 10^{-2} \text{ m} & \theta_o &= 0.2 \text{ rad} \\
\Omega_1 &= 50 \frac{\text{rad}}{\text{s}} & \Omega_d &= 50 \frac{\text{rad}}{\text{s}} & p_i &= 1.4 \times 10^6 \text{ Pa} & p_o &= 7.0 \times 10^5 \text{ Pa} \\
\rho &= 830 \frac{\text{kg}}{\text{m}^3} & \rho_f &= 8800 \frac{\text{kg}}{\text{m}^3} & \rho_b &= 7800 \frac{\text{kg}}{\text{m}^3} & \rho_s &= 7800 \frac{\text{kg}}{\text{m}^3} \\
c &= 2.0 \times 10^3 \frac{\text{J}}{\text{kg K}} & c_f &= 4.2 \times 10^2 \frac{\text{J}}{\text{kg K}} & c_b &= 4.3 \times 10^2 \frac{\text{J}}{\text{kg K}} & c_s &= 4.3 \times 10^2 \frac{\text{J}}{\text{kg K}} \\
k &= 0.14 \frac{\text{W}}{\text{m K}} & k_f &= 50.0 \frac{\text{W}}{\text{m K}} & k_b &= 65.0 \frac{\text{W}}{\text{m K}} & k_s &= 65.0 \frac{\text{W}}{\text{m K}} \\
T_o &= 400 \text{ K} & \mu_o &= 2.5 \times 10^{-3} \frac{\text{Ns}}{\text{m}^2} & I_2 &= 2.6 \text{ kg m}^2 & L_f &= 2.5 \times 10^{-4} \text{ m} \\
L_b &= 2.5 \times 10^{-4} \text{ m} & L_s &= 2.5 \times 10^{-4} \text{ m} & & & &
\end{aligned}$$

Table 3.2: TYPICAL CLUTCH OPERATING CONDITIONS

$h_* = \frac{h}{h_o}$  is the dimensionless film thickness,  $\alpha_f^* = \frac{k_f \rho c}{k \rho_f c_f}$ ,  $\alpha_b^* = \frac{k_b \rho c}{k \rho_b c_b}$ , and  $\alpha_s^* = \frac{k_s \rho c}{k \rho_s c_s}$  are respectively the ratios of friction, backing, and separator thermal diffusivities to lubricant thermal diffusivity,  $L_f^* = \frac{L_f}{h_o}$ ,  $L_b^* = \frac{L_b}{h_o}$ , and  $L_s^* = \frac{L_s}{h_o}$  are respectively the ratios of friction, backing, and separator axial lengths to minimum film thickness, and  $k_f^* = \frac{k_f}{k}$ ,  $k_b^* = \frac{k_b}{k}$ , and  $k_s^* = \frac{k_s}{k}$  are respectively the ratios of friction, backing, and separator thermal conductivities to lubricant thermal conductivity.

### 3.5.3 Simplifications

For the equations of motion at hand, the primary dimensionless groups are analyzed at typical operating conditions listed in Table 3.2. The range of parameters studied in this dissertation are listed in Table 3.3. These values were used to calculate dimensionless operating conditions listed in Table 3.4. The ranges of dimensionless parameters studied in this dissertation are listed in Table 3.5. In some instances,

$$\begin{aligned}
3 \times 10^{-6} \text{ m} \leq h_o \leq 2.0 \times 10^{-4} \text{ m} & \quad 50 \frac{\text{rad}}{\text{s}} \leq \Omega_d \leq 200 \frac{\text{rad}}{\text{s}} \\
0.5 \text{ MPa} \leq p_o \leq 2.0 \text{ MPa} & \quad 300 \text{ K} \leq T_o \leq 500 \text{ K} \\
1.0 \times 10^{-3} \frac{\text{Ns}}{\text{m}^2} \leq \mu_o \leq 7.0 \times 10^{-2} \frac{\text{Ns}}{\text{m}^2}
\end{aligned}$$

Table 3.3: RANGE OF PARAMETERS STUDIED

$$\begin{aligned}
\epsilon = \frac{h_o}{R_i} = 1.0 \times 10^{-3} & \quad Re = \frac{\rho \Omega_1 R_i h_o}{\mu_o} = 42 & \quad I_R = \frac{\rho R_i^4 h_o}{I_2} = 1.0 \times 10^{-7} \\
Gr = \frac{\rho c \Omega_1 h_o^2}{k} = 1.5 & \quad Br = \frac{\mu_o \Omega_1^2 R_i^2}{k T_o} = 2.8 \times 10^{-4} & \quad \Omega_* = \frac{\Omega_d}{\Omega_1} = 1 \\
Pr = \frac{\mu_o c}{k} = 36 & \quad \alpha_f^* = \frac{k_f \rho c}{k \rho_f c_f} = 160 & \quad \alpha_b^* = \frac{k_b \rho c}{k \rho_b c_b} = 230 \\
\alpha_s^* = \frac{k_s \rho c}{k \rho_s c_s} = 230 & \quad L_f^* = \frac{L_f}{h_o} = 5 & \quad L_b^* = \frac{L_b}{h_o} = 5 \\
L_s^* = \frac{L_s}{h_o} = 5 & \quad R_* = \frac{R_o}{R_i} = 1.3 & \quad p_o^* = \frac{(p_o - p_i) h_o^2}{\mu_o \Omega_1 R_i^2} = -5.6 \\
K_1^* = \frac{K_1}{\mu_o} = 0.33 & \quad K_2^* = \frac{K_2}{T_o} = 1.1 & \quad K_3^* = \frac{k_3}{\mu_o} = -0.15
\end{aligned}$$

Table 3.4: TYPICAL CLUTCH DIMENSIONLESS PARAMETERS

$$\begin{aligned}
6 \times 10^{-5} \leq \epsilon = \frac{h_o}{R_i} \leq 4.0 \times 10^{-3} \\
9 \times 10^{-5} \leq Br = \frac{\mu_o \Omega_1^2 R_i^2}{k T_o} \leq 0.16 \\
5 \times 10^{-3} \leq Gr = \frac{\rho c \Omega_1 h_o^2}{k} \leq 105
\end{aligned}$$

Table 3.5: RANGE OF DIMENSIONLESS PARAMETERS STUDIED

a best guess is made for the operating conditions. The radii,  $R_i$  and  $R_o$ , and axial lengths,  $L_b$ ,  $L_s$ , and  $L_f$ , are based on a Clark 18000 forward first clutch. The material and lubricant properties are based on steel for the backing and separator materials, commercial bronze for the friction material, and SAE 10 for the lubricant. It is noted that the operating parameters could significantly change the Brinkman and Graetz numbers via the film size, input speed, and viscosity-temperature relation. Further discussion on these parameter ranges is given shortly.

In view of the dimensionless numbers predicted, the following arguments are made to simplify the governing equations:

1. All dimensionless variables,  $t_*$ ,  $r_*$ ,  $\theta_*$ ,  $z_*$ ,  $v_r^*$ ,  $v_\theta^*$ ,  $v_z^*$ ,  $p_*$ ,  $T_*$ , and  $\mu_*$ , are  $O(1)$ .
2. The ratio of fluid to solid inertia,  $I_R$ , is negligible.
3. The solid to fluid thermal diffusivity ratios,  $\alpha_f^*$ ,  $\alpha_b^*$ , and  $\alpha_s^*$ , are large.
4. The film thickness to inner radius ratio,  $\epsilon$ , is small.
5. The film thickness,  $h_* = h_*(r_*, \theta_*)$ , has no severe spatial gradients.

The consequence of the second assumption is that time variations in the model are ignored. We consider steady state solutions which satisfy the governing equations and boundary conditions. In this long time limit, the initial conditions, Equations (3.39) and (3.40), are omitted. Gross [18] gives an excellent discussion as to why time variations in lubrication problems can usually be neglected.

### 3.6 Summarized Problem Statement

Using the assumptions presented in the previous section, the relevant dimensionless governing equations and boundary conditions are summarized below:

$$\frac{\partial (r_* v_r^*)}{\partial r_*} + \frac{\partial v_\theta^*}{\partial \theta_*} + r_* \frac{\partial v_z^*}{\partial z_*} = 0, \quad (3.45)$$

$$\frac{\partial p_*}{\partial r_*} = \frac{\partial}{\partial z_*} \left( \mu_* \frac{\partial v_r^*}{\partial z_*} \right), \quad (3.46)$$

$$\frac{1}{r_*} \frac{\partial p_*}{\partial \theta_*} = \frac{\partial}{\partial z_*} \left( \mu_* \frac{\partial v_\theta^*}{\partial z_*} \right), \quad (3.47)$$

$$\frac{\partial p_*}{\partial z_*} = 0, \quad (3.48)$$

$$Gr \left[ v_r^* \frac{\partial T_*}{\partial r_*} + \frac{v_\theta^*}{r_*} \frac{\partial T_*}{\partial \theta_*} + v_z^* \frac{\partial T_*}{\partial z_*} \right] = \frac{\partial^2 T_*}{\partial z_*^2} + \mu_* Br \left[ \left( \frac{\partial v_r^*}{\partial z_*} \right)^2 + \left( \frac{\partial v_\theta^*}{\partial z_*} \right)^2 \right], \quad (3.49)$$

$$\frac{\partial^2 T_*}{\partial z_f^{*2}} = 0, \quad (3.50)$$

$$\frac{\partial^2 T_*}{\partial z_b^{*2}} = 0, \quad (3.51)$$

$$\frac{\partial^2 T_*}{\partial z_s^{*2}} = 0, \quad (3.52)$$

$$\mu_* = \frac{(K_1^* + 1) \exp \left[ K_2^* \left( \frac{1}{T_*^m} - K_3^* m \right) \right] - 1}{(K_1^* + 1) \exp \left[ K_2^* (1 - K_3^* m) \right] - 1} \quad (3.53)$$

$$\text{on } z_* = 0 : \quad v_r^* = v_z^* = 0, \quad v_\theta^* = \Omega_* r_*, \quad (3.54)$$

$$\text{on } z_* = h_* : \quad v_r^* = v_\theta^* = v_z^* = 0,$$

$$\begin{aligned} p_*(1, \theta_*) &= 0, & p_*(R_*, \theta_*) &= p_o^*, \\ p(r_*, 0) &= p(r_*, \theta_o), & \frac{\partial p_*}{\partial \theta_*}(r_*, 0) &= \frac{\partial p_*}{\partial \theta_*}(r_*, \theta_o), \end{aligned} \quad (3.55)$$



$$T_*(1, \theta_*, z_*) = 1, \quad T_*(r_*, 0, z_*) = T_*(r_*, \theta_o, z_*), \quad (3.56)$$

$$\begin{aligned} T_* \Big|_{z_b^*=1} &= T_* \Big|_{z_f^*=0}, & T_* \Big|_{z_f^*=L_f^*+1-h_*} &= T_* \Big|_{z_*=h_*}, \\ T_* \Big|_{z_s^*=1} &= T_* \Big|_{z_*=0}, & \frac{\partial T_*}{\partial z_b^*} \Big|_{z_b^*=0} &= \frac{\partial T_*}{\partial z_s^*} \Big|_{z_s^*=0} = 0, \\ \frac{k_b^* L_f^*}{k_f^* L_b^*} \frac{\partial T_*}{\partial z_b^*} \Big|_{z_b^*=1} &= \frac{\partial T_*}{\partial z_f^*} \Big|_{z_f^*=0}, & \frac{k_s^*}{L_s^*} \frac{\partial T_*}{\partial z_s^*} \Big|_{z_s^*=1} &= \frac{\partial T_*}{\partial z_*} \Big|_{z_*=0}, \\ \frac{k_f^*}{L_f^*} \frac{\partial T_*}{\partial z_f^*} \Big|_{z_f^*=L_f^*+1-h_*} &= -\frac{\partial T_*}{\partial z_*} \Big|_{z_*=h_*}. \end{aligned} \quad (3.57)$$

The first four of these equations, (3.45-3.48), are the classical incompressible lubrication equations from which a Reynolds equation may be found. In this simplified energy equation for the lubricant, (3.49), we are allowing for viscous dissipation to heat the clutch and convection to cool the clutch. In particular, one will note that the Brinkman number given in Table 3.4 is significantly lower than  $O(1)$ . This suggests that viscous dissipation could safely be neglected given the operating conditions stated in Table 3.2. Nevertheless, we make no such assumption regarding the viscous dissipation for two reasons mentioned here. First, having neglected asperity contact, viscous dissipation is the *only* source of heat generation for this problem. In reality, the solid to solid rubbing of clutch plates significantly increases the clutch temperature. Second, the scalings given are not the most judicious choice. As indicated previously, the range of the Brinkman and Graetz numbers is fairly broad. It was found *a posteriori* that while the terms in the energy equation balance, the order of magnitude of these quantities is not  $O(1)$ . However, as the Brinkman and Graetz numbers approach unity, the ordering of the energy balance terms becomes exact. This is shown in the results for a specific set of operating conditions for various Graetz and Brinkman numbers.

Comparing the last condition in Equation (3.44) to the last condition in Equation (3.57), the leading term having the factor  $\epsilon^2$  was omitted. Here, it was not only assumed that  $\epsilon$  was small, but that the gradients  $\frac{\partial h_*}{\partial r_*}$  and  $\frac{\partial h_*}{\partial \theta_*}$  are  $O(1)$ .

Two obvious conclusions follow immediately from Equations (3.48) and (3.50-3.52): (1) the pressure is independent of the axial coordinate, and (2) the temperature distribution is axially linear in the solid clutch plates. In other words,

$$p_* = p_*(r_*, \theta_*), \quad (3.58)$$

$$T_* = C_1^f(r_*, \theta_*) z_f^* + C_2^f(r_*, \theta_*),$$

$$T_* = C_1^b(r_*, \theta_*) z_b^* + C_2^b(r_*, \theta_*), \quad (3.59)$$

$$T_* = C_1^s(r_*, \theta_*) z_s^* + C_2^s(r_*, \theta_*).$$

Further, from Equations (3.57) and (3.59), the following simplified boundary conditions on the lubricant may be deduced:

$$\left. \frac{\partial T_*}{\partial z_*} \right|_{z_*=0} = \left. \frac{\partial T_*}{\partial z_*} \right|_{z_*=h_*} = 0. \quad (3.60)$$

This is shown in Appendix A. In addition, it may be shown that the temperature distribution in both the backing and friction materials is  $T_* = T_* \Big|_{z_*=h_*}$  and in the separator plates,  $T_* = T_* \Big|_{z_*=0}$ . Mathematically, Equation (3.60) decouples the fluid problem from the thermal problem.

The dimensionless set of equations, (3.45-3.57) are sufficient to determine the velocity, pressure, and temperature in the lubricant and solid clutch plates given a periodic, but otherwise arbitrary, film shape.

### 3.7 Algebraic Coordinate Transformation

The following algebraic mapping transforms the independent physical variables into the working set of independent transformed variables:

$$\begin{aligned}\bar{r} &= \frac{r_* - 1}{R_* - 1} & 1 \leq r_* \leq R_*, \\ \bar{\theta} &= \frac{\theta_*}{\theta_o} & 0 \leq \theta_* \leq \theta_o, \\ \bar{z} &= \frac{z_*}{h_*(r_*, \theta_*)} & 0 \leq z_* \leq h_*(r_*, \theta_*).\end{aligned}\tag{3.61}$$

The transformed domain is thus:  $0 \leq \bar{r} \leq 1$ ,  $0 \leq \bar{\theta} \leq 1$ , and  $0 \leq \bar{z} \leq 1$ . The pertinent metrics for the above transformation are elements of the Jacobian matrix,  $J$ :

$$\begin{aligned}J &= \begin{bmatrix} \frac{\partial \bar{r}}{\partial r_*} & \frac{\partial \bar{r}}{\partial \theta_*} & \frac{\partial \bar{r}}{\partial z_*} \\ \frac{\partial \bar{\theta}}{\partial r_*} & \frac{\partial \bar{\theta}}{\partial \theta_*} & \frac{\partial \bar{\theta}}{\partial z_*} \\ \frac{\partial \bar{z}}{\partial r_*} & \frac{\partial \bar{z}}{\partial \theta_*} & \frac{\partial \bar{z}}{\partial z_*} \end{bmatrix} = \begin{bmatrix} \frac{1}{(R_* - 1)} & 0 & 0 \\ 0 & \frac{1}{\theta_o} & 0 \\ -\frac{z_*}{h_*^2} \frac{\partial h_*}{\partial r_*} & -\frac{z_*}{h_*^2} \frac{\partial h_*}{\partial \theta_*} & \frac{1}{h_*} \end{bmatrix} \\ &= \begin{bmatrix} \frac{1}{(R_* - 1)} & 0 & 0 \\ 0 & \frac{1}{\theta_o} & 0 \\ -\frac{\bar{z}}{h_*} \frac{1}{(R_* - 1)} \frac{\partial h_*}{\partial \bar{r}} & -\frac{\bar{z}}{h_*} \frac{1}{\theta_o} \frac{\partial h_*}{\partial \bar{\theta}} & \frac{1}{h_*} \end{bmatrix}.\end{aligned}\tag{3.62}$$

Note that the off-diagonal terms in Equation (3.62) are present due to the arbitrarily defined film thickness,  $h_* = h_*(\bar{r}, \bar{\theta})$ . The final matrix in Equation (3.62) is desirable because all terms are expressed in terms of the working transformed variables.

Derivatives in the governing equations may be expressed using the chain rule for

partial differentiation:

$$\begin{bmatrix} \frac{\partial}{\partial r_*} \\ \frac{\partial}{\partial \theta_*} \\ \frac{\partial}{\partial z_*} \end{bmatrix} = \begin{bmatrix} \frac{\partial \bar{r}}{\partial r_*} & \frac{\partial \bar{\theta}}{\partial r_*} & \frac{\partial \bar{z}}{\partial r_*} \\ \frac{\partial \bar{r}}{\partial \theta_*} & \frac{\partial \bar{\theta}}{\partial \theta_*} & \frac{\partial \bar{z}}{\partial \theta_*} \\ \frac{\partial \bar{r}}{\partial z_*} & \frac{\partial \bar{\theta}}{\partial z_*} & \frac{\partial \bar{z}}{\partial z_*} \end{bmatrix} \begin{bmatrix} \frac{\partial}{\partial \bar{r}} \\ \frac{\partial}{\partial \bar{\theta}} \\ \frac{\partial}{\partial \bar{z}} \end{bmatrix}. \quad (3.63)$$

The matrix given in Equation (3.63) is the transpose of the Jacobian matrix given in Equation (3.62). Further use of the chain rule may be employed to evaluate second derivatives in the governing equations:

$$\begin{aligned} \frac{\partial^2}{\partial z_*^2} &= \frac{\partial}{\partial z_*} \left( \frac{\partial}{\partial z_*} \right) = \frac{\partial}{\partial z_*} \left( \frac{\partial \bar{r}}{\partial z_*} \frac{\partial}{\partial \bar{r}} + \frac{\partial \bar{\theta}}{\partial z_*} \frac{\partial}{\partial \bar{\theta}} + \frac{\partial \bar{z}}{\partial z_*} \frac{\partial}{\partial \bar{z}} \right) \\ &= \frac{\partial}{\partial z_*} \left( \frac{1}{h_*} \frac{\partial}{\partial \bar{z}} \right) = \frac{1}{h_*} \frac{\partial}{\partial \bar{z}} \left( \frac{1}{h_*} \frac{\partial}{\partial \bar{z}} \right) = \frac{1}{h_*^2} \frac{\partial^2}{\partial \bar{z}^2}. \end{aligned}$$

Only second derivatives in  $z_*$  appear in the governing equations.

The mass, momentum, and energy equations for the lubricant, (3.45-3.49), are written in terms of the working transformed variables and metrics as follows:

$$\begin{aligned} \frac{1}{(R_* - 1)} \left[ h_* \frac{\partial}{\partial \bar{r}} [(\bar{r} [R_* - 1] + 1) v_r^*] - \bar{z} \frac{\partial h_*}{\partial \bar{r}} \frac{\partial}{\partial \bar{z}} [(\bar{r} [R_* - 1] + 1) v_r^*] \right] \\ \frac{1}{\theta_o} \left[ h_* \frac{\partial v_\theta^*}{\partial \bar{\theta}} - \bar{z} \frac{\partial h_*}{\partial \bar{\theta}} \frac{\partial v_\theta^*}{\partial \bar{z}} \right] + [\bar{r} (R_* - 1) + 1] \frac{\partial v_z^*}{\partial \bar{z}} = 0, \end{aligned} \quad (3.64)$$

$$\frac{h_*^2}{(R_* - 1)} \frac{\partial p_*}{\partial \bar{r}} = \frac{\partial}{\partial \bar{z}} \left( \mu_* \frac{\partial v_r^*}{\partial \bar{z}} \right), \quad (3.65)$$

$$\frac{h_*^2}{[\bar{r} (R_* - 1) + 1] \theta_o} \frac{\partial p_*}{\partial \bar{\theta}} = \frac{\partial}{\partial \bar{z}} \left( \mu_* \frac{\partial v_\theta^*}{\partial \bar{z}} \right), \quad (3.66)$$

$$\frac{\partial p_*}{\partial \bar{z}} = 0, \quad (3.67)$$

$$\begin{aligned} \frac{Gr h_*^2 v_r^*}{(R_* - 1)} \frac{\partial T_*}{\partial \bar{r}} + \frac{Gr h_*^2 v_\theta^*}{[\bar{r} (R_* - 1) + 1] \theta_o} \frac{\partial T_*}{\partial \bar{\theta}} \\ + Gr h_* \left[ v_z^* - \frac{v_r^* \bar{z}}{(R_* - 1)} \frac{\partial h_*}{\partial \bar{r}} - \frac{v_\theta^* \bar{z}}{[\bar{r} (R_* - 1) + 1]} \frac{\partial h_*}{\partial \bar{\theta}} \frac{1}{\theta_o} \right] \frac{\partial T_*}{\partial \bar{z}} \\ - \frac{\partial^2 T_*}{\partial \bar{z}^2} = \mu_* Br \left[ \left( \frac{\partial v_r^*}{\partial \bar{z}} \right)^2 + \left( \frac{\partial v_\theta^*}{\partial \bar{z}} \right)^2 \right]. \end{aligned} \quad (3.68)$$

The boundary conditions on the lubricant, Equations (3.54-3.56) and (3.60), are also written in terms of transformed variables:

$$\text{on } \bar{z} = 0 : \quad v_r^* = v_z^* = 0 \quad v_\theta^* = \Omega_* r_*, \quad (3.69)$$

$$\text{on } \bar{z} = 1 : \quad v_r^* = v_\theta^* = v_z^* = 0,$$

$$p_*(0, \bar{\theta}) = 0, \quad p_*(1, \bar{\theta}) = p_o^*, \quad (3.70)$$

$$p_*(\bar{r}, 0) = p_*(\bar{r}, 1), \quad \frac{\partial p_*}{\partial \bar{\theta}}(\bar{r}, 0) = \frac{\partial p_*}{\partial \bar{\theta}}(\bar{r}, 1),$$

$$T_*(1, \bar{\theta}, \bar{z}) = 1, \quad T_*(\bar{r}, 0, \bar{z}) = T_*(\bar{r}, 1, \bar{z}), \quad (3.71)$$

$$\left. \frac{\partial T_*}{\partial \bar{z}} \right|_{\bar{z}=0} = \left. \frac{\partial T_*}{\partial \bar{z}} \right|_{\bar{z}=1} = 0. \quad (3.72)$$

The above equations, (3.64-3.72), the viscosity-temperature relation, (3.53), and a specified film thickness,  $h_* = h_*(\bar{r}, \bar{\theta})$ , are sufficient to determine the velocity components, pressure, and temperature in the transformed domain.

In summary, this algebraic coordinate transformation is advantageous because it generalizes the problem to account for an arbitrary film shape. Furthermore, the transformed domain is a unit cube rather than a complex figure. Thus, we have dramatically simplified the geometry at the expense of a more complicated set of governing equations. Discussions on generalized algebraic transformations are given by Fletcher [17] and Minkowycz, Sparrow, Schneider, and Pletcher [37], and Hirsch [25]. Further, Wirz and Smolderen [67] list and discuss other options to consider in numerically solving problems in irregular domains.

A subtle critique of the mathematical model's development is mentioned here. The philosophy used to obtain the governing equations went as follows: (1) state the governing equation, (2) non-dimensionalize the equations, (3) simplify the equations.

and (4) transform the equations into a domain of manageable form. If the domain was transformed prior to the simplifications, additional terms would be present in the governing equations. For example, the conduction term in the radial direction is of the form:  $\frac{1}{r_*} \frac{\partial}{\partial r_*} \left( r_* \frac{\partial T}{\partial r_*} \right)$ . In terms of computational variables this term is as follows:

$$\begin{aligned} \frac{1}{r_*} \frac{\partial}{\partial r_*} \left( r_* \frac{\partial T}{\partial r_*} \right) &= \frac{1}{r_*} \left[ \frac{\partial}{\partial \bar{r}} \left( r_* \left[ \frac{\partial T_*}{\partial \bar{r}} \frac{\partial \bar{r}}{\partial r_*} + \frac{\partial T_*}{\partial \bar{z}} \frac{\partial \bar{z}}{\partial r_*} \right] \right) \frac{\partial \bar{r}}{\partial r_*} \right. \\ &\quad \left. + \frac{\partial}{\partial \bar{z}} \left( r_* \left[ \frac{\partial T_*}{\partial \bar{r}} \frac{\partial \bar{r}}{\partial r_*} + \frac{\partial T_*}{\partial \bar{z}} \frac{\partial \bar{z}}{\partial r_*} \right] \right) \frac{\partial \bar{r}}{\partial r_*} \right]. \end{aligned}$$

Some of these terms become significant when steep geometrical gradients are present. A thorough approach would first transform the governing equations, identify the appropriate scalings for all the terms in the scaled equations, and finally simplify the equations.

### 3.8 Clutch Performance Parameters

On finding a solution to the system of equations presented in the previous section, it is possible to study clutch performance within the regime of hydrodynamic lubrication. The quantities of interest, for a wet disk clutch, are the radial volumetric flow rate, the normal load capacity, tangential forces, the frictional moment, and the friction coefficient. These clutch performance parameters will be discussed, defined, and non-dimensionalized in this section. A detailed formulation of the definitions of these quantities is given by Hamrock [22].

A new dimensionless parameter which depends on the input conditions appears in this section. The *Sommerfeld number* is defined as follows:

$$S = \frac{\mu_o \Omega_1 R_i^2}{p_i h_o^2}. \quad (3.73)$$

This dimensionless number is sometimes referred to as the *Bearing characteristic number* [18].

### 3.8.1 Radial Volumetric Flow Rate

The total volume flow rate in the radial direction across the clutch, is defined as follows:

$$Q_r = N_g r \int_0^{\theta_o} \int_0^{h(r,\theta)} v_r(r, \theta, z) dz d\theta. \quad (3.74)$$

Here,  $N_g = \frac{2\pi}{\theta_o}$ , is the total number of periodic domains on the clutch friction plate. Given a set of operating conditions, this equation is used to obtain a relationship between the supply pressure and the flow rate. In terms of the working transformed variables, Equation (3.74) may be written as follows:

$$Q_r^* = \frac{Q_r}{\Omega_1 R_i^2 h_o} = N_g \theta_o [\bar{r}(R_* - 1) + 1] \int_0^1 h_* (\bar{r}, \bar{\theta}) \int_0^1 v_r^* (\bar{r}, \bar{\theta}, \bar{z}) d\bar{z} d\bar{\theta}. \quad (3.75)$$

### 3.8.2 Normal Load

The total normal load supported by the lubricant is the pressure integrated over the clutch surface.

$$F_z = N_g \int_0^{\theta_o} \int_{R_i}^{R_o} p(r, \theta) r dr d\theta \quad (3.76)$$

Given a set of operating conditions, this equation may be used to obtain a relationship between the film thickness and the normal load. In other words, in practical applications the minimum film thickness is typically not known *a priori*. The above

equation facilitates a mean by which the film thickness can be found. Equation (3.76)

may be written in terms of the transformed variables as follows:

$$F_z^* = \frac{F_z}{p_i \pi (R_o^2 - R_i^2)} = 1 + \frac{SN_g \theta_o}{\pi (R_* + 1)} \int_0^1 \int_0^1 p_* (\bar{r}, \bar{\theta}) [\bar{r} (R_* - 1) + 1] d\bar{r} d\bar{\theta}. \quad (3.77)$$

### 3.8.3 Tangential Forces

The tangential forces on the clutch may be decomposed into two types. They are (1) the tangential forces due to viscous shearing and (2) the tangential forces due to pressure. Since the clutch separator plate is defined to be in the  $z = 0$  plane, the tangential force due to pressure on the separator plate is zero. However at the friction plate,  $z = h(r, \theta)$ , the tangential force due to pressure is non-trivial. This tangential force may be expressed as follows:

$$F_{p,h} = -N_g \int_0^{\theta_o} \int_{R_i}^{R_o} p(r, \theta) \frac{\partial h}{\partial \theta}(r, \theta) dr d\theta. \quad (3.78)$$

Note that when the film is axisymmetric,  $\frac{\partial h}{\partial \theta} = 0$ , the tangential force due to pressure vanishes. Equation (3.78) is written in terms of the working transformed variables as follows:

$$F_{p,h}^* = \frac{F_{p,h}}{p_i \pi (R_o^2 - R_i^2)} = -\frac{\epsilon N_g}{\pi (R_* + 1)} \int_0^1 \int_0^1 \frac{\partial h_*}{\partial \bar{\theta}}(\bar{r}, \bar{\theta}) [Sp_* (\bar{r}, \bar{\theta}) + 1] d\bar{r} d\bar{\theta}. \quad (3.79)$$

The tangential forces due to viscous shearing occur on both the separator plate and the friction plate. They depend on the shear stress evaluated at  $z = 0$  and  $z = h$  respectively.

$$F_{\theta,0} = N_g \int_0^{\theta_o} \int_{R_i}^{R_o} \left( \mu(r, \theta, z) \frac{\partial v_{\theta}}{\partial z}(r, \theta, z) \right) \Big|_{z=0} r dr d\theta \quad (3.80)$$



$$F_{\theta,h} = -N_g \int_0^{\theta_o} \int_{R_i}^{R_o} \left( \mu(r, \theta, z) \frac{\partial v_{\theta}}{\partial z}(r, \theta, z) \right) \Big|_{z=h(r,\theta)} r dr d\theta \quad (3.81)$$

In general, these quantities are not equal and opposite. However, since the lubricant is not accelerating, it is known that  $F_{\theta,0} + F_{\theta,h} + F_{p,h} = 0$ . This relation offers a valuable check to results obtained. These equations may be written in terms of the transformed variables as follows:

$$\begin{aligned} F_{\theta,0}^* &= \frac{F_{\theta,0}}{p_i \pi (R_o^2 - R_i^2)} \\ &= \frac{S \epsilon N_g \theta_o}{\pi (R_* + 1)} \int_0^1 \int_0^1 \left( \mu_* (\bar{r}, \bar{\theta}, \bar{z}) \frac{\partial v_{\theta}^*}{\partial \bar{z}} (\bar{r}, \bar{\theta}, \bar{z}) \right) \Big|_{\bar{z}=0} \frac{[\bar{r} (R_* - 1) + 1]}{h_* (\bar{r}, \bar{\theta})} d\bar{r} d\bar{\theta}, \end{aligned} \quad (3.82)$$

$$\begin{aligned} F_{\theta,0}^* &= \frac{F_{\theta,0}}{p_i \pi (R_o^2 - R_i^2)} \\ &= -\frac{S \epsilon N_g \theta_o}{\pi (R_* + 1)} \int_0^1 \int_0^1 \left( \mu_* (\bar{r}, \bar{\theta}, \bar{z}) \frac{\partial v_{\theta}^*}{\partial \bar{z}} (\bar{r}, \bar{\theta}, \bar{z}) \right) \Big|_{\bar{z}=1} \frac{[\bar{r} (R_* - 1) + 1]}{h_* (\bar{r}, \bar{\theta})} d\bar{r} d\bar{\theta}. \end{aligned} \quad (3.83)$$

### 3.8.4 Frictional Moment Delivered

The frictional moment delivered to the separator plate is the shear stress at  $z = 0$  multiplied by the radius integrated over the clutch surface.

$$M_F = N_g \int_0^{\theta_o} \int_{R_i}^{R_o} \left( \mu(r, \theta, z) \frac{\partial v_{\theta}}{\partial z}(r, \theta, z) \right) \Big|_{z=0} r^2 dr d\theta \quad (3.84)$$

This quantity represents only a fraction of the total moment delivered to the output side of the transmission. In general, a clutch pack has multiple interfaces which generate frictional torque. The frictional moment may be defined in terms of computational

variables as follows:

$$\begin{aligned}
 M_F^* &= \frac{M_F}{p_i \pi (R_o^2 - R_i^2) R_i} \\
 &= \frac{S \epsilon N_g \theta_o}{\pi (R_* + 1)} \int_0^1 \int_0^1 \left( \mu_* (\bar{r}, \bar{\theta}, \bar{z}) \frac{\partial v_{\bar{\theta}}^*}{\partial z_*} (\bar{r}, \bar{\theta}, \bar{z}) \right) \Big|_{\bar{z}=0} \frac{[\bar{r} (R_* - 1) + 1]^2}{h_* (\bar{r}, \bar{\theta})} d\bar{r} d\bar{\theta}.
 \end{aligned} \tag{3.85}$$

### 3.8.5 Friction Coefficient

The friction coefficient is the ratio of friction to normal forces. In particular, for this lubrication problem the friction coefficient is defined as the net tangential force delivered to the separator plate divided by the normal force.

$$\mu_F = -\frac{F_{\theta,0}}{F_z} = -\frac{F_{\theta,0}^*}{F_z^*} \tag{3.86}$$

The negative sign in front of this expression is used because the frictional force is defined positive to the right. Again, since the separator plate is defined to be in the  $z = 0$  plane, pressure effects need not be considered. This would not be the case if the friction force was computed on  $z = h(r, \theta)$ . From the previous discussion, the friction coefficient would be  $\mu_F = \frac{F_{\theta,h} + F_{p,h}}{F_z}$ . Again, since the lubricant is not accelerating, this quantity is equal to the friction coefficient given by Equation (3.86).

## CHAPTER 4

### NUMERICAL SOLUTION METHOD

This chapter describes the mathematical model's numerical implementation used in this dissertation. The first section discusses the staggered grid on which the governing equations are discretized. The second section lists the discrete form of the governing equations and supplemental boundary conditions. Here, the governing equations and boundary conditions are converted to algebraic equations using finite difference discretization. In the third section, the algorithm employed to solve the governing equations is summarized. The fourth section gives the method used to obtain the clutch performance parameters introduced in the previous chapter and discusses an example. The fifth section presents two verification test cases for the numerical solution method.

#### 4.1 Staggered Grid

The numerical solution of the governing equations is obtained on a staggered grid. Here, we employ equispaced nodal grid points at discrete locations in the computational domain. The grid is staggered in the  $\bar{r}$ - $\bar{\theta}$  plane as shown Figure 4.1. The grid is not staggered in the  $\bar{z}$ -direction.

In the computational domain, the discrete location of the dependent variables'

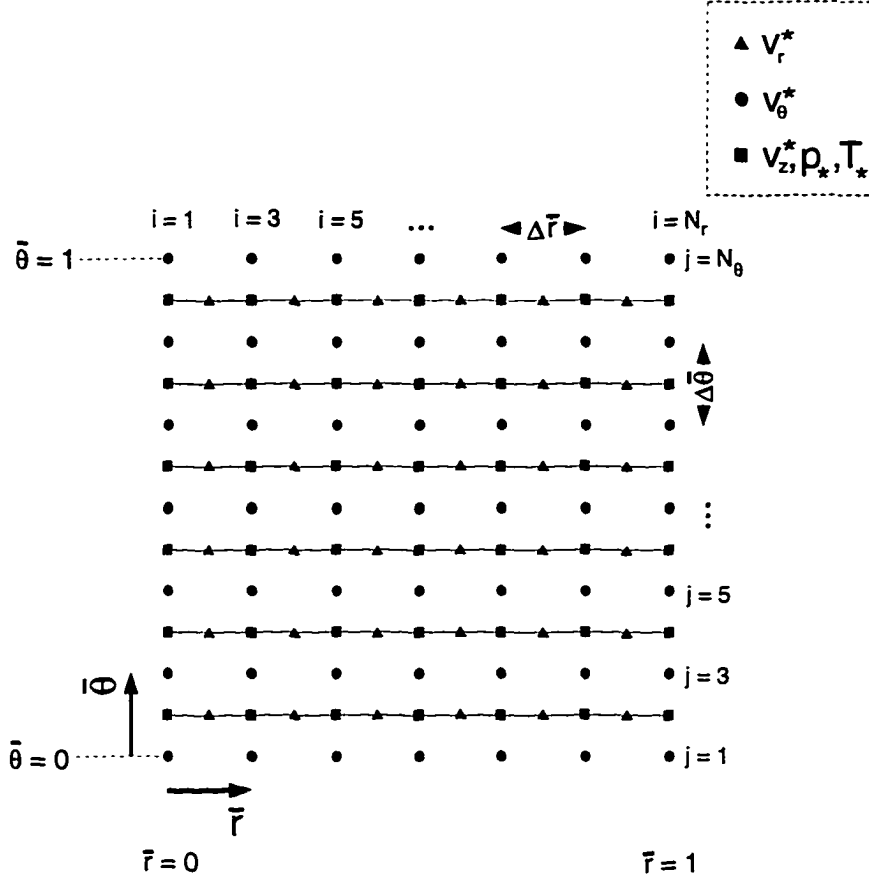


Figure 4.1: Staggered Grid

nodes is illustrated in Figure 4.1 and defined mathematically below:

$$\bar{r}_i = \left(\frac{i-1}{2}\right) \Delta\bar{r}, \quad \bar{\theta}_j = \left(\frac{j-1}{2}\right) \Delta\bar{\theta}, \quad \bar{z}_k = (k-1) \Delta\bar{z}, \quad (4.1)$$

where  $i = 1, 3, 5, \dots, N_r$  for  $v_\theta^*, v_z^*, p_*$ , and  $T_*$ ,

$i = 2, 4, 6, \dots, N_r - 1$  for  $v_r^*$ ,

$j = 1, 3, 5, \dots, N_\theta$  for  $v_\theta^*$ , (4.2)

$j = 2, 4, 6, \dots, N_\theta - 1$  for  $v_r^*, v_z^*, p_*$ , and  $T_*$ ,

$k = 1, 2, 3, \dots, N_z$  for  $v_r^*, v_\theta^*, v_z^*, p_*$ , and  $T_*$ .

Here,  $N_r$ ,  $N_\theta$ , and  $N_z$  are respectively the total number of radial, angular, and axial grid points. It is assumed that  $N_r$ ,  $N_\theta$ , and  $N_z$  are positive, odd integers. In Figure

4.1,  $N_r = N_\theta = 13$ . The computational grid spacings are defined in terms of the number of nodes:

$$\Delta\bar{r} = \frac{2}{N_r - 1}, \quad \Delta\bar{\theta} = \frac{2}{N_\theta - 1}, \quad \Delta\bar{z} = \frac{1}{N_z - 1}. \quad (4.3)$$

This staggered grid is advantageous for several reasons. The prescription of pressure and temperature boundary conditions at the inner and outer radii is straightforward. Further, truncation error and undesirable oscillations, which may occur on non-staggered grids, are avoided in the solution of Poisson pressure equations [46]. Further discussion on the use of staggered grids is given by Fletcher [17].

## 4.2 Discretized Equations

The discrete representation of the governing equations is given in this section. First, the radial momentum equation, angular momentum equation, and no-slip boundary conditions are discretized. Second, an integral form of the continuity equation is combined with the momentum equations in order to obtain a Poisson pressure equation. Third, a differential form of the continuity equation is used to obtain a finite difference relation for the axial velocity. Fourth, the energy equation, along with boundary conditions on the temperature field, are given in discrete form.

In short, the terms in the governing equations are approximated by finite difference expressions which enable a systematic computation of the dependent variables. To solve for the pressure, radial velocity, and angular velocity, a Marker and Cell (MAC) method is employed. This method is characterized by the use of a staggered grid and solving a Poisson pressure equation. To solve for the temperature, a three level fully

implicit (3LFI) routine is used. In this method, the energy equation is treated as parabolic in radius.

#### 4.2.1 Discrete Radial and Angular Momentum

The numerical discretization of Equations (3.65) and (3.66) subjected to the boundary conditions stated in Equation (3.69) are presented in this section. At present, it is assumed that both the discrete solution of the pressure field and the discrete solution of the viscosity are known. A discussion of how the pressure and viscosity are obtained is given shortly.

The momentum equations are written in discrete form using spatial central differencing as follows:

$$\begin{aligned} \frac{h_*^{[ij]2}}{\Delta \bar{r}} \frac{1}{(R_* - 1)} (p_*^{[i+1,j]} - p_*^{[i-1,j]}) &= \frac{\mu_*^{[i,j,k]}}{\Delta \bar{z}^2} (v_r^{*[i,j,k+1]} - 2v_r^{*[i,j,k]} + v_r^{*[i,j,k-1]}) \\ &+ \left( \frac{\mu_*^{[i,j,k+1]} - \mu_*^{[i,j,k-1]}}{2\Delta \bar{z}} \right) \left( \frac{v_r^{*[i,j,k+1]} - v_r^{*[i,j,k-1]}}{2\Delta \bar{z}} \right), \end{aligned} \quad (4.4)$$

and

$$\begin{aligned} \frac{h_*^{[ij]2}}{[\bar{r}^{[i]}(R_* - 1) + 1]\Delta \bar{\theta} \theta_o} (p_*^{[i,j+1]} - p_*^{[i,j-1]}) &= \frac{\mu_*^{[i,j,k]}}{\Delta \bar{z}^2} (v_\theta^{*[i,j,k+1]} - 2v_\theta^{*[i,j,k]} + v_\theta^{*[i,j,k-1]}) \\ &+ \left( \frac{\mu_*^{[i,j,k+1]} - \mu_*^{[i,j,k-1]}}{2\Delta \bar{z}} \right) \left( \frac{v_\theta^{*[i,j,k+1]} - v_\theta^{*[i,j,k-1]}}{2\Delta \bar{z}} \right). \end{aligned} \quad (4.5)$$

The no-slip boundary conditions, Equation (3.69), may be written in discrete form as follows:

$$v_r^{*[i,j,1]} = v_r^{*[i,j,N_z]} = v_\theta^{*[i,j,N_z]} = 0, \quad v_\theta^{*[i,j,1]} = \Omega_* [\bar{r}^{[i]}(R_* - 1) + 1]. \quad (4.6)$$

In Equations (4.4), (4.5), and (4.6), the superscripts in brackets denote the nodal position of the dependent variables with  $i$ ,  $j$ , and  $k$  corresponding to radial, angular, and axial positions, respectively.

and axial grid locations. As indicated by Equation (4.2), Equation (4.4) is defined on  $i = 2, 4, 6, \dots, N_r - 1$ ,  $j = 2, 4, 6, \dots, N_\theta - 1$ , and  $k = 1, 2, 3, \dots, N_z$ . Similarly, Equation (4.5) is defined on  $i = 1, 3, 5, \dots, N_r$ ,  $j = 1, 3, 5, \dots, N_\theta$ , and  $k = 1, 2, 3, \dots, N_z$ . Note that in addition to the five dependent variables,  $v_r^*$ ,  $v_\theta^*$ ,  $v_z^*$ ,  $p_*$ , and  $T_*$ , discrete locations are indicated for the film thickness,  $h_*$ , and the viscosity,  $\mu_*$ .

For given values of  $i$  and  $j$ , Equations (4.4), (4.5), and (4.6) may be written for all values of  $k$ , ( $k = 1, 2, 3, \dots, N_z$ ), in a compact matrix form:

$$[\mathbf{A}^{[i,j]}] \mathbf{v}_r^{[i,j]} = \mathbf{f}_{V_r}^{[i,j]}, \quad [\mathbf{A}^{[i,j]}] \mathbf{v}_\theta^{[i,j]} = \mathbf{f}_{V_\theta}^{[i,j]} + \mathbf{f}_{V_\theta BC}^{[i]}, \quad (4.7)$$

where

$$[\mathbf{A}^{[i,j]}] = \begin{bmatrix} 1 & 0 & 0 & \dots & 0 & 0 & 0 \\ A_1^{[i,j,2]} & A_2^{[i,j,2]} & A_3^{[i,j,2]} & 0 & \dots & 0 & 0 \\ 0 & A_1^{[i,j,3]} & A_2^{[i,j,3]} & A_3^{[i,j,3]} & 0 & \dots & 0 \\ 0 & 0 & \ddots & \ddots & \ddots & & \vdots \\ \vdots & \vdots & & A_1^{[i,j,N_z-2]} & A_2^{[i,j,N_z-2]} & A_3^{[i,j,N_z-2]} & 0 \\ 0 & 0 & \dots & 0 & A_1^{[i,j,N_z-1]} & A_2^{[i,j,N_z-1]} & A_3^{[i,j,N_z-1]} \\ 0 & 0 & \dots & 0 & 0 & 0 & 1 \end{bmatrix}, \quad (4.8)$$

$$\begin{aligned}
\mathbf{v}_r^{[i,j]} &= \begin{bmatrix} v_r^{*[i,j,1]} & v_r^{*[i,j,2]} & v_r^{*[i,j,3]} & \dots & v_r^{*[i,j,N_z-2]} & v_r^{*[i,j,N_z-1]} & v_r^{*[i,j,N_z]} \end{bmatrix}^T, \\
\mathbf{v}_\theta^{[i,j]} &= \begin{bmatrix} v_\theta^{*[i,j,1]} & v_\theta^{*[i,j,2]} & v_\theta^{*[i,j,3]} & \dots & v_\theta^{*[i,j,N_z-2]} & v_\theta^{*[i,j,N_z-1]} & v_\theta^{*[i,j,N_z]} \end{bmatrix}^T, \\
\mathbf{f}_{V_r}^{[i,j]} &= \begin{bmatrix} 0 & 1 & 1 & \dots & 1 & 1 & 0 \end{bmatrix}^T f_{V_r}^{[i,j]}, \\
\mathbf{f}_{V_\theta}^{[i,j]} &= \begin{bmatrix} 0 & 1 & 1 & \dots & 1 & 1 & 0 \end{bmatrix}^T f_{V_\theta}^{[i,j]}, \\
\mathbf{f}_{V_\theta BC}^{[i]} &= \begin{bmatrix} \Omega_* [\bar{r}^{[i]} (R_* - 1) + 1] & 0 & 0 & \dots & 0 & 0 & 0 \end{bmatrix}^T,
\end{aligned} \tag{4.9}$$

and

$$\begin{aligned}
f_{V_r}^{[i,j]} &= \frac{h_*^{[ij]2} \Delta \bar{z}^2}{\Delta \bar{r}} \frac{1}{(R_* - 1)} (p_*^{[i+1,j]} - p_*^{[i-1,j]}), \\
f_{V_\theta}^{[i,j]} &= \frac{h_*^{[ij]2} \Delta \bar{z}^2}{[\bar{r}^{[i]} (R_* - 1) + 1] \Delta \bar{\theta} \theta_o} \frac{1}{\theta_o} (p_*^{[i,j+1]} - p_*^{[i,j-1]}), \\
A_1^{[i,j,k]} &= \mu_*^{[i,j,k]} - \frac{1}{4} (\mu_*^{[i,j,k+1]} - \mu_*^{[i,j,k-1]}), \quad A_2^{[i,j,k]} = -2\mu_*^{[i,j,k]}, \\
A_3^{[i,j,k]} &= \mu_*^{[i,j,k]} + \frac{1}{4} (\mu_*^{[i,j,k+1]} - \mu_*^{[i,j,k-1]}).
\end{aligned} \tag{4.10}$$

It is seen that  $[\mathbf{A}^{[i,j]}]$  is tridiagonal.

#### 4.2.2 Discrete Poisson Pressure Equation

This section discusses the derivation of a discrete Poisson pressure equation. This equation is derived using Equations (3.64), (3.69), (4.7), and (4.10). The following derivation parallels classical derivations of the Reynolds equation discussed by Hamrock [22] and Gross [18]. Allowing for variable viscosity across the film complicates the derivation. However, for current purposes, a known viscosity distribution is assumed.

First the continuity equation, (3.64), is integrated from  $\bar{z} = 0$  to  $\bar{z} = 1$ . Using integration by parts, Leibnitz's integration rule, and the no-slip boundary conditions listed in Equation (3.69), the following integral form of the continuity equation was



derived:

$$\frac{1}{(R_* - 1)} \frac{\partial}{\partial \bar{r}} (h_* [\bar{r} (R_* - 1) + 1] \tilde{v}_r^*) + \frac{1}{\theta_o} \frac{\partial}{\partial \theta} (h_* \tilde{v}_\theta^*) = 0, \quad (4.11)$$

where

$$\tilde{v}_r^* = \int_0^1 v_r^* d\bar{z} \quad \text{and} \quad \tilde{v}_\theta^* = \int_0^1 v_\theta^* d\bar{z}. \quad (4.12)$$

Recalling that we required  $N_z$  to be a positive odd integer, it is possible to approximate the integrals of Equation (4.12) numerically using Simpson's rule. For  $\tilde{v}_r^*$ , we have

$$\tilde{v}_r^* [i,j] \approx \frac{\Delta \bar{z}}{3} \left( v_\theta^* [i,j,1] + v_\theta^* [i,j,N_z] + 4 \sum_{k=2,4,\dots}^{N_z-1} v_r^* [i,j,k] + 2 \sum_{k=3,5,\dots}^{N_z-2} v_r^* [i,j,k] \right).$$

More generally, numerical integration techniques are simply weighted sums of the discrete values of the integrand. Returning to the notation of Equation (4.7), a more general approximation of  $\tilde{v}_r^*$  is as follows:

$$\tilde{v}_r^* [i,j] \approx \sum_{k=1}^{N_z} \mathbf{w}^{[i,j]} \cdot \mathbf{v}_r^{[i,j]}, \quad (4.13)$$

where  $\mathbf{w}^{[i,j]}$  is a known vector with components equal to the weights in the integration method. In the case of Simpson's rule,

$$\mathbf{w}^{[i,j]} = \frac{\Delta \bar{z}}{3} \left[ 1 \ 4 \ 2 \ 4 \ 2 \ \dots \ 2 \ 4 \ 2 \ 4 \ 1 \right]^T.$$

Substituting Equations (4.7) into (4.13) we have

$$\tilde{v}_r^* [i,j] \approx \sum_{k=1}^{N_z} \mathbf{w}^{[i,j]} \cdot [\mathbf{A}^{[i,j]}]^{-1} \mathbf{f}_{V_r}^{[i,j]} = f_{V_r}^{[i,j]} \sum_{k=1}^{N_z} \mathbf{w}^{[i,j]} \cdot [\mathbf{A}^{[i,j]}]^{-1} \mathbf{1}_1^{[i,j]}, \quad (4.14)$$

where

$$\mathbf{1}_1^{[i,j]} = \left[ 0 \ 1 \ 1 \ \dots \ 1 \ 1 \ 0 \right]^T.$$

Rearranging Equation (4.14), and recalling Equation (4.10), the following expression for  $\tilde{v}_r^*$  is found:

$$\tilde{v}_r^* [i,j] \approx I_r^{[i,j]} \left( p_*^{[i+1,j]} - p_*^{[i-1,j]} \right),$$

$$\text{where } I_r^{[i,j]} = \frac{h_*^{[i,j]2} \Delta \bar{z}^2}{\Delta \bar{r}} \frac{1}{(R_* - 1)} \sum_{k=1}^{N_z} \mathbf{w}^{[i,j]} \cdot [\mathbf{A}^{[i,j]}]^{-1} \mathbf{l}_1^{[i,j]}.$$
 (4.15)

Similarly,

$$\tilde{v}_\theta^* [i,j] \approx I_\theta^{[i,j]} \left( p_*^{[i,j+1]} - p_*^{[i,j-1]} \right) + I_{\theta BC}^{[i,j]},$$

$$\text{where } I_\theta^{[i,j]} = \frac{h_*^{[i,j]2} \Delta \bar{z}^2}{[\bar{r}^{[i]} (R_* - 1) + 1] \Delta \theta} \frac{1}{\theta_o} \sum_{k=1}^{N_z} \mathbf{w}^{[i,j]} \cdot [\mathbf{A}^{[i,j]}]^{-1} \mathbf{l}_1^{[i,j]},$$
 (4.16)
$$\text{and } I_{\theta BC}^{[i,j]} = \Omega_* [\bar{r}^{[i]} (R_* - 1) + 1] \sum_{k=1}^{N_z} \mathbf{w}^{[i,j]} \cdot [\mathbf{A}^{[i,j]}]^{-1} \mathbf{l}_2^{[i,j]}.$$

Unlike, the radial counterpart,  $\tilde{v}_\theta^*$  contains a term due to the non-homogeneous no-slip boundary condition. In Equation (4.16),

$$\mathbf{l}_2^{[i,j]} = \left[ 1 \ 0 \ 0 \ \dots \ 0 \ 0 \ 0 \right]^T.$$

Discretizing Equation (4.11) on the pressure nodes shown in Figure 4.1, we have

$$\frac{1}{(R_* - 1)} \frac{1}{\Delta \bar{r}} \left( h_*^{[i+1,j]} [\bar{r}^{[i+1]} (R_* - 1) + 1] \tilde{v}_r^* [i+1,j] \right.$$

$$\left. - h_*^{[i-1,j]} [\bar{r}^{[i-1]} (R_* - 1) + 1] \tilde{v}_r^* [i-1,j] \right)$$
 (4.17)
$$+ \frac{1}{\theta_o} \frac{1}{\Delta \theta} \left( h_*^{[i,j+1]} \tilde{v}_\theta^* [i,j+1] - h_*^{[i,j-1]} \tilde{v}_\theta^* [i,j-1] \right) = 0.$$

Substituting the finite difference expressions derived for  $\tilde{v}_r^* [i,j]$  and  $\tilde{v}_\theta^* [i,j]$ , defined as approximations in Equations (4.15) and (4.16), a discrete Poisson pressure equation is obtained:

$$a_p^{[i,j]} p_*^{[i,j]} + b_p^{[i,j]} p_*^{[i+2,j]} + c_p^{[i,j]} p_*^{[i-2,j]} + d_p^{[i,j]} p_*^{[i,j+2]} + e_p^{[i,j]} p_*^{[i,j-2]} = f_p^{[i,j]},$$
 (4.18)

$$\begin{aligned}
\text{where } a_p^{[i,j]} &= -\frac{1}{(R_* - 1)} \frac{1}{\Delta \bar{r}} \left( I_r^{[i+1,j]} h_*^{[i+1,j]} [\bar{r}^{[i+1]} (R_* - 1) + 1] \right. \\
&\quad \left. + I_r^{[i-1,j]} h_*^{[i-1,j]} [\bar{r}^{[i-1]} (R_* - 1) + 1] \right) \\
&\quad - \frac{1}{\theta_o} \frac{1}{\Delta \theta} \left( I_\theta^{[i,j+1]} h_*^{[i,j+1]} + I_\theta^{[i,j-1]} h_*^{[i,j-1]} \right), \\
b_p^{[i,j]} &= \frac{1}{(R_* - 1)} \frac{1}{\Delta \bar{r}} I_r^{[i+1,j]} h_*^{[i+1,j]} [\bar{r}^{[i+1]} (R_* - 1) + 1], \\
c_p^{[i,j]} &= \frac{1}{(R_* - 1)} \frac{1}{\Delta \bar{r}} I_r^{[i-1,j]} h_*^{[i-1,j]} [\bar{r}^{[i-1]} (R_* - 1) + 1], \\
d_p^{[i,j]} &= \frac{1}{\theta_o} \frac{1}{\Delta \theta} I_\theta^{[i,j+1]} h_*^{[i,j+1]}, \\
e_p^{[i,j]} &= \frac{1}{\theta_o} \frac{1}{\Delta \theta} I_\theta^{[i,j-1]} h_*^{[i,j-1]}, \\
f_p^{[i,j]} &= \frac{1}{\theta_o} \frac{1}{\Delta \theta} \left( I_\theta^{[i,j-1]} h_*^{[i,j-1]} - I_\theta^{[i,j+1]} h_*^{[i,j+1]} \right).
\end{aligned}$$

Equation (4.18), referred to as the discrete Poisson pressure equation, is defined on odd  $i$ -nodes and even  $j$ -nodes as indicated in Figure 4.1. Note that the boundary values of pressure must be supplied to close the numerical problem. From Equations (3.70) and (4.2), we have

$$p_*^{[1,j]} = 0 \quad \text{and} \quad p_*^{[N_r,j]} = p_o^* \quad (4.19)$$

on the radial boundaries. On the angular boundaries, Equation (4.18) suggests that we must have knowledge of  $p_*^{[i,0]}$  and  $p_*^{[i,N_t+1]}$ . Using second order finite differencing and averaging for Equation (3.70), it can be shown that

$$p_*^{[i,0]} = p_*^{[i,N_t-1]} \quad \text{and} \quad p_*^{[i,N_t+1]} = p_*^{[i,2]}. \quad (4.20)$$

Equations (4.18), (4.19), and (4.20) can be written in terms of a general block-banded matrix. Note that, knowledge of the velocity field is not required to obtain the pressure. Rather, the boundary conditions at the clutch plates are required. Further.

the viscosity distribution is assumed to be known.

Again, the above method, which outlines a methodology by which a pressure distribution may be found, parallels classical derivations of the Reynolds equation. The additional complication of allowing for variable viscosity across the film demands numerical treatment in all but the simplest of cases. The analogous steps used to derive a variable viscosity Reynolds equation are given in Appendix B. Terms in this variable viscosity Reynolds equation are integrals of the form:  $\int_0^1 \frac{z dz}{\mu^*}$  and  $\int_0^1 \frac{dz}{\mu^*}$ . These integrals would have to be evaluated numerically. Further, the discretization of such a Reynolds equation would demand numerical treatment to solve for the pressure. Thus, the procedure to follow in solving the variable viscosity Reynolds equation must use the methodology given above. In other words, both accounting for variable viscosity and solving a Poisson pressure equation would demand numerical treatment in either case. The methodology outlined in this section is advantageous because continuity will clearly be satisfied on a discrete level.

#### **4.2.3 Discrete Axial Velocity Equation**

This section discusses the discretization of the differential form of Equation (3.64) which is used to obtain the axial velocity. It is assumed that the radial and angular components of velocity are known.

First, Equation (3.64) is differentiated with respect to the variable  $\bar{z}$ :

$$\begin{aligned} & \frac{1}{(R_* - 1)} \left[ h_* \frac{\partial}{\partial \bar{r}} \left( [\bar{r}(R_* - 1) + 1] \frac{\partial v_r^*}{\partial \bar{z}} \right) \right. \\ & \quad \left. - [\bar{r}(R_* - 1) + 1] \frac{\partial h_*}{\partial \bar{r}} \left( \frac{\partial v_r^*}{\partial \bar{z}} + \bar{z} \frac{\partial^2 v_r^*}{\partial \bar{z}^2} \right) \right] \\ & \quad + \frac{1}{\theta_o} \left[ h_* \frac{\partial^2 v_\theta^*}{\partial \bar{z} \partial \theta} - \frac{\partial h_*}{\partial \theta} \left( \frac{\partial v_\theta^*}{\partial \bar{z}} + \bar{z} \frac{\partial^2 v_\theta^*}{\partial \bar{z}^2} \right) \right] + [\bar{r}(R_* - 1) + 1] \frac{\partial^2 v_z^*}{\partial \bar{z}^2} = 0, \end{aligned} \quad (4.21)$$

which can be rearranged as follows:

$$[\bar{r}(R_* - 1) + 1] \frac{\partial^2 v_z^*}{\partial \bar{z}^2} = -f_{V_z}, \quad (4.22)$$

where

$$\begin{aligned} f_{V_z} = & \frac{1}{(R_* - 1)} \left[ h_* \frac{\partial}{\partial \bar{r}} \left( [\bar{r}(R_* - 1) + 1] \frac{\partial v_r^*}{\partial \bar{z}} \right) \right. \\ & \quad \left. - [\bar{r}(R_* - 1) + 1] \frac{\partial h_*}{\partial \bar{r}} \left( \frac{\partial v_r^*}{\partial \bar{z}} + \bar{z} \frac{\partial^2 v_r^*}{\partial \bar{z}^2} \right) \right] \\ & \quad + \frac{1}{\theta_o} \left[ h_* \frac{\partial^2 v_\theta^*}{\partial \bar{z} \partial \theta} - \frac{\partial h_*}{\partial \theta} \left( \frac{\partial v_\theta^*}{\partial \bar{z}} + \bar{z} \frac{\partial^2 v_\theta^*}{\partial \bar{z}^2} \right) \right]. \end{aligned}$$

Second, Equation (4.22) is discretized on odd  $i$ -nodes and even  $j$ -nodes:

$$\frac{[\bar{r}^{[i]}(R_* - 1) + 1]}{\Delta \bar{z}^2} \left( v_z^{*[i,j,k+1]} - 2v_z^{*[i,j,k]} + v_z^{*[i,j,k-1]} \right) = -f_{V_z}^{[i,j,k]}, \quad (4.23)$$

where

$$\begin{aligned} f_{V_z}^{[i,j,k]} = & a_{1V_z}^{[i,j,k]} v_r^{*[i+1,j,k+1]} + a_{2V_z}^{[i,j,k]} v_r^{*[i+1,j,k-1]} + a_{3V_z}^{[i,j,k]} v_r^{*[i-1,j,k-1]} \\ & + a_{4V_z}^{[i,j,k]} v_r^{*[i-1,j,k+1]} + a_{5V_z}^{[i,j,k]} \left( v_r^{*[i+1,j,k]} + v_r^{*[i-1,j,k]} \right) \\ & + a_{6V_z}^{[i,j,k]} v_\theta^{*[i,j+1,k+1]} + a_{7V_z}^{[i,j,k]} v_\theta^{*[i,j+1,k-1]} + a_{8V_z}^{[i,j,k]} v_\theta^{*[i,j-1,k-1]} \\ & + a_{9V_z}^{[i,j,k]} v_\theta^{*[i,j-1,k+1]} + a_{10V_z}^{[i,j,k]} \left( v_\theta^{*[i,j+1,k]} + v_\theta^{*[i,j-1,k]} \right), \end{aligned}$$

$$\begin{aligned}
a_{1V_z}^{[i,j,k]} &= \frac{1}{2\Delta\bar{r}\Delta\bar{z}} \frac{1}{(R_* - 1)} \left[ h_*^{[i,j]} [\bar{r}^{[i+1]} (R_* - 1) + 1] \right. \\
&\quad \left. - [\bar{r}^{[i]} (R_* - 1) + 1] \left( h_*^{[i+1,j]} - h_*^{[i-1,j]} \right) \left( 1 + \frac{\bar{z}^{[k]}}{\Delta\bar{z}} \right) \right], \\
a_{2V_z}^{[i,j,k]} &= \frac{1}{2\Delta\bar{r}\Delta\bar{z}} \frac{1}{(R_* - 1)} \left[ -h_*^{[i,j]} [\bar{r}^{[i+1]} (R_* - 1) + 1] \right. \\
&\quad \left. + [\bar{r}^{[i]} (R_* - 1) + 1] \left( h_*^{[i+1,j]} - h_*^{[i-1,j]} \right) \left( 1 - \frac{\bar{z}^{[k]}}{\Delta\bar{z}} \right) \right], \\
a_{3V_z}^{[i,j,k]} &= \frac{1}{2\Delta\bar{r}\Delta\bar{z}} \frac{1}{(R_* - 1)} \left[ h_*^{[i,j]} [\bar{r}^{[i-1]} (R_* - 1) + 1] \right. \\
&\quad \left. + [\bar{r}^{[i]} (R_* - 1) + 1] \left( h_*^{[i+1,j]} - h_*^{[i-1,j]} \right) \left( 1 - \frac{\bar{z}^{[k]}}{\Delta\bar{z}} \right) \right], \\
a_{4V_z}^{[i,j,k]} &= \frac{1}{2\Delta\bar{r}\Delta\bar{z}} \frac{1}{(R_* - 1)} \left[ -h_*^{[i,j]} [\bar{r}^{[i-1]} (R_* - 1) + 1] \right. \\
&\quad \left. - [\bar{r}^{[i]} (R_* - 1) + 1] \left( h_*^{[i+1,j]} - h_*^{[i-1,j]} \right) \left( 1 + \frac{\bar{z}^{[k]}}{\Delta\bar{z}} \right) \right], \\
a_{5V_z}^{[i,j,k]} &= \frac{\bar{z}^{[k]}}{\Delta\bar{r}\Delta\bar{z}^2} \frac{1}{(R_* - 1)}, \\
a_{6V_z}^{[i,j,k]} &= \frac{1}{2\Delta\bar{\theta}\Delta\bar{z}} \frac{1}{\theta_o} \left[ h_*^{[i,j]} - \left( h_*^{[i,j+1]} - h_*^{[i,j-1]} \right) \left( 1 + \frac{\bar{z}^{[k]}}{\Delta\bar{z}} \right) \right], \\
a_{7V_z}^{[i,j,k]} &= \frac{1}{2\Delta\bar{\theta}\Delta\bar{z}} \frac{1}{\theta_o} \left[ -h_*^{[i,j]} + \left( h_*^{[i,j+1]} - h_*^{[i,j-1]} \right) \left( 1 - \frac{\bar{z}^{[k]}}{\Delta\bar{z}} \right) \right], \\
a_{8V_z}^{[i,j,k]} &= \frac{1}{2\Delta\bar{\theta}\Delta\bar{z}} \frac{1}{\theta_o} \left[ h_*^{[i,j]} + \left( h_*^{[i,j+1]} - h_*^{[i,j-1]} \right) \left( 1 - \frac{\bar{z}^{[k]}}{\Delta\bar{z}} \right) \right], \\
a_{9V_z}^{[i,j,k]} &= \frac{1}{2\Delta\bar{\theta}\Delta\bar{z}} \frac{1}{\theta_o} \left[ -h_*^{[i,j]} - \left( h_*^{[i,j+1]} - h_*^{[i,j-1]} \right) \left( 1 + \frac{\bar{z}^{[k]}}{\Delta\bar{z}} \right) \right], \\
a_{10V_z}^{[i,j,k]} &= \frac{\bar{z}^{[k]}}{\Delta\bar{\theta}\Delta\bar{z}^2} \frac{1}{\theta_o}.
\end{aligned}$$

As can be seen from Equation (4.23) and Figure 4.1, the angular boundaries do not present a problem. However, at  $i = 1$  and  $i = N_r$  information outside the domain is required. For example, at  $i = 1$ ,  $v_r^{*[0,j,k+1]}$ ,  $v_r^{*[0,j,k]}$ , and  $v_r^{*[0,j,k-1]}$  need to be specified. To circumvent this problem, truncated Taylor series expansions are written to approximate values outside the domain. For example,  $v_r^{*[0,j,k]} \approx 3v_r^{*[2,j,k]} - 3v_r^{*[4,j,k]} + v_r^{*[6,j,k]}$ . Only second order truncation error is introduced using these expressions. This

analysis differs from the specification of boundary conditions in that ultimately only values inside the domain are required.

Since Equation (4.22) is a second order differential equation in  $\bar{z}$ , both no-slip boundary conditions listed in Equation (3.69) for  $v_z^*$  are utilized. Here we have

$$v_z^{*[i,j,1]} = v_z^{*[i,j,N_z]} = 0. \quad (4.24)$$

Equations (4.23) and (4.24) may be written using a tridiagonal matrix in the same form as Equation (4.7).

It is not hard to show that if the integral and differential forms of continuity are satisfied, then Equation (3.64) is satisfied. A simplified proof is given here. Here,  $\int_0^h \nabla \cdot \mathbf{v} dz = 0$  is considered the integral form of continuity, and  $\frac{\partial}{\partial z} (\nabla \cdot \mathbf{v}) = 0$  is considered the differential form of continuity. Let  $\nabla \cdot \mathbf{v} = f_c$ . Given that  $\frac{\partial}{\partial z} (\nabla \cdot \mathbf{v}) = \frac{\partial f_c}{\partial z} = 0$ , it is known that  $f_c$  can be a function of  $r$  and  $\theta$  at most. Therefore,  $\int_0^h f_c dz = f_c \int_0^h dz = f_c h$ . But since  $h \neq 0$ , and it is given that the integral form of continuity is zero, we must have  $f_c = 0$ . Therefore continuity is satisfied. This is particularly relevant because the previous section which derived the Poisson pressure equation used the integral form of continuity and this section employed the differential form of continuity.

#### 4.2.4 Discrete Energy Equation

This section discusses the discretization of Equations (3.68), (3.71), and (3.72). It is assumed that the velocity components and viscosity are known.

First, Equation (3.68) is written in the form

$$\lambda_{\bar{r}} \frac{\partial T_*}{\partial \bar{r}} + \lambda_{\bar{\theta}} \frac{\partial T_*}{\partial \bar{\theta}} + \lambda_{\bar{z}} \frac{\partial T_*}{\partial \bar{z}} - \frac{\partial^2 T_*}{\partial \bar{z}^2} = f_{VD}, \quad (4.25)$$

where the coefficients of the energy equation, (4.25), are defined as follows:

$$\begin{aligned} \lambda_{\bar{r}} &= \frac{Gr h_*^2 v_r^*}{(R_* - 1)}, & \lambda_{\bar{\theta}} &= \frac{Gr h_*^2 v_{\theta}^*}{[\bar{r}(R_* - 1) + 1]\theta_o}, \\ \lambda_{\bar{z}} &= Gr h_* \left[ v_z^* - \frac{\partial h_*}{\partial \bar{r}} \frac{v_r^* \bar{z}}{(R_* - 1)} - \frac{\partial h_*}{\partial \bar{\theta}} \frac{v_{\theta}^* \bar{z}}{[\bar{r}(R_* - 1) + 1]\theta_o} \right], \\ f_{VD} &= \mu_* Br \left[ \left( \frac{\partial v_r^*}{\partial \bar{z}} \right)^2 + \left( \frac{\partial v_{\theta}^*}{\partial \bar{z}} \right)^2 \right]. \end{aligned} \quad (4.26)$$

Second, using Equation (4.2) the terms in Equation (4.26) are discretized:

$$\begin{aligned} \lambda_{\bar{r}}^{[i,j,k]} &= \frac{Gr h_*^{[i,j]2} v_r^{*[i,j,k]}}{(R_* - 1)}, & \lambda_{\bar{\theta}}^{[i,j,k]} &= \frac{Gr h_*^{[i,j]2} v_{\theta}^{*[i,j,k]}}{[\bar{r}^{[i]}(R_* - 1) + 1]\theta_o}, \\ \lambda_{\bar{z}} &= Gr h_*^{[i,j]} \left[ \frac{(v_z^{*[i+1,j,k]} + v_z^{*[i-1,j,k]})}{2} - \frac{v_r^{*[i,j,k]} \bar{z}^{[k]} (h_*^{[i+1,j]} - h_*^{[i-1,j]})}{\Delta \bar{r} (R_* - 1)} \right. \\ &\quad \left. - \frac{(v_{\theta}^{*[i+1,j+1,k]} + v_{\theta}^{*[i-1,j+1,k]} + v_{\theta}^{*[i+1,j-1,k]} + v_{\theta}^{*[i-1,j-1,k]}) \bar{z}^{[k]} (h_*^{[i,j+1]} - h_*^{[i,j-1]})}{4\Delta \bar{\theta} [\bar{r}^{[i]}(R_* - 1) + 1]\theta_o} \right], \\ f_{VD}^{[i,j,k]} &= \frac{\mu_*^{[i,j,k]} Br}{4\Delta \bar{z}^2} \left[ (v_r^{*[i,j,k+1]} - v_r^{*[i,j,k-1]})^2 \right. \\ &\quad + \frac{1}{16} (v_{\theta}^{*[i+1,j+1,k+1]} + v_{\theta}^{*[i-1,j+1,k+1]} + v_{\theta}^{*[i+1,j-1,k+1]} + v_{\theta}^{*[i-1,j-1,k+1]} \\ &\quad \left. - v_{\theta}^{*[i+1,j+1,k-1]} - v_{\theta}^{*[i-1,j+1,k-1]} - v_{\theta}^{*[i+1,j-1,k-1]} - v_{\theta}^{*[i-1,j-1,k-1]})^2 \right]. \end{aligned} \quad (4.27)$$

Note that  $\lambda_{\bar{r}}$ ,  $\lambda_{\bar{z}}$ , and  $f_{VD}$  are defined on even  $i$ -nodes and even  $j$ -nodes, while  $\lambda_{\bar{\theta}}$  is defined on odd  $i$ -nodes and odd  $j$ -nodes.

Third, the finite difference equation, which approximates Equation (4.25), was obtained by applying a three-level fully implicit (3LFI) [16] scheme. Here, the equation was treated as parabolic in  $\bar{r}$ . Diffusive and convective terms in the  $\bar{z}$ -direction were handled implicitly using second order central differencing, while the convective term



in the  $\bar{\theta}$ -direction was treated explicitly using a three point upwinding technique. The discrete form of the energy equation was taken as follows:

$$\begin{aligned}
& a_{1T}^{[i,j,k]} T_*^{[i,j,k]} + a_{2T}^{[i,j,k]} T_*^{[i,j-2,k]} + a_{3T}^{[i,j,k]} T_*^{[i,j-4,k]} + a_{4T}^{[i,j,k]} T_*^{[i,j,k+1]} \\
& + a_{5T}^{[i,j,k]} T_*^{[i,j,k-1]} = f_T^{[i,j,k]},
\end{aligned} \tag{4.28}$$

where

$$\begin{aligned}
a_{1T}^{[i,j,k]} &= \frac{3\lambda_{\bar{r}}^{[i-1,j,k]}}{2\Delta\bar{r}} + \frac{2}{\Delta\bar{z}^2} + \frac{3}{4\Delta\bar{\theta}} \left( \lambda_{\bar{\theta}}^{[i,j+1,k]} + \lambda_{\bar{\theta}}^{[i,j-1,k]} \right), \\
a_{2T}^{[i,j,k]} &= -\frac{1}{\Delta\bar{\theta}} \left( \lambda_{\bar{\theta}}^{[i,j+1,k]} + \lambda_{\bar{\theta}}^{[i,j-1,k]} \right), \\
a_{3T}^{[i,j,k]} &= \frac{1}{4\Delta\bar{\theta}} \left( \lambda_{\bar{\theta}}^{[i,j+1,k]} + \lambda_{\bar{\theta}}^{[i,j-1,k]} \right), \\
a_{4T}^{[i,j,k]} &= \frac{3\lambda_{\bar{z}}^{[i-1,j,k]}}{4\Delta\bar{z}} - \frac{1}{\Delta\bar{z}^2} - \frac{\lambda_{\bar{z}}^{[i-3,j,k]}}{4\Delta\bar{z}}, \\
a_{5T}^{[i,j,k]} &= -\frac{3\lambda_{\bar{z}}^{[i-1,j,k]}}{4\Delta\bar{z}} - \frac{1}{\Delta\bar{z}^2} + \frac{\lambda_{\bar{z}}^{[i-3,j,k]}}{4\Delta\bar{z}}, \\
f_T^{[i,j,k]} &= \frac{3}{2} f_{VD}^{[i-1,j,k]} - \frac{1}{2} f_{VD}^{[i-3,j,k]} + T_*^{[i-2,j,k]} \left( \frac{3\lambda_{\bar{r}}^{[i-1,j,k]}}{2\Delta\bar{r}} + \frac{\lambda_{\bar{r}}^{[i-3,j,k]}}{2\Delta\bar{r}} \right) \\
& \quad - T_*^{[i-4,j,k]} \frac{\lambda_{\bar{r}}^{[i-3,j,k]}}{2\Delta\bar{r}},
\end{aligned}$$

when  $i = 5, 7, \dots, N_r$ , while for  $i = 3$ ,

where

$$\begin{aligned}
a_{1T}^{[i,j,k]} &= \frac{\lambda_{\bar{r}}^{[2,j,k]}}{2\Delta\bar{r}} + \frac{\lambda_{\bar{r}}^{[4,j,k]}}{2\Delta\bar{r}} + \frac{2}{\Delta\bar{z}^2} + \frac{3}{4\Delta\bar{\theta}} \left( \lambda_{\bar{\theta}}^{[i,j+1,k]} + \lambda_{\bar{\theta}}^{[i,j-1,k]} \right), \\
a_{2T}^{[i,j,k]} &= -\frac{1}{\Delta\bar{\theta}} \left( \lambda_{\bar{\theta}}^{[i,j+1,k]} + \lambda_{\bar{\theta}}^{[i,j-1,k]} \right), \\
a_{3T}^{[i,j,k]} &= \frac{1}{4\Delta\bar{\theta}} \left( \lambda_{\bar{\theta}}^{[i,j+1,k]} + \lambda_{\bar{\theta}}^{[i,j-1,k]} \right), \\
a_{4T}^{[i,j,k]} &= \frac{1}{4\Delta\bar{z}} \left( \lambda_{\bar{z}}^{[2,j,k]} + \lambda_{\bar{z}}^{[4,j,k]} \right) - \frac{1}{\Delta\bar{z}^2}, \\
a_{5T}^{[i,j,k]} &= \frac{1}{4\Delta\bar{z}} - \left( \lambda_{\bar{z}}^{[2,j,k]} + \lambda_{\bar{z}}^{[4,j,k]} \right) - \frac{1}{\Delta\bar{z}^2}, \\
f_T^{[i,j,k]} &= \frac{1}{2} \left( f_{VD}^{[2,j,k]} + f_{VD}^{[4,j,k]} \right) + T_*^{[1,j,k]} \frac{1}{2\Delta\bar{r}} \left( \lambda_{\bar{r}}^{[2,j,k]} + \lambda_{\bar{r}}^{[4,j,k]} \right).
\end{aligned}$$

Two sets of coefficients were required because Equation (4.28) requires two previous levels,  $i - 2$  and  $i - 4$ , to determine the current level  $i$ . In other words, the solution to

the energy equation was obtained by marching forward in radius. This is considered a three level, fully implicit (3LFI) scheme.

Note that at  $i = 1$ , the radial boundary condition in Equation (3.71) may be written discretely as follows:

$$T_*^{[1,j,\kappa]} = 1. \quad (4.29)$$

Further, for  $j = 2$  and  $j = 4$ , Equation (4.28) suggests we must have knowledge of the temperature at  $j = -2$  and  $j = 0$ . However, as periodicity suggests, we have

$$T_*^{[i,-2,\kappa]} = T_*^{[i,N_t-3,\kappa]}, \quad T_*^{[i,0,\kappa]} = T_*^{[i,N_t-1,\kappa]}. \quad (4.30)$$

In other words, two conditions are given because an upwinding technique is employed for the angular coordinate. Finally, Equation (3.72) is discretized using spatial second order differencing:

$$T_*^{[i,j,0]} = T_*^{[i,j,2]}, \quad T_*^{[i,j,N_t+1]} = T_*^{[i,j,N_t-1]}. \quad (4.31)$$

For each  $i$ -level, or discrete radial position, Equations (4.28), (4.29), (4.30), and (4.31) may be combined and written in terms of a block-banded matrix. As mentioned above, an upwinding technique was used for the term  $\frac{\partial T_*}{\partial \theta}$ . This term was handled implicitly as indicated by the finite difference structure of Equation (4.28). It was found that this considerably reduced numerical oscillations in the  $\bar{\theta}$ -direction compared with explicit second order central differencing.

### 4.3 Algorithm Summary

In the previous section, it has been indicated that each numerical problem may

be written in the following general form:

$$[\mathcal{A}]\mathbf{x} = \mathbf{y}. \quad (4.32)$$

In general,  $\mathcal{A}$  is a block-banded matrix,  $\mathbf{x}$  is an unknown vector corresponding to one of the unknown dependent variables:  $v_r^*$ ,  $v_\theta^*$ ,  $v_z^*$ ,  $p_*$ , or  $T_*$ , and  $\mathbf{y}$  is a known forcing function corresponding to the right hand sides of Equations (4.7), (4.18), (4.22), or (4.28). Further, it has been assumed that the viscosity distribution is known. However, we require the viscosity-temperature relation (3.53) to be satisfied. The algorithm used to solve the discrete form of the governing equations which are coupled by Equation (3.53) is discussed in this section.

It is noted here that several methods exist to solve the system of linear algebraic equations indicated by Equation (4.32). A numerical scheme which solves a system of linear algebraic equations having a real banded coefficient matrix was chosen. The scheme computed a lower-upper (LU) factorization [16] of the coefficient matrix in order to check for a singular matrix and to expedite the solution.

The first step in the algorithm was to assume a temperature distribution. The viscosity may be found on all nodal locations using Equation (3.53) and second order averaging. For example, to find the viscosity on even  $i$ -nodes and even  $j$ -nodes, the viscosity is computed at adjacent radial grid locations using Equation (3.53) and second order averaging,  $\mu_*^{[i,j,k]} = \frac{1}{2} \left( \mu_*^{[i+1,j,k]} + \mu_*^{[i-1,j,k]} \right)$ .

Second, with the estimated viscosity distribution a pressure distribution is obtained by solving the discrete pressure equation, introduced in section 4.3.2, written in the form of Equation (4.32). Third, the radial and angular components of velocity

are solved using the equations introduced in section 4.3.1. Recall that in this section the pressure and viscosity were treated as known quantities. Fourth, the axial velocity is obtained using the equations discussed in section 4.3.3. In this section, the radial and angular velocity components were treated as known quantities. Fifth, the temperature is obtained using the equations introduced in section 4.3.4.

A better approximation of the viscosity may be obtained using Equation (3.53). This iterative procedure is continued until the difference in the temperature fields falls below a specified error tolerance. In particular, the maximum temperature difference was required to be less than a specified tolerance.

#### 4.4 Treatment of Clutch Performance Parameters

Upon solving the discretized fluid mechanics problem discussed in the previous section, the performance parameters are found using numerical integration. Numerical quadrature is employed.

For example, the application of Simpson's rule on the radial volumetric flow rate will be discussed here. For convenience, this flow rate is redefined here:

$$Q_r^* = N_g \theta_o [\bar{r} (R_* - 1) + 1] \int_0^1 h_* (\bar{r}, \bar{\theta}) \int_0^1 v_r^* (\bar{r}, \bar{\theta}, \bar{z}) d\bar{z} d\bar{\theta}.$$

The inner integral can be approximated as follows:

$$\int_0^1 v_r^* d\bar{z} \approx I_Q^{[i,j]} = \frac{\Delta \bar{z}}{3} \left( v_r^{*[i,j,1]} + v_r^{*[i,j,N_z]} + 4 \sum_{k=2,4,\dots}^{N_z-1} v_r^{*[i,j,k]} + 2 \sum_{k=3,5,\dots}^{N_z-2} v_r^{*[i,j,k]} \right).$$

After obtaining the approximation for the inner integral,  $I_Q$ , the flow rate may be

found using a second application of Simpson's rule:

$$Q_r^* \approx \frac{N_g \theta_o [\bar{r}^{[i]} (R_* - 1) + 1] \Delta \bar{\theta}}{6} \left( h_*^{[i,1]} I_Q^{[i,1]} + h_*^{[i,N_\theta]} I_Q^{[i,N_\theta]} \right. \\ \left. + 4 \sum_{j=2,4,\dots}^{N_\theta-1} h_*^{[i,j]} I_Q^{[i,j]} + 2 \sum_{j=3,5,\dots}^{N_\theta-2} h_*^{[i,j]} I_Q^{[i,j]} \right).$$

However, as can be noted from Equation (4.2),  $v_r^*$ , and therefore  $I_Q$ , is defined on even  $j$ -nodes. Using second order averaging for the terms defined in the above equation on odd  $j$ -nodes, the above expression reduces to the following equation:

$$Q_r^* \approx N_g \theta_o [\bar{r}^{[i]} (R_* - 1) + 1] \Delta \bar{\theta} \sum_{j=2,4,\dots}^{N_\theta-1} h_*^{[i,j]} I_Q^{[i,j]}.$$

Similar expressions were obtained for the normal force,  $F_z^*$ , the tangential forces,  $F_{p,h}^*$ ,  $F_{\theta,0}^*$ , and  $F_{\theta,h}^*$ , and the frictional moment,  $M_F^*$ .

## 4.5 Numerical Verification

The solutions presented in this section offer specialized check cases for the numerical algorithm. The first section discusses isoviscous axisymmetric solutions and presents an analytical solution. The second section discusses an isoviscous solution with radial grooves. In each section, numerical and analytical results are compared.

### 4.5.1 Isoviscous Axisymmetric Solutions

This section discusses isoviscous axisymmetric solutions of the governing equations. Since the flow field is incompressible, the assumption of constant viscosity,  $\mu_* = 1$ , decouples the energy equation from the momentum equations. We consider only the hydrodynamic dependent variables:  $p_*$ ,  $v_r^*$ ,  $v_\theta^*$ , and  $v_z^*$ . The assumption of

axisymmetry implies all changes in the  $\theta_*$ -direction are zero,  $\frac{\partial}{\partial \theta_*} = 0$ . This is accomplished by using a film thickness which is a function of radius only,  $h_* = h_*(r_*)$ .

Under these conditions, a solution for  $v_\theta^*$  may be obtained using Equations (3.47) and (3.54):

$$v_\theta^* = \Omega_* r_* \left(1 - \frac{z_*}{h_*}\right). \quad (4.33)$$

Equations (3.46) and (3.54) may be used to obtain an expression for  $v_r^*$  in terms of the pressure:

$$v_r^* = \frac{1}{2} \frac{\partial p_*}{\partial r_*} \left(z_*^2 - z_* h_*\right). \quad (4.34)$$

To obtain a solution for the pressure field, the above equation and (3.45) are integrated with respect to  $z_*$ , from  $z_* = 0$  to  $z_* = h_*$ . The following differential equation results from combining the resulting expressions:

$$\frac{\partial}{\partial r_*} \left( r_* h_* \frac{\partial p_*}{\partial r_*} \right) = 0. \quad (4.35)$$

The boundary conditions listed in Equation (3.55) may be used with Equation (4.35) to find the pressure field. Once the pressure is obtained, the radial velocity may be obtained using Equation (4.34). The axial velocity may be obtained from the differential form of Equation (3.45) along with Equation (3.54).

An analytical solution was obtained for a radially varying film thickness of the form  $h_* = 1 + b_1 r_*$ , where  $b_1$  is a constant:

$$v_r^* = \frac{P_o^*}{2b_1 r_* h_*^3} \left(z_*^2 - z_* h_*\right),$$

$$v_\theta^* = \Omega_* r_* \left(1 - \frac{z_*}{h_*}\right),$$

$$v_z^* = \frac{b_1 p_o^* z_*^2}{2b_2 r_* h_*^3} \left( \frac{z_*}{h_*} - 1 \right),$$

$$p_* = \frac{p_o^*}{b_2} \left[ \left( \frac{2h_* + 1}{2h_*^2} \right) - \left( \frac{2h_i^* + 1}{2h_i^{*2}} \right) + \ln \left[ \frac{(h_* - 1) h_i^*}{(h_i^* - 1) h_*} \right] \right].$$

Here, the dimensionless radial inlet and outlet film thicknesses were defined as  $h_i^* = 1 + b_1$  and  $h_o^* = 1 + b_1 R_*$ . The constant  $b_2$  is defined as follows:

$$b_2 = \left( \frac{2h_o^* + 1}{2h_o^{*2}} \right) - \left( \frac{2h_i^* + 1}{2h_i^{*2}} \right) \ln \left[ \frac{(h_o^* - 1) h_i^*}{(h_i^* - 1) h_o^*} \right].$$

While the flow is axisymmetric, the film varies linearly with  $r_*$ . In the limit that the film thickness is constant,  $b_1 = 0$ , one can show that the axial velocity vanishes using L'Hopital's rule. Intuition suggests this feature is a necessity from mass continuity arguments.

Figures 4.2 through 4.5 show a comparison between the analytical and numerical solutions using  $R_* = \frac{5}{3}$ ,  $\Omega_* = 1$ ,  $p_{*0} = -1.393$ , and  $b_1 = 1$ . Using these specified parameters, the reader can verify that  $h_i^* = 2$ ,  $h_o^* = \frac{8}{3}$ , and  $b_2 = 0.043456$ .

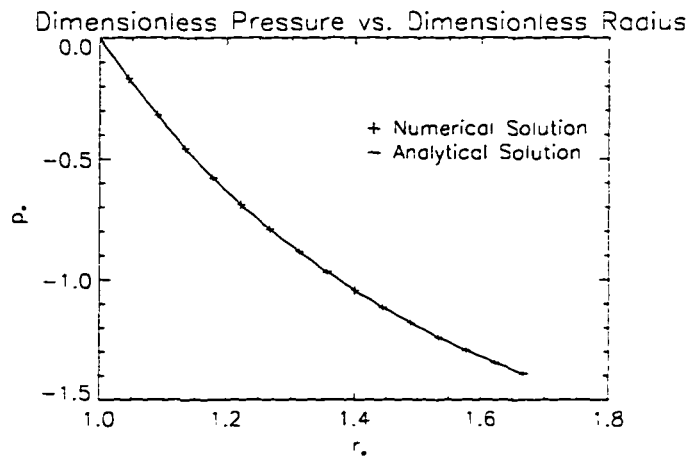


Figure 4.2: Numerical and Analytical Pressure Profiles

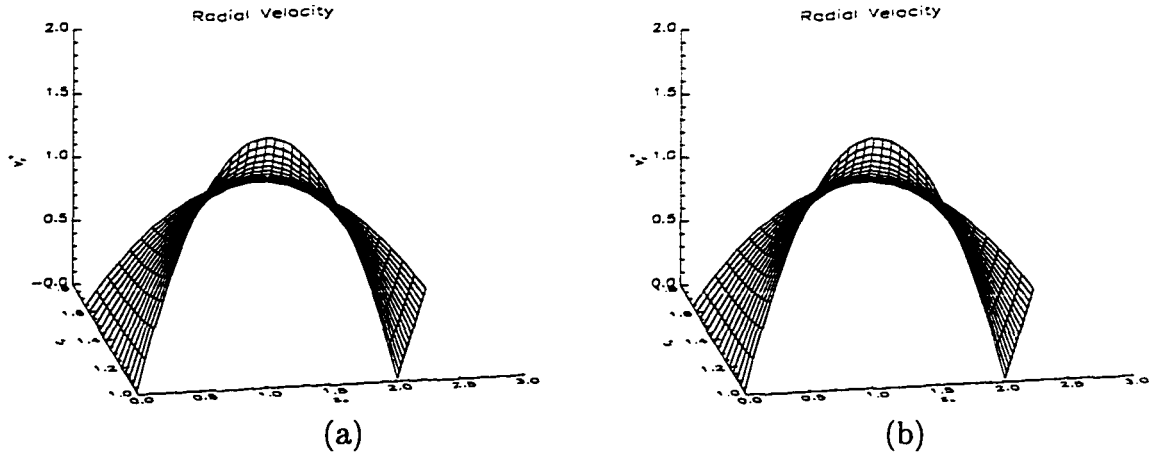


Figure 4.3: (a) Numerical and (b) Analytical Radial Velocity Profiles

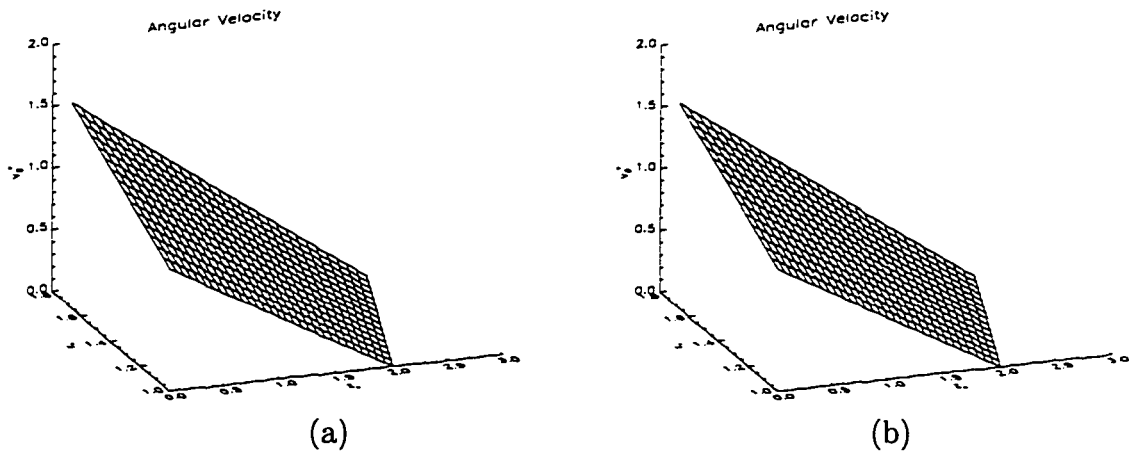


Figure 4.4: (a) Numerical and (b) Analytical Angular Velocity Profiles

A convergence study on the velocity components was completed using the following error equation:

$$\text{error} = \frac{\sqrt{\sum_i \sum_j \sum_k (v_A - v_N)^2}}{\mathcal{N}}$$

Here,  $v_A$  and  $v_N$  respectively denote analytically and numerically predicted velocity components, and  $\mathcal{N}$  represents the total number of nodes for a particular velocity component. Summations are taken over the radial, angular, and axial grid locations. This error was presumed to be a function of grid resolution. The results from this error



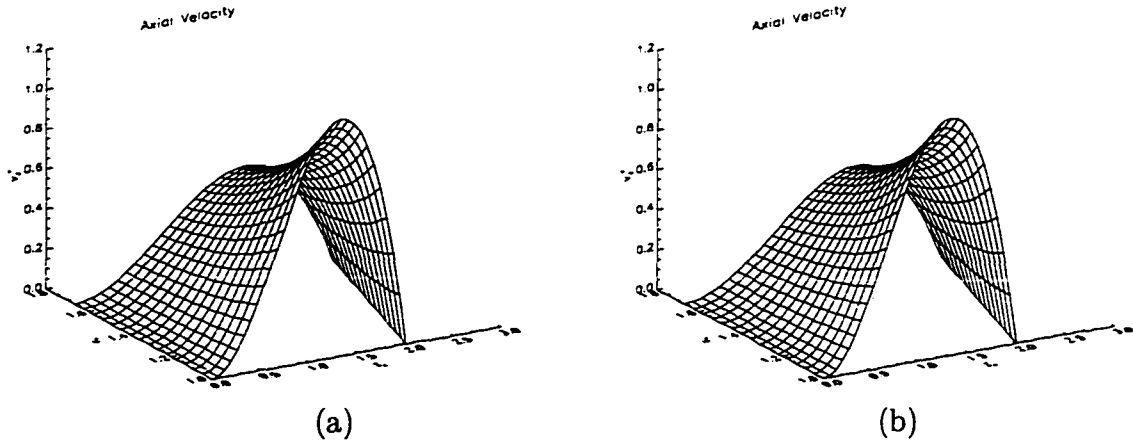


Figure 4.5: (a) Numerical and (b) Analytical Axial Velocity Profiles

analysis are shown in Figure 4.6. In this study, while the computational grid spacings

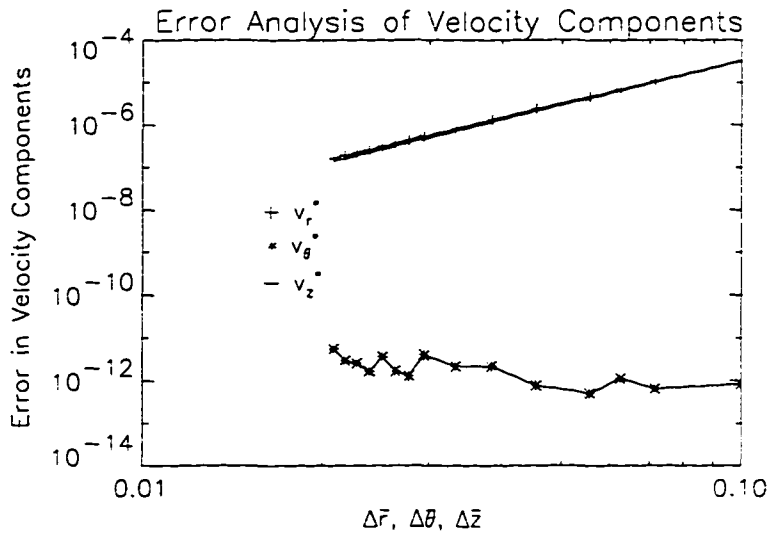


Figure 4.6: Error Analysis for Isoviscous Axisymmetric Check Case

were varied, the relative size of these grid spacings were held fixed:  $\Delta\bar{r} = \Delta\bar{\theta} = \Delta\bar{z}$ . From Figure 4.6, the error in the numerically predicted angular velocity distribution is round-off error. In other words, there is no truncation error in the prediction of the angular velocity component. Further, the error in the radial and axial components appear similar in magnitude over the range of grid spacings examined. The results from

these two components indicate that the measured order of accuracy was  $O(\Delta\bar{r}^{3.456})$  for  $v_r^*$  and  $O(\Delta\bar{r}^{3.379})$  for  $v_z^*$ . This is an improvement over the theoretical order of accuracy,  $O(\Delta\bar{r}^2)$ . While no formal truncation error analysis was completed, it is believed that this improvement is a result of the symmetry present in the problem.

In addition, the clutch performance parameters, mentioned previously, were obtained for this check case:

$$\begin{aligned} Q_r^* &= -\frac{\pi p_o^*}{6b_2}, & F_z^* &= 1 + \frac{2p_o^*S}{b_2b_1^2(R_*^2 - 1)}b_3, \\ F_{\theta,0}^* &= -F_{\theta,h}^* = -\frac{2\pi\Omega_*S\epsilon G}{b_1^3} \left[ \frac{h_o^{*2} - h_i^{*2}}{2} - 2(h_o^* - h_i^*) + \ln \frac{h_o^*}{h_i^*} \right], \\ F_{p,h}^* &= 0, & M_F &= -\frac{2\pi\Omega_*S\epsilon Gb_4}{b_1^4}, \end{aligned}$$

where,

$$\begin{aligned} b_3 &= (h_o^* - h_i^*) - \frac{1}{2} \ln \frac{h_o^*}{h_i^*} + \frac{1}{2} \left( \frac{1}{h_o^*} - \frac{1}{h_i^*} \right) - \left( \frac{2h_i^* + 1}{2h_i^{*2}} \right) \left( \frac{h_o^{*2} - h_i^{*2}}{2} - h_o^* + h_i^* \right) \\ &\quad + \frac{(h_o^* - 1)^2}{4} (2 \ln(h_o^* - 1) - 1) - \frac{(h_i^* - 1)^2}{4} (2 \ln(h_i^* - 1) - 1) \\ &\quad - \frac{h_o^{*2}}{4} (2 \ln h_o^* - 1) + \frac{h_i^{*2}}{4} (2 \ln h_i^* - 1) + (h_o^* \ln h_o^* - h_o^*) - (h_i^* \ln h_i^* - h_i^*) \\ &\quad - \ln \left( \frac{h_i^* - 1}{h_i^*} \right) \left( \frac{h_o^{*2} - h_i^{*2}}{2} - h_o^* + h_i^* \right), \\ b_4 &= \frac{h_o^{*3} - h_i^{*3}}{3} - \frac{3}{2} (h_o^{*2} - h_i^{*2}) + 3(h_o^* - h_i^*) - \ln \frac{h_o^*}{h_i^*}. \end{aligned}$$

It should be clear that the analytical expressions are cumbersome for this relatively simple flow field. Nevertheless, agreement was found between the numerically predicted performance parameters and the analytical expressions above. For the specified dimensionless parameters, along with  $S = 0.598$  and  $\epsilon = 8.33 \times 10^{-4}$ , the clutch performance parameters were computed:

$$Q_r^* = 16.79, \quad F_z^* = 0.456,$$

$$F_{\theta,0}^* = -F_{\theta,h}^* = -2.843 \times 10^{-4},$$

$$M_F^* = -3.90 \times 10^{-4}, \quad \mu_F = 6.23 \times 10^{-4}.$$

#### 4.5.2 Isoviscous, Radially Grooved Solution

This solution considers a non-axisymmetric film thickness. The geometry under consideration is similar to a parallel-step slider bearing, or Rayleigh Step Bearing. Similar two-dimensional problems are solved by Hamrock [22] in Cartesian coordinates and Gross [18] in cylindrical coordinates. As in the previous analytical solution, the lubricant was taken as isoviscous which decoupled the momentum and energy equations. Results are presented for dimensionless pressure distribution,  $p_*$ .

The film thickness was defined in parts:

$$h_* = \begin{cases} 1 & ; \quad 0 \leq \theta_* < \frac{\theta_o}{3} \\ 2 & ; \quad \frac{\theta_o}{3} \leq \theta_* < \frac{2\theta_o}{3} \\ 1 & ; \quad \frac{2\theta_o}{3} \leq \theta_* \leq \theta_o \end{cases} . \quad (4.36)$$

Unlike the previous section, the film thickness depends on the angular coordinate,  $\theta_*$ , and is not continuous. In Chapter 3, we assumed that there were no severe gradients in the film thickness. Here, we temporarily relax this assumption and assume Equations (3.64-3.72) are still valid. We note that this violates the strict ordering scheme developed earlier so that the solutions obtained are not rational limits of the Navier Stokes Equations. Nevertheless, such analyses have yielded results which compare favorably with experiments and are consistent with Hamrock and Gross.

Analytical solutions can be obtained because the pressure adjacent to each parallel

surface satisfies Laplace's equation [18, 22]:

$$r_*^2 \frac{\partial^2 p_*}{\partial r_*^2} + r_* \frac{\partial p_*}{\partial r_*} + \frac{\partial^2 p_*}{\partial \theta_*^2} = 0.$$

In addition to the periodic boundary conditions at  $\theta_* = 0$  and  $\theta_* = \theta_o$  listed in Equation (3.55), the pressure and flow rates per unit depth across the planes  $\theta_* = \frac{\theta_o}{3}$  and  $\theta_* = \frac{2\theta_o}{3}$  are required to be continuous. The angular flow rate per unit depth is defined as

$$Q_\theta = \int_0^{h(r,\theta)} v_\theta dz,$$

or

$$Q_\theta^* = \frac{Q_\theta}{\Omega_1 R_i h_o} = \int_0^{h_*(r_*,\theta_*)} v_\theta^* dz_*,$$

in dimensionless terms. For isoviscous flow, Equations (3.47) and (3.54) may be used to predict an angular velocity in terms of the pressure gradient:

$$v_\theta^* = \frac{(z_*^2 - z_* h_*)}{2r_*} \frac{\partial p_*}{\partial \theta_*} + r_* \Omega_* \left(1 - \frac{z_*}{h_*}\right).$$

By substituting this equation into the expression for  $Q_\theta^*$  and requiring the flow rates per unit length to be continuous as mentioned above, the boundary conditions on pressure may be stated mathematically as follows:

$$p_* \Big|_{\theta_* = \frac{\theta_o^+}{3}} = p_* \Big|_{\theta_* = \frac{\theta_o^-}{3}} \quad \left[ -\frac{h_*^3}{12r_*} \frac{\partial p_*}{\partial \theta_*} + \frac{\Omega_* r_* h_*}{2} \right]_{\theta_* = \frac{\theta_o^+}{3}} = \left[ -\frac{h_*^3}{12r_*} \frac{\partial p_*}{\partial \theta_*} + \frac{\Omega_* r_* h_*}{2} \right]_{\theta_* = \frac{\theta_o^-}{3}}$$

$$p_* \Big|_{\theta_* = \frac{2\theta_o^+}{3}} = p_* \Big|_{\theta_* = \frac{2\theta_o^-}{3}} \quad \left[ -\frac{h_*^3}{12r_*} \frac{\partial p_*}{\partial \theta_*} + \frac{\Omega_* r_* h_*}{2} \right]_{\theta_* = \frac{2\theta_o^+}{3}} = \left[ -\frac{h_*^3}{12r_*} \frac{\partial p_*}{\partial \theta_*} + \frac{\Omega_* r_* h_*}{2} \right]_{\theta_* = \frac{2\theta_o^-}{3}}$$

Further, we require a homogeneous condition on  $r_* = R_*$ . Namely, from Equation (3.55),  $p_o^* = 0$ .

The solution for the pressure distribution, in each region where the film thickness is continuous, may be stated as follows:

$$p_* = \sum_{n=1}^{\infty} [\beta_n \cosh(\lambda_n \theta_*) + \gamma_n \sinh(\lambda_n \theta_*)] \sin(\lambda_n \ln r_*) \quad (4.37)$$

The coefficients,  $\beta_n$  and  $\gamma_n$ , are defined for the three separate continuous regions:

$$\beta_n = \begin{cases} 0 & ; 0 \leq \theta_* < \frac{\theta_o}{3} \\ \Gamma_n \left( 18 \sinh \frac{\lambda_n \theta_o}{3} - 22 \sinh \frac{\lambda_n \theta_o}{3} - 14 \sinh \lambda_n \theta_o - 4 \sinh \frac{2\lambda_n \theta_o}{3} \right) & ; \frac{\theta_o}{3} \leq \theta_* < \frac{2\theta_o}{3} \\ -\Gamma_n \left( -32 \sinh \frac{4\lambda_n \theta_o}{3} + 18 \sinh \frac{\lambda_n \theta_o}{3} + 28 \sinh \lambda_n \theta_o \right. \\ \quad \left. + 18 \sinh \frac{\lambda_n \theta_o}{3} - 32 \sinh \frac{2\lambda_n \theta_o}{3} \right) & ; \frac{2\theta_o}{3} \leq \theta_* \leq \theta_o \end{cases}$$

$$\gamma_n = \begin{cases} 2\Gamma_n \left( 18 \cosh \frac{2\lambda_n \theta_o}{3} - 32 \cosh \frac{\lambda_n \theta_o}{3} + 14 \right) & ; 0 \leq \theta_* < \frac{\theta_o}{3} \\ -\Gamma_n \left( 18 \cosh \frac{4\lambda_n \theta_o}{3} - 14 + 14 \cosh \frac{\lambda_n \theta_o}{3} - 14 \cosh \lambda_n \theta_o \right. \\ \quad \left. - 4 \cosh \frac{2\lambda_n \theta_o}{3} \right) & ; \frac{\theta_o}{3} \leq \theta_* < \frac{2\theta_o}{3} \\ \Gamma_n \left( -32 \cosh \frac{4\lambda_n \theta_o}{3} + 18 \cosh \frac{\lambda_n \theta_o}{3} + 28 \cosh \lambda_n \theta_o \right. \\ \quad \left. + 18 \cosh \frac{5\lambda_n \theta_o}{3} - 32 \cosh \frac{2\lambda_n \theta_o}{3} \right) & ; \frac{2\theta_o}{3} \leq \theta_* \leq \theta_o \end{cases}$$

Here,  $\Gamma_n$  and  $\lambda_n$  are defined as follows:

$$\Gamma_n = \frac{\frac{-12\Omega_*}{\ln R_*} \left[ \frac{1 - R_*^2 \cos n\pi}{(\lambda_n)^2 + 4} \right]}{-64 - 98 \cosh \frac{\lambda_n \theta_o}{3} + 162 \cosh \lambda_n \theta_o},$$

$$\lambda_n = \frac{n\pi}{\ln R_*}.$$

A comparison of the analytical and numerically predicted pressure solutions is shown in Figure 4.7. The numerical and analytical solutions used the following dimensionless parameters:  $R_* = \frac{5}{3}$ ,  $\Omega_* = 1$ , and  $\theta_o = 0.3$ . The infinite series in Equation (4.37) was truncated after the first one hundred terms.

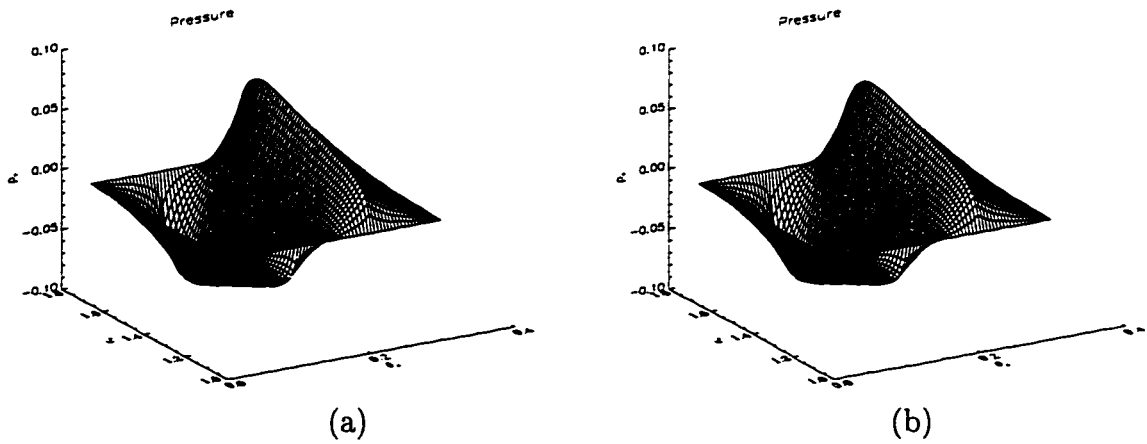


Figure 4.7: (a) Numerical and (b) Analytical Pressure Profiles using  $N_r = N_\theta = 125$

A more detailed comparison was completed by way of a convergence study. The following equation was used to evaluate the error in the analytical and numerical solutions:

$$\text{error} = \frac{\sqrt{\sum_i \sum_j (p_A - p_N)^2}}{\mathcal{N}}.$$

Similar to the previous case,  $p_A$  and  $p_N$  respectively denote analytically and numerically predicted pressure values, and  $\mathcal{N}$  represents the total number of nodes on which the solution was evaluated. Since the pressure is independent of  $z$ , summations are taken over the radial and angular indices only. As in the previous case, while the computational grid spacings were varied, the relative size of these grid spacings were held fixed:  $\Delta\bar{r} = \Delta\bar{\theta}$ . Figure 4.8 shows the results of this convergence study. Local peaks in the figure occur when the number of angular nodes,  $N_\theta$ , equals 37, 61, 85, 109, 133, and 157. For each of these scenarios, angular grid points lie exactly on the lines  $\bar{\theta} = \frac{1}{3}$  and  $\bar{\theta} = \frac{2}{3}$  where the discontinuities in film thickness occur. This can be shown using Equations (4.1) and (4.3). Considering both cases separately (where angular grid

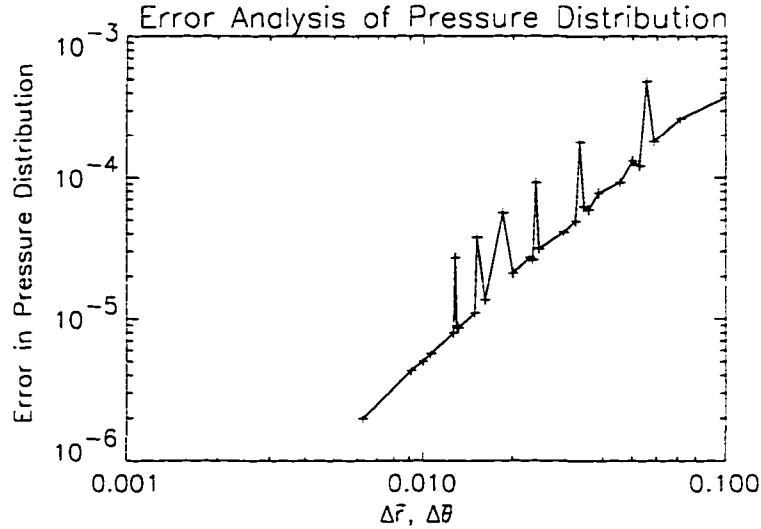


Figure 4.8: Error Analysis for Isoviscous Radially Grooved Case

points do and do not lie on the mentioned lines), the error decreases with decreasing grid spacing. The measured order of accuracy using  $N_\theta = 37, 61, 85, 109, 133,$  and  $157$  was found to be  $O(\Delta\bar{r}^{1.968})$  and  $O(\Delta\bar{r}^{1.950})$  for the remaining cases.

Once the pressure distribution is known, it is possible to obtain the radial and angular velocity components via the momentum equations.

$$v_r^* = \frac{1}{2} \frac{\partial p_*}{\partial r_*} (z_*^2 - z_* h_*)$$

$$v_\theta^* = \frac{1}{2r_*} \frac{\partial p_*}{\partial \theta_*} (z_*^2 - z_* h_*) + \Omega_* r_* \left(1 - \frac{z_*}{h_*}\right)$$

Note that while the pressure distribution is continuous,  $\frac{\partial p_*}{\partial \theta_*}$  is not everywhere continuous. This is shown in Figure 4.7 for both the exact solution and the numerical solution. Specifically, at the film thickness discontinuities the pressure gradient is not continuous. This shortcoming, overlooked throughout hydrodynamic lubrication theory, renders the angular velocity discontinuous at these planes.

Several statements can be made about this check case. First some general statements can be inferred regarding the dependent variables:  $v_r^*$ ,  $v_\theta^*$ ,  $v_z^*$ , and  $p_*$ , given an arbitrary film thickness. If the film thickness is continuous, then  $v_r^*$ ,  $v_\theta^*$ ,  $p_*$ , and  $\nabla p_*$  are continuous. If the film thickness, and its derivative are continuous ( $C^1$ ) then  $v_r^*$ ,  $v_\theta^*$ ,  $v_z^*$ ,  $p_*$ , and  $\nabla p_*$  are continuous. However, if the film thickness is discontinuous, then  $p_*$  is continuous, but  $\nabla p_*$  is discontinuous. These comments are justified in Appendix C by considering a simplified two-dimensional lubrication problem. Second, this geometry could be that of a legitimate clutch problem. Payvar [43, 44] considers this problem with the inclusion of diffusion terms in the angular direction. It is expected that these terms, and further no slip conditions, are required to smooth out the discontinuities. Nevertheless, the thin-film limit is an approximation which attempts to describe the physical problem.



## CHAPTER 5

### RESULTS

This chapter presents the results obtained for this dissertation. In the first section, the solution for a sinusoidally varying film is given. Here, the velocity, pressure, and temperature profiles are presented. In the second section, the effects of variable viscosity on the constant film case will be examined. Here, the effect on clutch performance of varying four independent parameters is examined. These results are compared to the analytical solution of the isoviscous, constant film case. In the third section, results indicating the effects of grooves are given. This section is divided into two parts: cavitation results and non-cavitation results. In the cavitation part, the effects of varying the Sommerfeld number and dimensionless groove depth on the normal load are given. In the non-cavitation part, the effects of varying groove depth on several performance parameters are given. In the fourth section, a generalization of the mathematical model to include heat transfer in the plates is given. The purpose of this section is to show how the lubrication theory may be coupled to a larger conjugate problem. Here, results are given for constant film shapes, variable film shapes, constant viscosity, and variable viscosity.

#### 5.1 Model Solution for a Sinusoidally Varying Film Thickness

In this section, velocity, pressure, and temperature profiles are given for the fol-

lowing film thickness:

$$h = h_o + \frac{h_{g\theta}}{2} \left[ 1 - \cos \left( \frac{2\pi\theta}{\theta_o} \right) \right]. \quad (5.1)$$

Note that  $h$  is periodic and has the following properties:

$$h(r, 0) = h(r, \theta_o) = h_o, \quad h\left(r, \frac{\theta_o}{2}\right) = h_o + h_{g\theta}, \quad h\left(r, \frac{\theta_o}{2} + \theta'\right) = h\left(r, \frac{\theta_o}{2} - \theta'\right),$$

where  $\theta'$  varies between 0 and  $\frac{\theta_o}{2}$ , and  $h_{g\theta}$  is a constant. In dimensionless terms, the film thickness is as follows:

$$h_* = \frac{h}{h_o} = 1 + \frac{h_{g\theta}^*}{2} \left[ 1 - \cos \left( \frac{2\pi\theta_*}{\theta_o} \right) \right], \quad (5.2)$$

where  $h_{g\theta}^* = \frac{h_{g\theta}}{h_o}$ . The dimensionless film thickness is shown in Figure 5.1. Dimen-

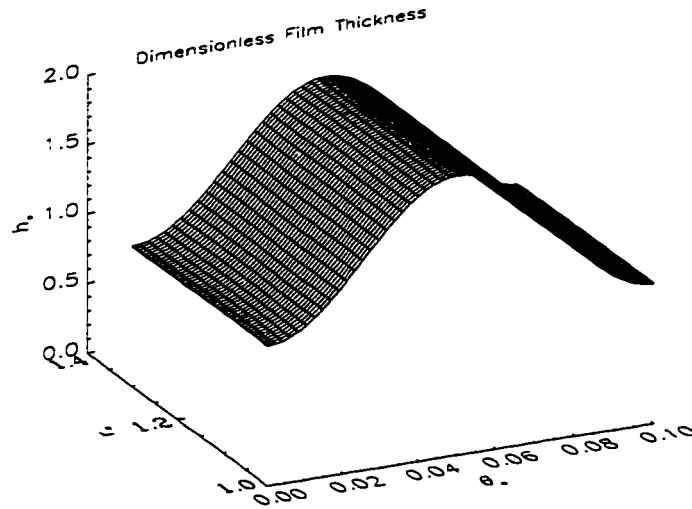


Figure 5.1: Film thickness profile from Equation 5.2, using  $N_r = 49$ ,  $N_\theta = 49$ ,  $R_* = 1.3$ ,  $\theta_o = 0.1$ , and  $h_{g\theta}^* = 1.0$ .

sionless velocity, pressure, and temperature profiles are shown in Figures 5.2 through 5.6. Here, dimensionless parameters which were held fixed for this solution are listed in Table 5.1.

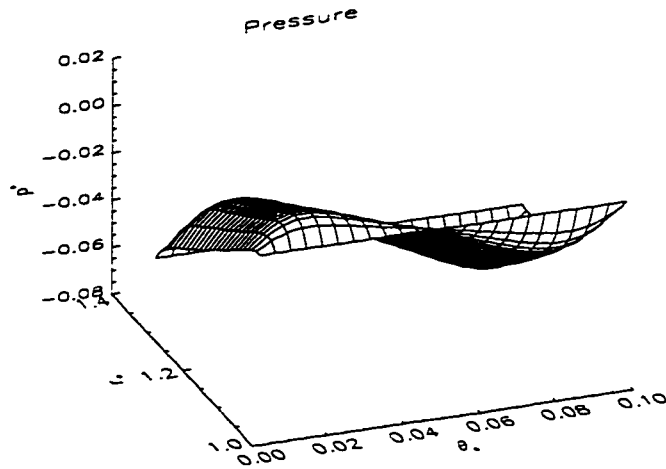


Figure 5.2: Pressure Profile

$\epsilon = 1.0 \times 10^{-3}$	$Gr = 4.93$	$Br = 1.21 \times 10^{-3}$	$\Omega_* = -1.0$
$R_* = 1.3$	$p_o^* = -4.91 \times 10^{-2}$	$h_{g\theta} = 1.0$	$\theta_o = 0.1$
$K_1^* = 165.83$	$K_2^* = 0.663$	$K_3^* = 1.5$	$m = 4.6384$
$N_r = 49$	$N_\theta = 49$	$N_z = 25$	

Table 5.1: CONSTANT PARAMETERS FOR RESULTS PRESENTED IN SECTION 5.1

The pressure distribution, shown in Figure 5.2, satisfies the boundary conditions given in Equation (3.42). In particular, a radial pressure gradient, evident in the figure, is partially due to the enforcement of the radial boundary conditions:  $p_*(1, \theta) = 0$  and  $p_*(R_*, \theta) = p_o^*$ . However, the relative angular velocity of the separator plate also plays a role in determining the pressure distribution. Since the relative angular velocity of the separator plate,  $\Omega_*$ , is negative, the angular inlet section of the domain is  $\theta_* > \frac{\theta_o}{2}$ , and the angular outlet section is  $\theta_* < \frac{\theta_o}{2}$ . The dimensionless lubricant

pressure decreases upon entering the inlet section until it reaches a minimum. Beyond this point, at smaller values of  $\theta_*$ , the pressure increases until it reaches a maximum. The pressure decreases beyond this maximum, and exhibits periodicity as indicated in Equation (3.42).

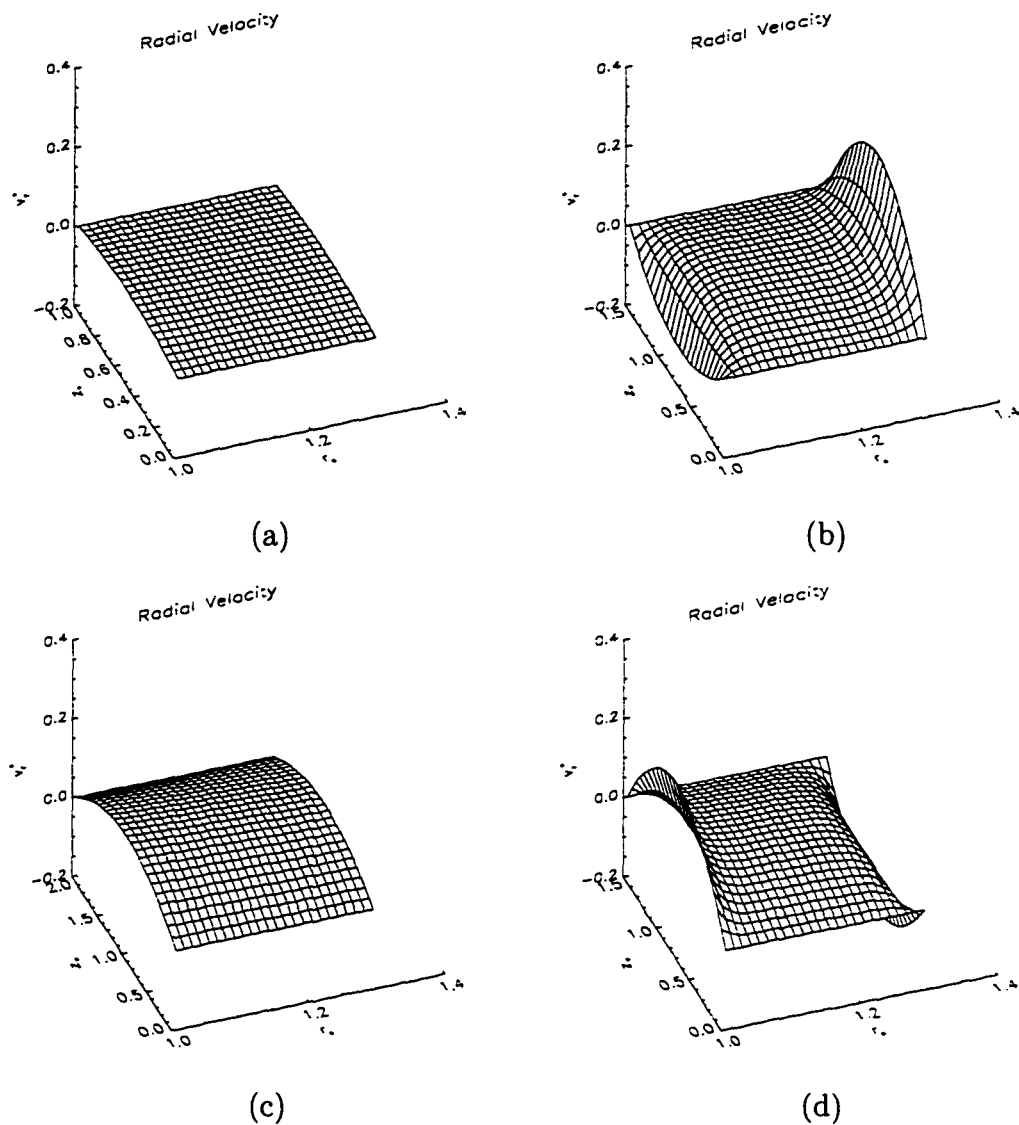


Figure 5.3: Radial Velocity Profiles at  $\theta_* =$  (a) 0, (b)  $\frac{\theta_0}{4}$ , (c)  $\frac{\theta_0}{2}$ , and (d)  $\frac{3\theta_0}{4}$ .

The velocity components, shown in Figures 5.3, 5.4, and 5.5, are shown in the  $r_* - z_*$  plane for four values of  $\theta_*$ . All velocity components satisfy the no-slip condi-

tion, indicated by Equation (3.41). Further, a recirculation pattern is evident in the velocity field.

The temperature distribution, shown in Figure 5.6, satisfies the adiabatic conditions, Equation (3.60), at the clutch plates, as well as the periodicity and inlet temperature conditions given by Equation (3.56). The temperature at the inner radius is equal to the inlet radial temperature,  $T_* = 1$ . At larger radii, the temperature of the lubricant increases until it reaches a maximum at the outer radius. In this scenario, it was found that the maximum temperature occurred at  $\theta_* = \frac{\theta_o}{2}$  and  $z_* = h$ . This may partially be explained by the fact that the pressure gradient is severe at this location resulting in large viscous dissipation.

## 5.2 Effects of Variable Viscosity on the Constant Film Thickness Case

In this section, several clutch performance parameters are studied as functions of four independent parameters: the outer pressure,  $p_o$ , the inlet temperature,  $T_o$ , the relative angular velocity,  $\Omega_d$ , and the film thickness,  $h_o$ . The performance parameters presented are the flow rate,  $Q_r$ , the normal force,  $F_z$ , the tangential force due to viscous shearing on the separator plate,  $F_{\theta,0}$ , the frictional moment,  $M_F$ , the coefficient of friction,  $\mu_F$ , and the maximum temperature rise,  $\Delta T_{max}$ . The maximum temperature rise is the largest increase in temperature found in the lubricant domain. In all cases it was found that the maximum temperature was located at  $r = R_o$ , and the minimum temperature was located at  $r = R_i$ . It is assumed that the film is constant,  $h = h_o$ , and the viscosity is given by Equation (3.15) using SAE 10 oil. Constant

parameters which were held fixed are listed in Table 5.2.

$$\begin{array}{lll}
 N_r = 31 & N_\theta = 31 & N_z = 31 \\
 R_i = 5.0 \times 10^{-2} \text{ m} & R_o = 6.5 \times 10^{-2} \text{ m} & \theta_o = 0.1 \text{ rad} \\
 p_i = 2.5 \text{ MPa} & \rho = 920 \frac{\text{kg}}{\text{m}^3} & c = 2.0 \frac{\text{kJ}}{\text{kg K}} \quad k = 0.14 \frac{\text{W}}{\text{m K}}
 \end{array}$$

Table 5.2: CONSTANT PARAMETERS FOR RESULTS PRESENTED IN SECTION 5.2

Assuming that the viscosity is constant,  $\mu = \mu_o$ , the solution for the hydrodynamic variables,  $v_r$ ,  $v_\theta$ ,  $v_z$ , and  $p$ , is as follows:

$$v_r = \frac{(p_o - p_i)(z^2 - zh)}{2\mu_o r \ln \frac{R_o}{R_i}}, \quad (5.3)$$

$$v_\theta = \Omega_d r \left(1 - \frac{z}{h_o}\right), \quad (5.4)$$

$$v_z = 0, \quad (5.5)$$

$$p = p_i + (p_o - p_i) \frac{\ln \frac{r}{R_i}}{\ln \frac{R_o}{R_i}}. \quad (5.6)$$

In this scenario, the energy equation reduces to the following relation:

$$\rho c v_r \frac{\partial T}{\partial r} = k \frac{\partial^2 T}{\partial z^2} + \mu_o \left[ \left( \frac{\partial v_r}{\partial z} \right)^2 + \left( \frac{\partial v_\theta}{\partial z} \right)^2 \right], \quad (5.7)$$

which may be used with the appropriate boundary conditions,

$$\text{on } r = R_i \quad T = T_o,$$

$$\frac{\partial T}{\partial z} \Big|_{z=0} = \frac{\partial T}{\partial z} \Big|_{z=h_o} = 0,$$

to obtain the temperature. In short, a closed form analytic solution for the temperature field was not obtained for the isoviscous case. Nevertheless, five of the six

performance parameters may be stated explicitly:

$$Q_r = \frac{\pi h_o^3 (p_i - p_o)}{6\mu_o \ln \frac{R_o}{R_i}}, \quad (5.8)$$

$$F_z = \pi \left[ p_o R_o^2 - p_i R_i^2 - \frac{(p_o - p_i)(R_o^2 - R_i^2)}{2 \ln \frac{R_o}{R_i}} \right], \quad (5.9)$$

$$F_{\theta,0} = -\frac{2\pi\Omega_d\mu_o(R_o^3 - R_i^3)}{3h_o}, \quad (5.10)$$

$$M_F = -\frac{\pi\Omega_d\mu_o(R_o^4 - R_i^4)}{2h_o}, \quad (5.11)$$

$$\mu_F = -\frac{4\Omega_d\mu_o(R_o^3 - R_i^3) \ln \frac{R_o}{R_i}}{3h_o \left[ 2(p_o R_o^2 - p_i R_i^2) \ln \frac{R_o}{R_i} - (p_o - p_i)(R_o^2 - R_i^2) \right]}. \quad (5.12)$$

Equations (5.3-5.12) represent the isoviscous, constant film solution. This solution is qualitatively compared to numerically predicted, variable viscosity results given in Figures 5.7 through 5.24.

The effects of varying the outer pressure,  $p_o$ , are illustrated in Figures 5.7 through 5.12 using  $T_o = 300K$  and  $\Omega_d = -100 \frac{rad}{s}$ . Note that increasing the outer pressure decreases the pressure difference,  $p_d = (p_i - p_o)$ . It is found that increasing the pressure difference increases the flow rate,  $Q_r$ , as shown in Figure 5.7. This trend is consistent with the isoviscous case given by Equation (5.8). The normal force,  $F_z$ , increases with increasing outer pressure as indicated in Figure 5.8. This trend is consistent with Equation (5.9) for  $\frac{R_o}{R_i} = 1.3$ . Both the tangential force,  $F_{\theta,0}$ , and the moment  $M_F$ , decrease with increasing outer pressure as shown in Figures 5.9 and 5.10. This effect is due to the viscosity-temperature relation as it can not be explained using Equations (5.10) and (5.11). Both the increasing normal force and decreasing tangential force with increasing outer pressure lead to a decreasing friction coefficient

as shown in Figure 5.11. Depending on whether the film thickness is large or small, the maximum temperature rise will either increase or decrease with increasing outer pressure as shown in Figure 5.12. That is, for large  $h$ , as  $p_d \rightarrow 0$ ,  $\Delta T_{max} \rightarrow 0$ , and for small  $h$ , as  $p_d \rightarrow 0$ ,  $\Delta T_{max} \rightarrow \infty$ . Assuming a finite radial flow, the term  $\mu \left( \frac{\partial v_r}{\partial z} \right)^2$  in the energy equation is the most significant heating term for large  $h$ , and the term  $\mu \left( \frac{\partial v_\theta}{\partial z} \right)^2$  is the most significant heating term for small  $h$ . As the pressure difference goes to zero,  $\mu \left( \frac{\partial v_r}{\partial z} \right)^2$  for large  $h$  goes to zero, resulting in decreased temperature rises. On the other hand, for small  $h$ ,  $\mu \left( \frac{\partial v_\theta}{\partial z} \right)^2$  is nearly unaffected by the pressure difference. However, in this case convection in the radial direction is hindered with decreasing  $p_d$ , resulting in increased temperature rises.

The effects of varying the inlet temperature,  $T_o$ , are illustrated in Figures 5.13 through 5.18 using  $p_o = 0.5 \text{ MPa}$  and  $\Omega_d = -100 \frac{\text{rad}}{\text{s}}$ . In Figure 5.13, the radial flow rate increases with increasing inlet temperature. Since the viscosity decreases with increasing temperature, the resistance to flow decreases and the flow rate increases. This is consistent with Equation (5.8). Unlike the isoviscous normal force given in Equation (5.9), the normal force was found to increase with increasing inlet temperature as shown in Figure 5.14. The tangential force, moment, and friction coefficient were found to decrease with increasing temperature as shown in Figures 5.15, 5.16, and 5.17. This is consistent with the viscosity-temperature relation and Equations (5.10), (5.11), and (5.12). The maximum temperature rise increases for smaller inlet temperatures as shown in Figure 5.18. For small inlet temperatures, the viscosity is high resulting in large viscous dissipation. In other words, high temperature rises are



expected for low inlet temperatures. For the five highest temperature rises shown in Figure 5.18 the ratio of Brinkman to Graetz numbers varies between 0.042 and 0.08. Clearly, when this ratio increases (decreasing film thickness) the maximum temperature rise increases. A particular study, involving the relative order of magnitude of the terms in the energy equation, was performed for this set of operating conditions. Dimensionless results are reported for the maximum values of convection, conduction, and viscous dissipation in Table 5.3. The Graetz and Brinkman numbers were varied

Case #	1	2	3	4	5	6
$h \times 10^6$ (m)	60	8	8	8	8	8
$T_o$ (K)	400	400	425	450	475	500
$Gr \times 10^2$	473	8.40	8.40	8.40	8.40	8.40
$Br \times 10^4$	10	10	7.4	5.4	4.2	3.4
$\left[ v_r^* \frac{\partial T_o}{\partial r_o} \right]_{max} \times 10^2$	9.78	2.37	1.92	1.55	1.30	1.10
$\left[ \bar{\mu} \left( \frac{\partial v_{\theta}^*}{\partial z_o} \right)^2 \right]_{max}$	1.69	1.17	1.41	1.53	1.60	1.63
$\left[ \bar{\mu} \left( \frac{\partial v_z^*}{\partial z_o} \right)^2 \right]_{max}$	446	0.18	0.31	0.48	0.69	0.92
$\left[ Gr v_r^* \frac{\partial T_o}{\partial r_o} \right]_{max} \times 10^4$	4620	20.6	16.1	13.0	10.9	9.24
$\left[ \frac{\partial^2 T_o}{\partial z_o^2} \right]_{max} \times 10^4$	1420	7.00	5.88	4.96	4.30	3.81
$\left[ Br \bar{\mu} \left( \left( \frac{\partial v_{\theta}^*}{\partial z_o} \right)^2 + \left( \frac{\partial v_z^*}{\partial z_o} \right)^2 \right) \right]_{max} \times 10^4$	4480	13.5	12.6	10.8	9.56	8.67

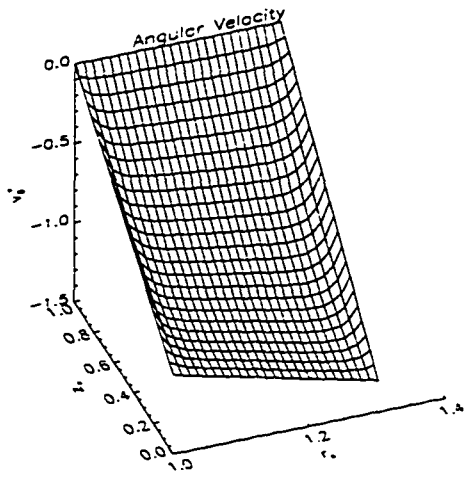
Table 5.3: MAXIMUM VALUES OF TERMS IN DIMENSIONLESS ENERGY EQUATION

by changing the film thickness and inlet temperature respectively. The maximum

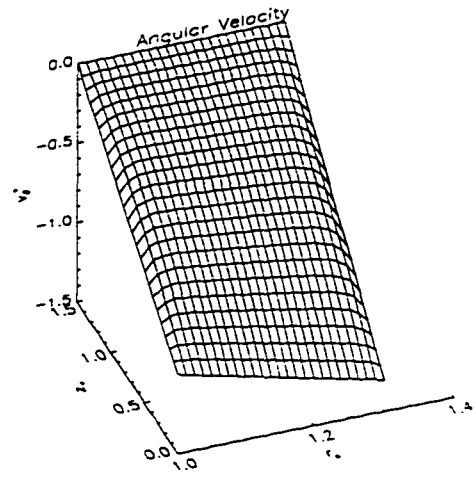
values of the convection, conduction, and viscous dissipation were obtained by examining the entire domain using finite differencing and determining the maximum. The results indicate that while a balance between the terms in the energy equation was achieved, the choice of scaling could be improved. Clearly, the convection, conduction, and viscous dissipation differ by no more than an order of magnitude for any individual case. Furthermore, the numbers given in the last three rows indicate that the contribution of each of these mechanisms is significant. Interestingly, conduction is consistently the smallest. It is believed that this quantity is the smallest because of the adiabatic conditions enforced on the clutch plates. However, as indicated, the dimensionless variables are not  $O(1)$  for the results examined. This is clearly illustrated by the terms  $\left[ v_r^* \frac{\partial T_*}{\partial r_*} \right]_{max}$  and  $\left[ \frac{\partial^2 T_*}{\partial z_*^2} \right]_{max}$  in Table 5.3.

The effects of varying the relative angular velocity,  $\Omega_d$ , are illustrated in Figures 5.19 through 5.24 using  $p_o = 0.5 \text{ MPa}$  and  $T_o = 300 \text{ K}$ . Increasing the magnitude of the slip speed tends to increase the shear rate leading to high temperatures. Results regarding the flow rate, normal force, and maximum temperature rise are consistent with previous discussions. Increasing the slip speed magnitude tends to increase the tangential force, moment, and friction coefficient. This is consistent with the isoviscous trends given in Equations (5.10), (5.11), and (5.12).

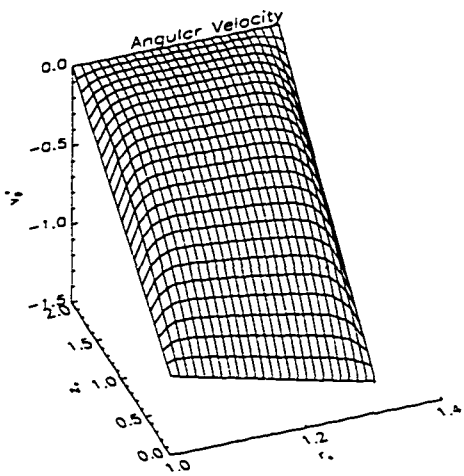
The effects of varying the film thickness are shown in Figures 5.7 through 5.24.



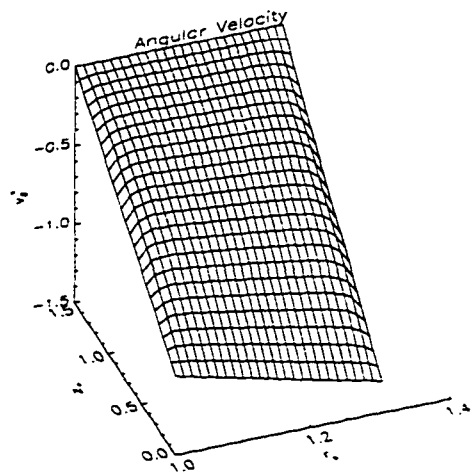
(a)



(b)

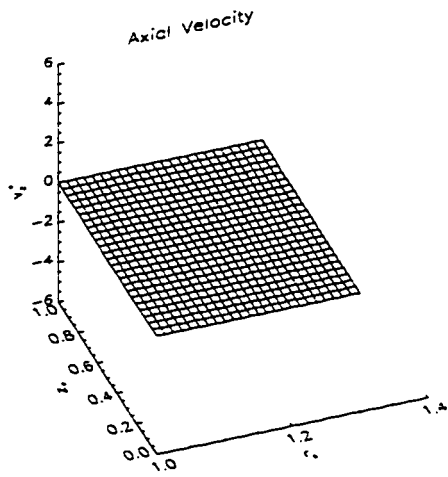


(c)

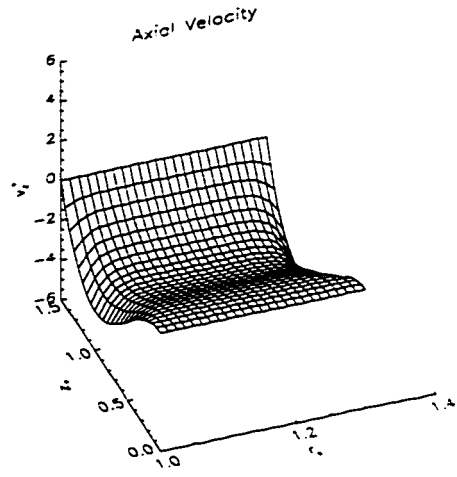


(d)

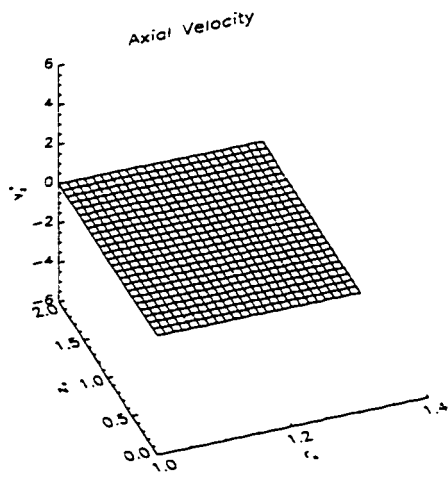
Figure 5.4: Angular Velocity Profiles at  $\theta_* =$  (a) 0, (b)  $\frac{\theta_0}{4}$ , (c)  $\frac{\theta_0}{2}$ , and (d)  $\frac{3\theta_0}{4}$ .



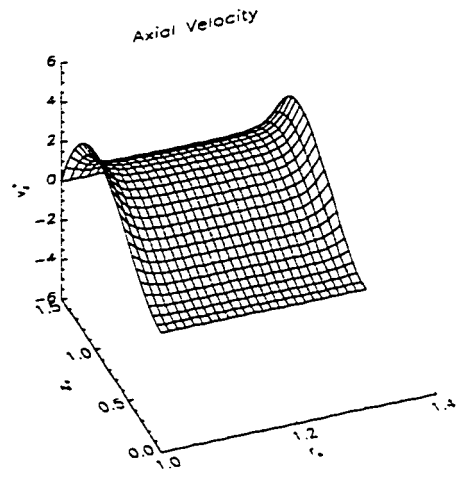
(a)



(b)



(c)



(d)

Figure 5.5: Axial Velocity Profiles at  $\theta_* =$  (a) 0, (b)  $\frac{\theta_0}{4}$ , (c)  $\frac{\theta_0}{2}$ , and (d)  $\frac{3\theta_0}{4}$ .

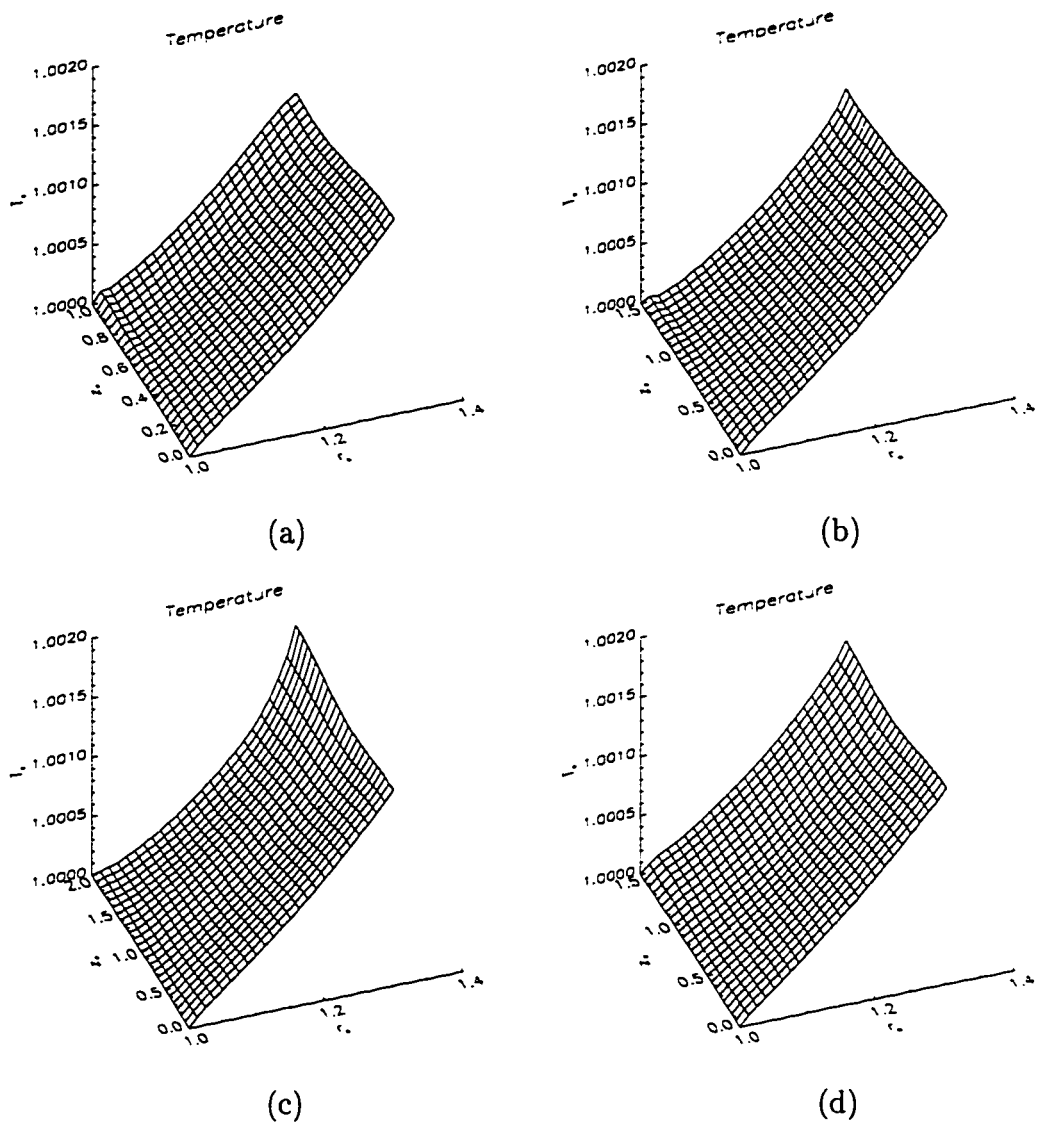


Figure 5.6: Temperature Profiles at  $\theta_* =$  (a) 0, (b)  $\frac{\theta_0}{4}$ , (c)  $\frac{\theta_0}{2}$ , and (d)  $\frac{3\theta_0}{4}$ .

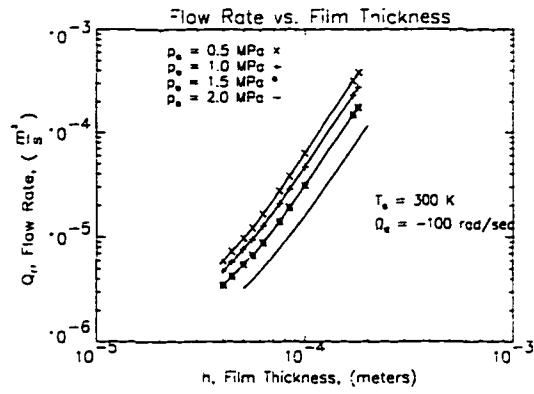


Figure 5.7: Variation of Flow Rate with Outlet Pressure

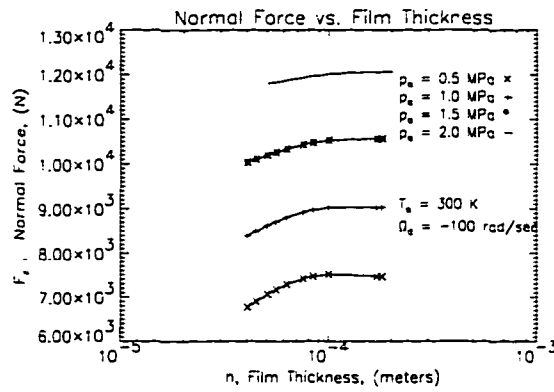


Figure 5.8: Variation of Normal Force with Outlet Pressure

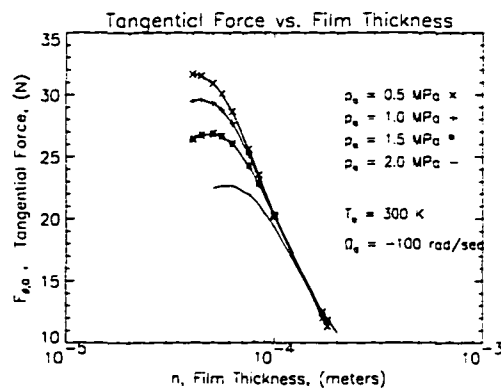


Figure 5.9: Variation of Tangential Force with Outlet Pressure

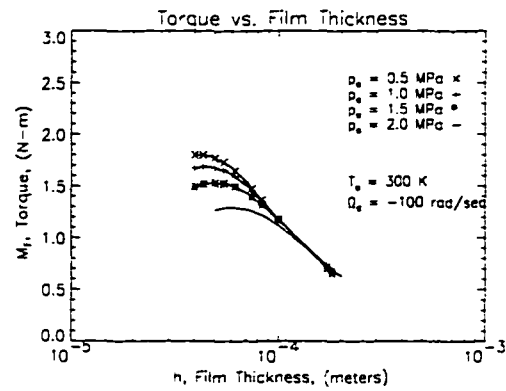


Figure 5.10: Variation of Friction Torque with Outlet Pressure

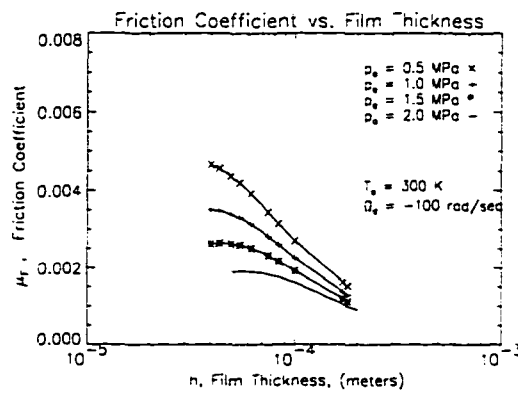


Figure 5.11: Variation of Friction Coefficient with Outlet Pressure

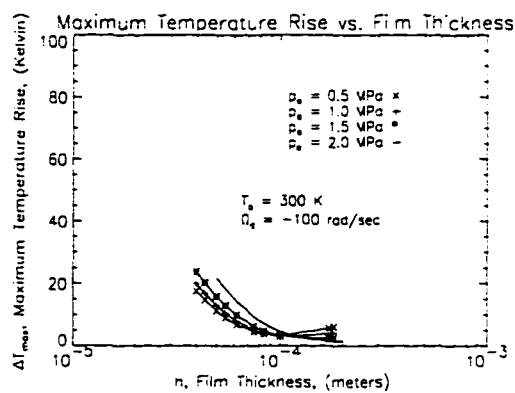


Figure 5.12: Variation of Temperature Rise with Outlet Pressure

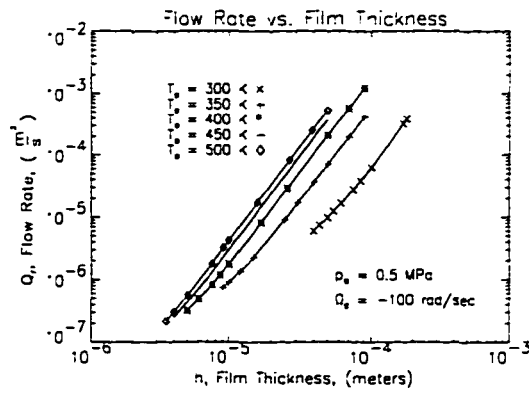


Figure 5.13: Variation of Flow Rate with Inlet Temperature

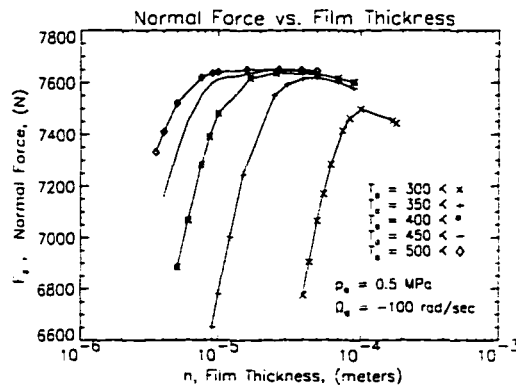


Figure 5.14: Variation of Normal Force with Inlet Temperature

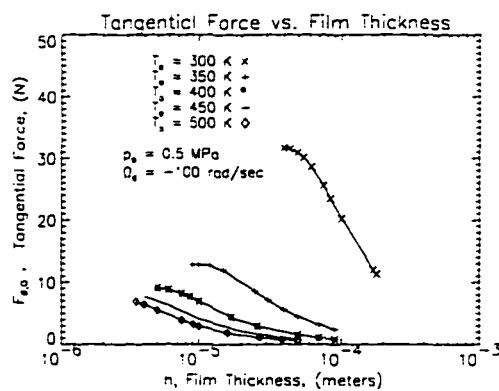


Figure 5.15: Variation of Tangential Force with Inlet Temperature



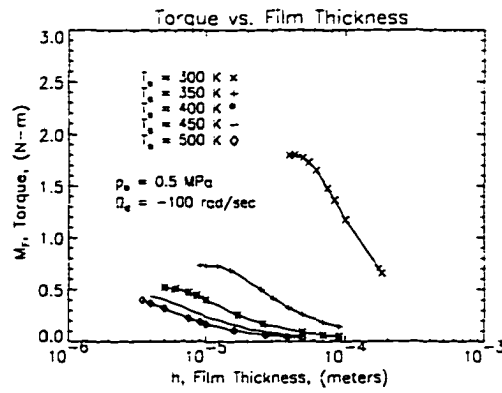


Figure 5.16: Variation of Friction Torque with Inlet Temperature

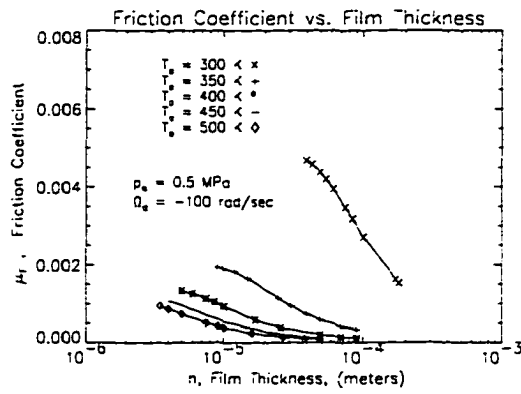


Figure 5.17: Variation of Friction Coefficient with Inlet Temperature

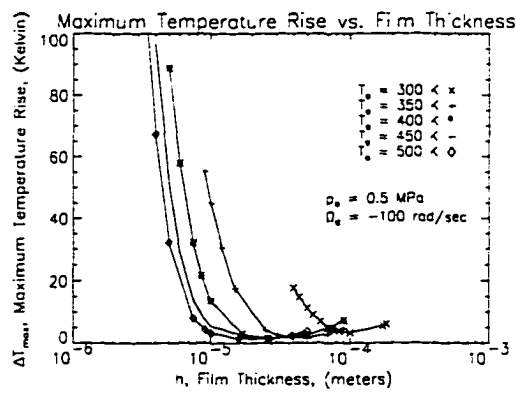


Figure 5.18: Variation of Temperature Rise with Inlet Temperature

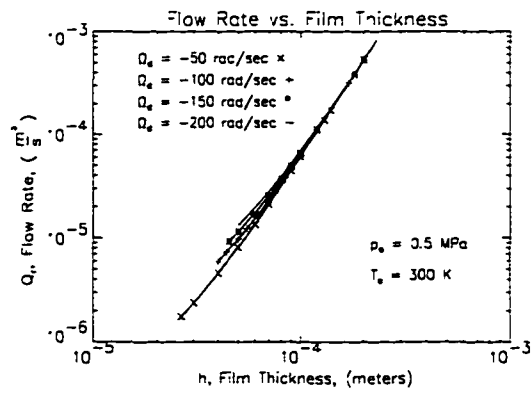


Figure 5.19: Variation of Flow Rate with Relative Angular Velocity

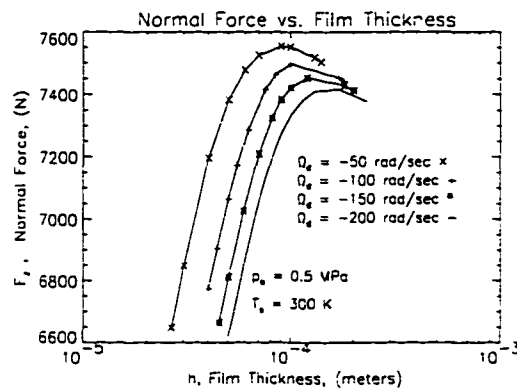


Figure 5.20: Variation of Normal Force with Relative Angular Velocity

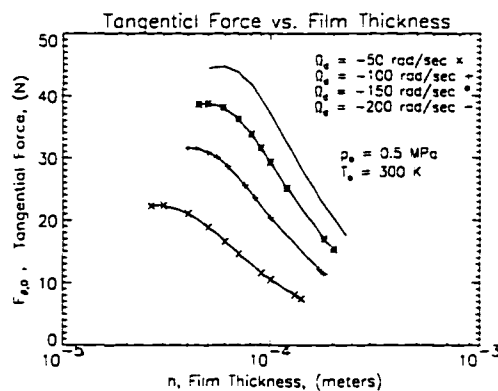


Figure 5.21: Variation of Tangential Force with Relative Angular Velocity

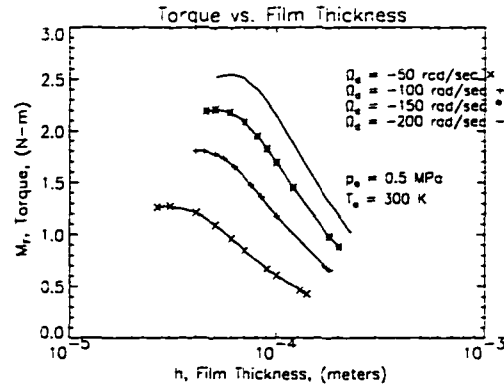


Figure 5.22: Variation of Friction Torque with Relative Angular Velocity

Results which are inconsistent with the isoviscous solution can be explained with the viscosity-temperature relation. For example, the frictional moment shown in Figure 5.22 reaches a maximum and begins to decrease with decreasing film thickness. Here, the small film thickness tends to increase the temperature, resulting in reduced viscosity, which finally leads to a decrease in frictional moment. Another example is the trend of quantities to approach a limiting curve as the film thickness becomes large. Note that the tangential force and torque approach a single curve as shown in Figures 5.9 and 5.10. Again, this can be explained by the fact that at large film thicknesses, temperature differences in the domain are negligible, resulting in a fairly constant viscosity. From Equations (5.10) and (5.11), since  $M_F$  and  $F_{\theta,0}$  are independent of  $p_o$ , a limiting curve is expected for constant viscosity solutions.

A comparison between variable viscosity and constant viscosity predictions is given in Table 5.4. Constant viscosity clutch performance parameters were based on a nodal average temperature:

$$T_{AVG} = \frac{4 \sum_{i=1,3,\dots}^{N_r} \sum_{j=2,4,\dots}^{N_\theta} \sum_{k=1,2,\dots}^{N_z} T^{[i,j,k]}}{(N_r + 1) (N_\theta - 1) N_z}$$

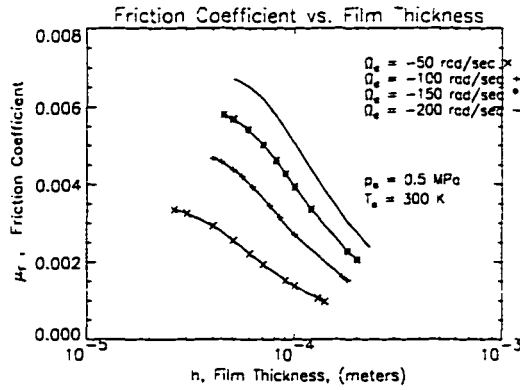


Figure 5.23: Variation of Friction Coefficient with Relative Angular Velocity

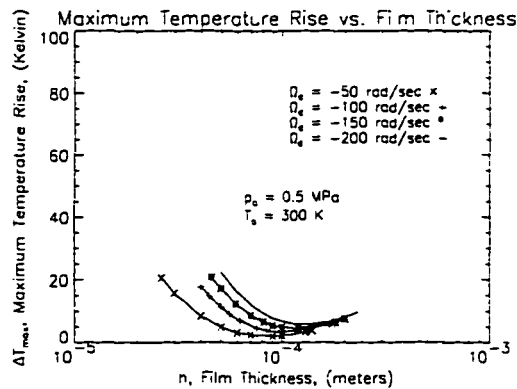


Figure 5.24: Variation of Temperature Rise with Relative Angular Velocity

To obtain the average temperature, the existing algorithm was changed merely by requiring a spatially independent viscosity. In other words, an initial guess for viscosity was made. The pressure, velocity components, and temperature were obtained as explained in Chapter 4. The average temperature was computed using the above equation. Finally, an improved guess for the viscosity, based on Equation (3.53), was made. Again, iteration was required. Thus, the constant viscosity clutch performance parameters listed in Table 5.4 are based on a reasonable approximation of the bulk viscosity of the lubricant. Five input states are given in Table 5.3. State 1 is consid-

ered  $p_o = 1.5 \text{ MPa}$ ,  $h_o = 60 \text{ }\mu\text{m}$ ,  $T_o = 400 \text{ K}$ , and  $\Omega_d = -50 \frac{\text{rad}}{\text{s}}$ . The remaining four input states show the effects of individually varying the four input parameters from state 1. Figures 5.25- 5.28 compare velocity, pressure, and temperature profiles for variable and constant viscosity using the input data for state 1.

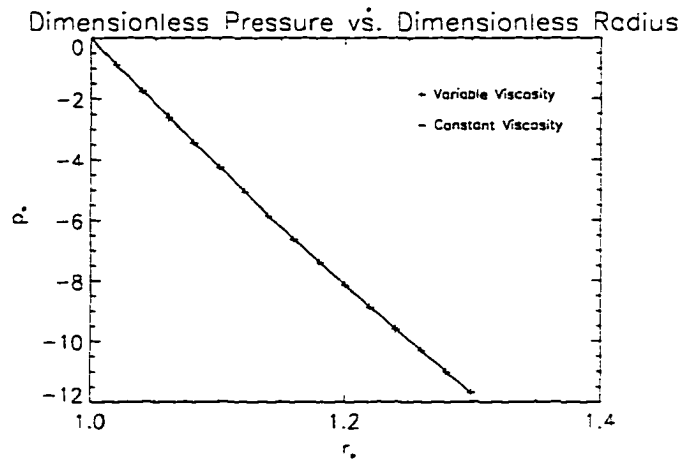


Figure 5.25: Variable and Constant Viscosity Pressure Profiles

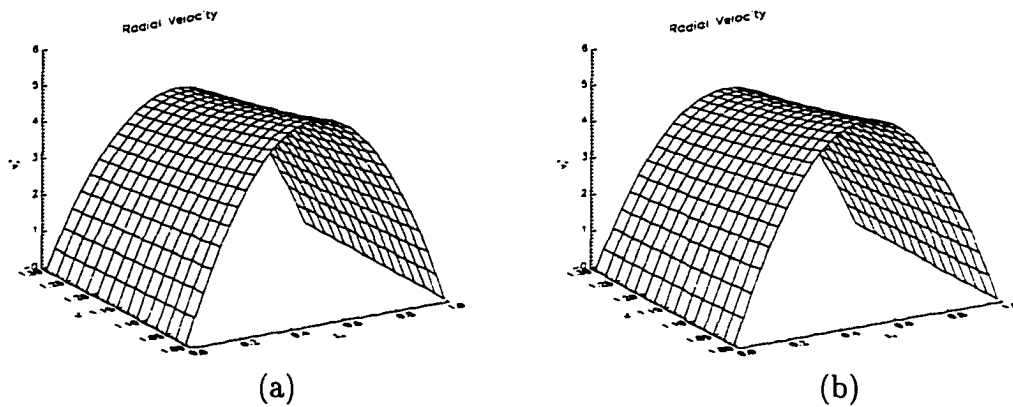


Figure 5.26: (a) Variable and (b) Constant Viscosity Radial Velocity Profiles

While the predicted values of  $\mu_F$ ,  $F_z$ ,  $M_F$ ,  $T_{max}$ , and  $Q_r$  change significantly from state 1 by individually varying the outer pressure, film thickness, inlet temperature, and relative slip speed, the variation between the constant viscosity model (CV)

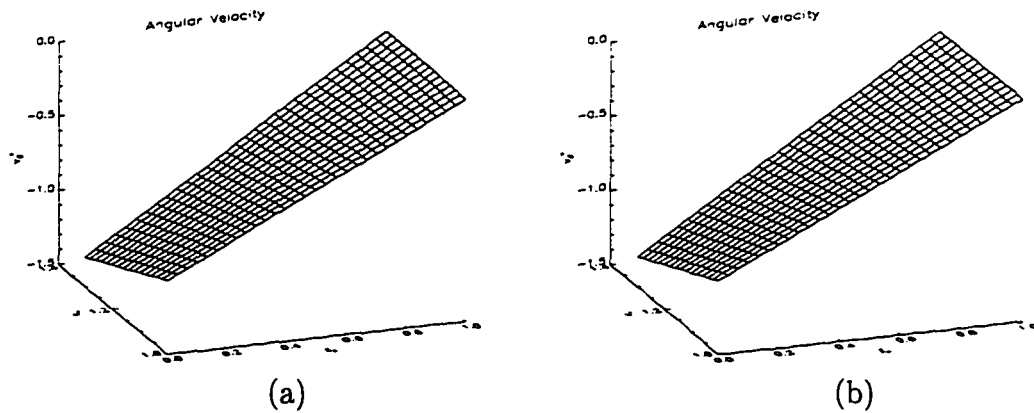


Figure 5.27: (a) Variable and (b) Constant Viscosity Angular Velocity Profiles

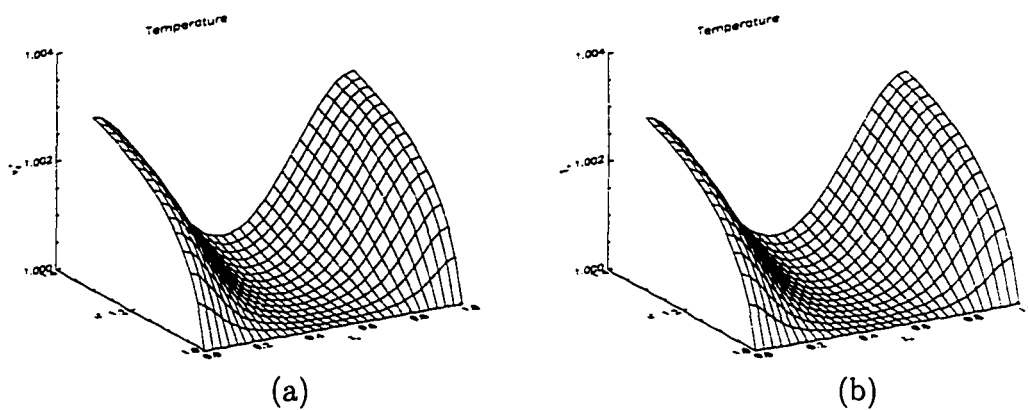


Figure 5.28: (a) Variable and (b) Constant Temperature Profiles

and the working variable viscosity model (VV) was found to be negligible. Clutch performance parameters predicted with the constant viscosity model were found to be within 1.5% of performance parameters predicted with the variable viscosity model. While only four parameters were examined, it can be concluded from the constant film case that if a rational method to choose the bulk viscosity is taken, spatial viscosity variations may be neglected. In practice, this may be difficult as one does not know *a priori* which temperature to choose.

In summary, significant variations in the clutch performance parameters were

found by varying input parameters such as the film thickness and inlet temperature. The viscosity-temperature relation was found to show significant variation from the isoviscous results given by Equations (5.8-5.12). However, when a good estimation is made for the bulk viscosity of the lubricant, (such as the viscosity evaluated at the average temperature) the constant viscosity model produces similar results.

### 5.3 Groove Studies

In this section, several studies involving grooves in friction plates are presented. As mentioned previously, grooves are present in friction plates to enhance lubricant cooling. In the absence of grooves, the model reduces to a parallel plate hydrodynamic thrust bearing. As a consequence, no load carrying capacity may be generated except by hydrostatic means. When grooves are present, the model may predict a *hydrodynamic* load carrying capacity. Again, our purpose for allowing for arbitrary geometry is to allow for any groove pattern. However, the results presented in this section use the following dimensionless groove shape:

$$h_* = \begin{cases} 1 & ; 0 \leq \theta_* < \frac{\theta_o}{2} (1 - \chi_1) \\ 1 + \frac{h_g^*}{\chi_1 - \chi_2} \left[ 2 \frac{\theta_*}{\theta_o} - 1 + \chi_1 \right] & ; \frac{\theta_o}{2} (1 - \chi_1) \leq \theta_* < \frac{\theta_o}{2} (1 - \chi_2) \\ 1 + h_g^* & ; \frac{\theta_o}{2} (1 - \chi_2) \leq \theta_* < \frac{\theta_o}{2} (1 + \chi_2) \\ 1 - \frac{h_g^*}{\chi_1 - \chi_2} \left[ 2 \frac{\theta_*}{\theta_o} - 1 - \chi_1 \right] & ; \frac{\theta_o}{2} (1 + \chi_2) \leq \theta_* < \frac{\theta_o}{2} (1 + \chi_1) \\ 1 & ; \frac{\theta_o}{2} (1 + \chi_1) \leq \theta_* < \theta_o \end{cases} \quad (5.13)$$

which is illustrated in Figure 5.29. In Equation (5.13),  $h_g^* = \frac{h_g}{h_o}$  is the ratio of groove depth to minimum film thickness, and  $\chi_1$  and  $\chi_2$  are referred to as the major and

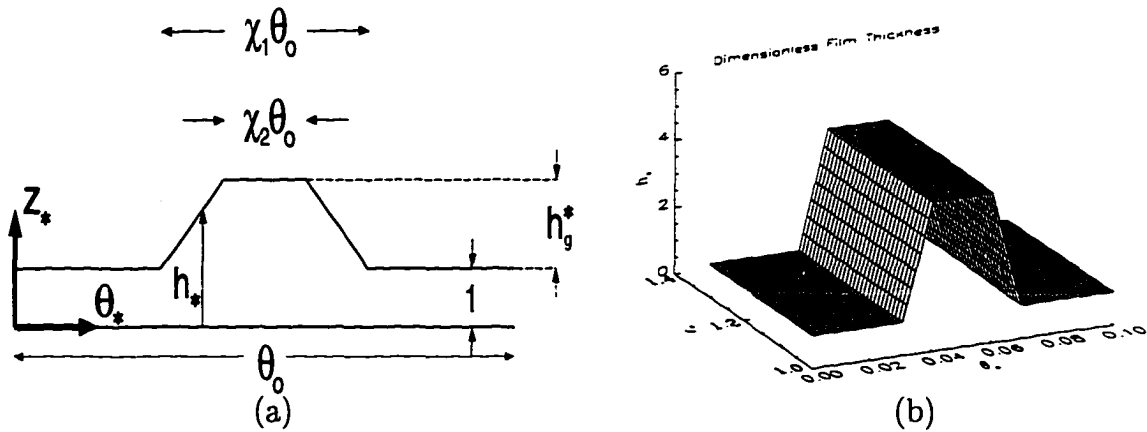


Figure 5.29: (a) Film Thickness Schematic in  $\theta_* - z_*$  plane and (b) Film Thickness with  $\chi_1 = 0.4$ ,  $\chi_2 = 0.2$ ,  $R_* = 1.3$ ,  $\theta_o = 0.1 \text{ rad}$ ,  $h_g^* = 3.5$ .

minor groove fractions, respectively. Finally, results presented in this section are divided into two parts: cavitation and non-cavitation studies. The results presented in the cavitation part are an isolated set in that negative pressures are predicted using the existing governing equations. Gumbel's [7, 18, 19, 22] approximation is employed to predict a load carrying capacity for this section. In the non-cavitation part, and throughout the remainder of this dissertation, negative pressures are not predicted.

### 5.3.1 Cavitation Studies

Cavitation refers to the formation of partial gas pockets in a liquid. This phenomenon occurs when the liquid pressure falls below the vapor pressure. In an ideal incompressible fluid, Batchelor [4] notes that it is possible to predict thermodynamically inadmissible negative pressures. In reality, the assumption of incompressibility is certainly questionable at these low pressures.

This topic is relevant under groove studies. Birkhoff and Hays [7] cite specific lemmas regarding increasing and decreasing pressures in converging and diverging



domains. In particular, when the local film thickness is less than a specific value, the pressure will necessarily increase with further reduction in film size. Above this specific height, which is defined by the geometry and operating conditions of the lubrication problem of interest, the pressure will decrease. For the domain defined by Equation (5.13), the pressure will necessarily decrease in the diverging section and increase in the converging section.

We adopt Gmbel's assumption which states that the vapor pressure is zero and negative pressures are neglected. Here, the difference between the vapor pressure and zero is small compared to positive pressures predicted in the lubricant. Physically, predicting negative pressures infers that a cavity is formed, the no-slip conditions and the incompressible continuity equation are inappropriate next to the cavity, and the posed model breaks down. Using the posed model with the assumption of neglecting negative pressures is a first approximation. Mathematically, Gmbel's assumption is to ignore negative pressures if the following inequality holds:

$$p_* < -\frac{1}{S}, \quad (5.14)$$

which may be shown using Equations (3.25) and (3.73).

For this isolated set of results, we are only concerned with the lubricant load carrying capacity,  $F_z^*$ . The numerical analysis is performed exactly as before. However, in computing the performance parameters, negative pressures are simply ignored. Numerical results are presented for variable groove depth,  $h_g^*$ , and Sommerfeld number,  $S$ . Unless otherwise stated, relevant dimensionless parameters which were held fixed are listed in Table 5.5. Isoviscous results,  $\mu_* = 1$ , are presented in Figures 5.30-5.33.

while variable viscosity results using the viscosity-temperature relation with SAE 10 oil are shown in Figure 5.34.

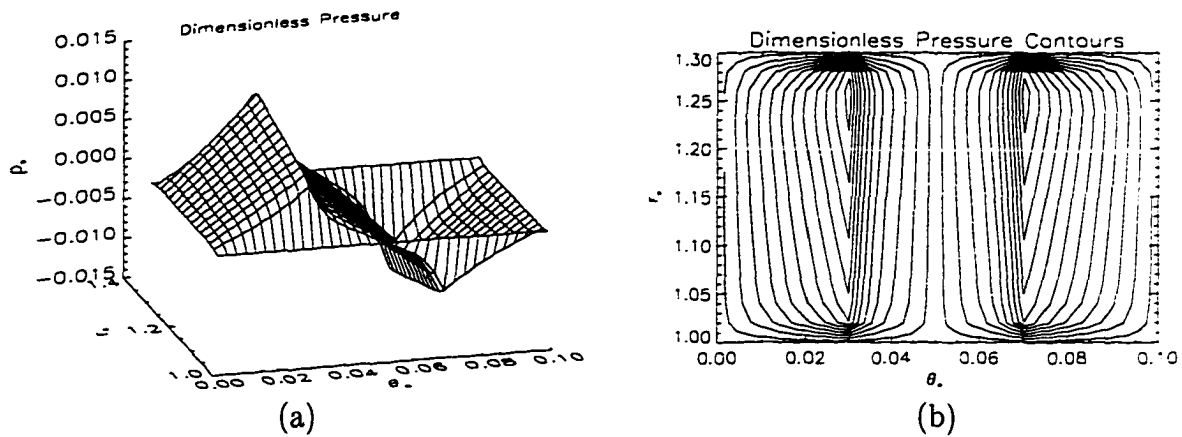


Figure 5.30: (a) Typical Pressure Distribution and (b) Pressure Contours. (Using  $S = 968.72$  and  $h_g^* = 3.5$ .)

Figure 5.30(a) shows a typical pressure distribution predicted by the numerical model using  $S = 968.72$  and  $h_g^* = 3.5$ . Figure 5.30(b) shows the same set of data displayed as a contour plot. Figure 5.31 shows the zones where cavitation will and will not occur. Note in Figure 5.31(a), for  $h_g^* \rightarrow 0$  cavitation will not occur. In other words, without grooves cavitation will not occur. In Figure 5.31(b) the boundary between regimes reaches a maximum and then tends toward zero as  $h_g \rightarrow \infty$ . For large Sommerfeld number, cavitation occurs. These results are consistent with the two-dimensional Rayleigh thrust bearing theory [18, 22]. Figure 5.32 may be used to explain Figure 5.31. In this figure,  $S = 200$ . Assuming symmetry as shown in Figure 5.30, the maximum and minimum dimensionless pressures have the same magnitude. Therefore, the groove depth which predicts the largest maximum pressure should correspond to the position where cavitation is likeliest to occur in Figure 5.31. Further

in Figure 5.32, as the groove depth goes to zero, the maximum dimensional pressure approaches the inlet radial pressure. This corresponds to  $p_* = 0$  in dimensionless terms. The minimum pressure is found at the radial outlet,  $p_* = p_o^*$ . On the other hand, as the groove depth increases, cavitation occurs when the maximum pressure is larger than  $p_* = \frac{1}{S} = 0.005$ . The minimum value for maximum pressure occurs in the zone where cavitation does not occur. As the groove depth gets large, the maximum pressure value remains finite resulting in an expanded zone of cavitation to include  $S = 200$  as  $h_g^* \rightarrow \infty$ . Figure 5.33 shows the normal load as a function of Sommerfeld number and groove depth. The trends indicate that using an ideal groove depth with a large Sommerfeld number will increase the load carrying capacity. The effect of the viscosity-temperature relation is shown in Figure 5.34. Here,  $S = 33.9$  and  $p_o^* = -0.02949$ . The constant viscosity case uses the dimensionless viscosity based on the inlet temperature throughout the domain. In other words,  $\mu_* = 1$  for the constant viscosity case. Note that the employment of the viscosity-temperature relation tends to decrease the load carrying capacity. This is consistent with previous results. That is, while no physical wedge was present for the constant film case, normal forces computed for variable viscosity were found to be less than constant viscosity predictions. This can be verified using Equation (5.9), Figure 5.14, and Table 5.2.

### 5.3.2 Non-Cavitation Studies

In this section, dimensionless results using variable and constant viscosity, grooving and no grooving are presented. Here the effect of varying the groove depth,  $h_g^*$ , on

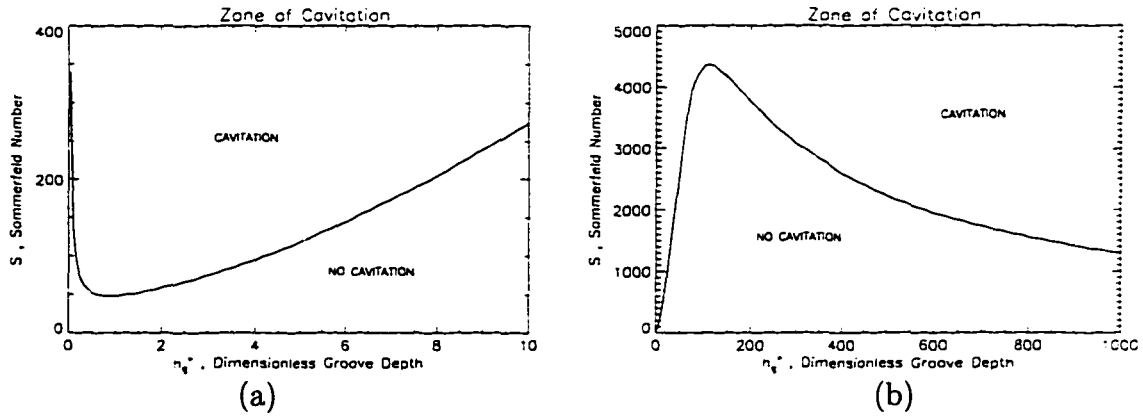


Figure 5.31: Zones of Cavitation and No Cavitation

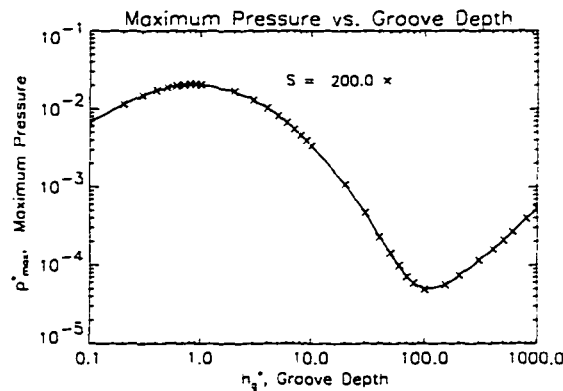


Figure 5.32: Maximum Pressure vs. Groove Depth

eight dimensionless clutch performance parameters is examined. These parameters are (1) the flow rate,  $Q_r^*$ , (2) the normal load,  $F_z^*$ , (3) the tangential force on the separator plate due to viscous shearing,  $F_{\theta,0}^*$ , (4) the tangential force on the friction plate due to viscous shearing,  $F_{\theta,h}^*$ , (5) the tangential force on the friction plate due to pressure,  $F_{p,h}^*$ , (6) the moment,  $M_F^*$ , (7) the friction coefficient,  $\mu_F$ , and (8) the maximum temperature  $T_{max}^*$ . All results predict positive pressures throughout the domain,  $p_* > -\frac{1}{5}$ . Relevant dimensionless parameters which were held fixed are listed in Table 5.6.

Results for this section are shown in Table 5.7. Here, the results for no grooves,

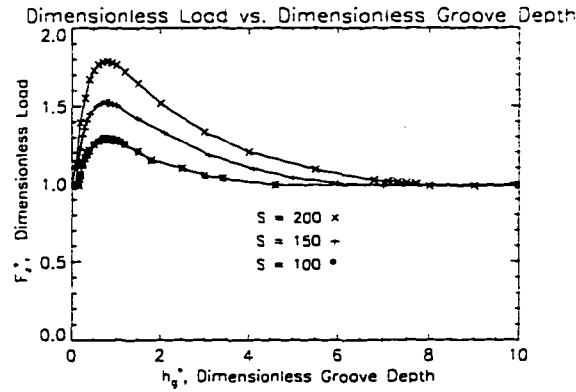


Figure 5.33: Normal Load vs. Groove Depth and Sommerfeld Number

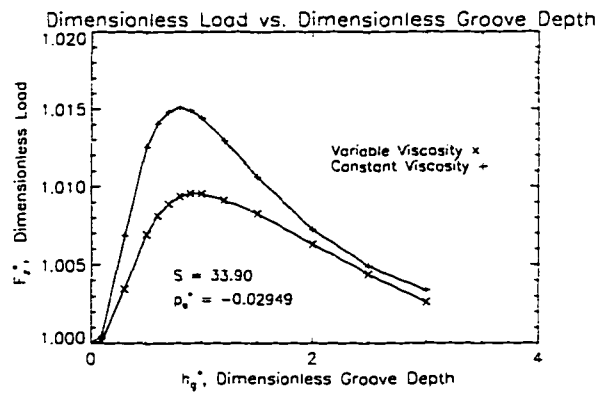


Figure 5.34: Normal Load vs. Groove Depth using Variable and Constant Viscosity  $h_g^* = 0$ , are compared to varying groove depth,  $h_g^* = 0.5$ ,  $h_g^* = 1.0$ , and  $h_g^* = 2.0$ . Further, the variable viscosity model is compared to the constant viscosity model. The acronyms, VV and CV, used in Table 5.7 denote variable and constant viscosity, respectively. Note that the flow rate increases as the groove depth increases. This is expected because a constant pressure difference,  $p_o^*$ , is maintained. The normal force is constant for the CV case and increases for the VV case for increasing  $h_g^*$ . This latter trend was observed for small film thicknesses as shown in Figures 5.8, 5.14, and 5.20. It is expected that the normal force will remain constant for the CV case because of the symmetry in pressure shown in the previous section. The tangential

forces due to viscous shearing decrease in magnitude as the groove depth increases. However, the tangential force due to pressure is zero for constant groove depth and increases as the groove depth increases. This is consistent with Equation (3.79). Note that in all cases,  $F_{\theta,0}^* + F_{\theta,h}^* + F_{p,h}^* = 0$  as mentioned in Chapter 3. This relation, which states that the sum of the tangential forces is zero, is in keeping with Newton's laws since acceleration terms in the momentum equations have been neglected. The maximum temperature decreases for increasing groove depth because the dominant heating term in the energy equation is  $\mu \frac{\partial v_{\theta}}{\partial z}$ , and this term decreases for increasing film thickness.

Figure 5.35 shows velocity vectors at the average radius,  $r_* = \frac{1+R_*}{2}$ , for the case where  $h_g^* = 0.5$ . Here, the velocity field is essentially a Couette flow in the  $\theta$ -direction.

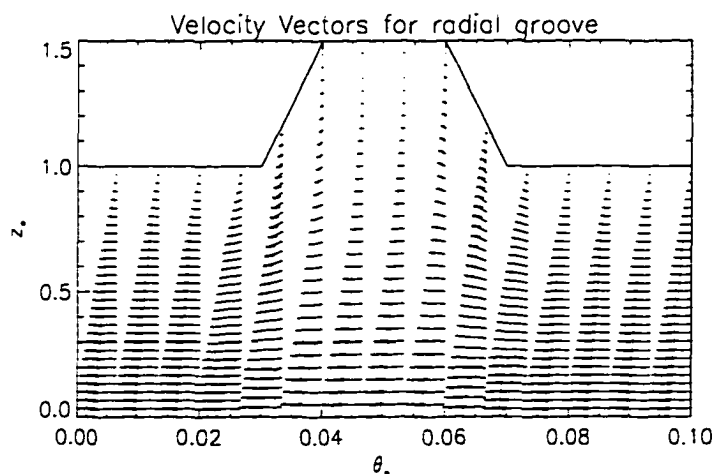


Figure 5.35: Velocity Vectors at Average Clutch Radius

Note that the axial velocity is significant on the physical wedges.

## 5.4 Multiple Disk Solutions

In this section, dimensional results for a conjugate lubrication, heat-transfer prob-

lem are given. Here, an assembly of five clutch plates is examined as shown in Figure 5.36(a). Temperature profiles throughout the assembly are predicted.

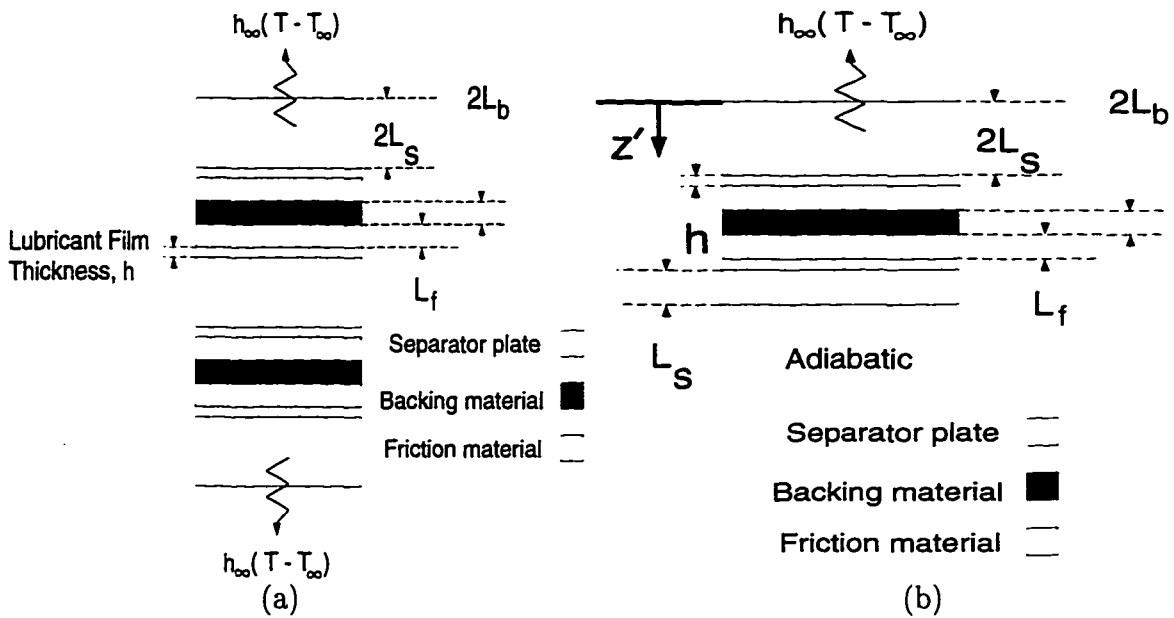


Figure 5.36: Multiple Disk Clutch Conjugate Model Schematic

It is assumed that the ambient conditions, namely the convection coefficient,  $h_\infty$ , and ambient temperature,  $T_\infty$ , are constant. Further, the film thickness between each plate is identical. These assumptions imply that axial symmetry may be taken about  $z' = 3L_s + 2L_f + 2h_o + 2L_b$ , as indicated in Figure 5.36(b). The thermal energy equation for each material region is  $\frac{\partial^2 T}{\partial z'^2} = 0$ , as indicated by Equations (3.50-3.52) and Figure 5.36(b). The boundary conditions on the temperature field are as follows:

$$\begin{aligned}
\text{on } z' = 0 : & \quad k_s \frac{\partial T}{\partial z'} = h_\infty (T - T_\infty), \\
\text{on } z' = L_1 : & \quad T \Big|_{L_1^-} = T \Big|_{L_1^+}, \quad k_s \frac{\partial T}{\partial z'} \Big|_{L_1^-} = k \frac{\partial T}{\partial z'} \Big|_{L_1^+}, \\
\text{on } z' = L_1 + h : & \quad T \Big|_{(L_1+h)^-} = T \Big|_{(L_1+h)^+}, \quad k \frac{\partial T}{\partial z'} \Big|_{(L_1+h)^-} = k_f \frac{\partial T}{\partial z'} \Big|_{(L_1+h)^+}, \\
\text{on } z' = L_2 : & \quad T \Big|_{L_2^-} = T \Big|_{L_2^+}, \quad k_f \frac{\partial T}{\partial z'} \Big|_{L_2^-} = k_b \frac{\partial T}{\partial z'} \Big|_{L_2^+}, \\
\text{on } z' = L_3 : & \quad T \Big|_{L_3^-} = T \Big|_{L_3^+}, \quad k_b \frac{\partial T}{\partial z'} \Big|_{L_3^-} = k_f \frac{\partial T}{\partial z'} \Big|_{L_3^+}, \\
\text{on } z' = L_4 - h : & \quad T \Big|_{(L_4-h)^-} = T \Big|_{(L_4-h)^+}, \quad k_f \frac{\partial T}{\partial z'} \Big|_{(L_4-h)^-} = k \frac{\partial T}{\partial z'} \Big|_{(L_4-h)^+}, \\
\text{on } z' = L_4 : & \quad T \Big|_{L_4^-} = T \Big|_{L_4^+}, \quad k \frac{\partial T}{\partial z'} \Big|_{L_4^-} = k_s \frac{\partial T}{\partial z'} \Big|_{L_4^+}, \\
\text{on } z' = L_5 : & \quad \frac{\partial T}{\partial z'} = 0,
\end{aligned} \tag{5.15}$$

where,

$$\begin{aligned}
L_1 &= 2L_s, & L_2 &= 2L_s + h_o + L_f, \\
L_3 &= 2L_s + h_o + L_f + 2L_b, & L_4 &= 2L_s + 2h_o + 2L_f + 2L_b, \\
L_5 &= 3L_s + 2h_o + 2L_f + 2L_b.
\end{aligned}$$

In the above equation, it has been assumed that  $L_f$  is the maximum axial length of the friction material as shown in Figure 3.2.

Using the fact that the temperature distributions are linear in the axial direction, the temperature distributions in the solid material regions may be determined in terms of the lubricant temperature and its derivative on  $z' = L_1$ ,  $z' = L_1 + h$ ,  $z' = L_4 - h$  and  $z' = L_4$ . In other words, we have,

$$T = C_1 z' + C_2, \tag{5.16}$$



where,

$$C_1 = \begin{cases} \frac{k}{k_s} \frac{\partial T}{\partial z'} \Big|_{z'=L_1} & ; 0 \leq z' \leq L_1 \\ \frac{k}{k_f} \frac{\partial T}{\partial z'} \Big|_{z'=L_1+h} & ; L_1 + h \leq z' \leq L_2 \\ \frac{k}{k_b} \frac{\partial T}{\partial z'} \Big|_{z'=L_1+h} & ; L_2 \leq z' \leq L_3 \\ \frac{k}{k_f} \frac{\partial T}{\partial z'} \Big|_{z'=L_4-h} & ; L_3 \leq z' \leq L_4 - h \\ 0 & ; L_4 \leq z' \leq L_5 \end{cases} ,$$

$$C_2 = \begin{cases} T \Big|_{z'=L_1} - \frac{k}{k_s} \frac{\partial T}{\partial z'} \Big|_{z'=L_1} L_1 & ; 0 \leq z' \leq L_1 \\ T \Big|_{z'=L_1+h} - \frac{k}{k_f} \frac{\partial T}{\partial z'} \Big|_{z'=L_1+h} (L_1 + h) & ; L_1 + h \leq z' \leq L_2 \\ T \Big|_{z'=L_1+h} - \frac{k}{k_b} \frac{\partial T}{\partial z'} \Big|_{z'=L_1+h} [L_2 - \frac{k_b}{k_f} (L_2 - L_1 - h)] & ; L_2 \leq z' \leq L_3 \\ T \Big|_{z'=L_4-h} - \frac{k}{k_f} \frac{\partial T}{\partial z'} \Big|_{z'=L_4-h} [L_4 - h] & ; L_3 \leq z' \leq L_4 - h \\ T \Big|_{z'=L_4} & ; L_4 \leq z' \leq L_5 \end{cases} .$$

These ten expressions for  $C_1$  and  $C_2$  were found from the fourteen conditions in Equation (5.15). In addition, it may be shown that

$$\begin{aligned} k \frac{\partial T}{\partial z'} \Big|_{z'=L_1} &= \frac{h_\infty \left( T \Big|_{z'=L_1} - T_\infty \right)}{\frac{2h_\infty L_s}{k_s} + 1}, \\ k \frac{\partial T}{\partial z'} \Big|_{z'=L_1+h} &= \frac{T \Big|_{z'=L_4-h} - T \Big|_{z'=L_1+h}}{\frac{2L_f + 2h_o - 2h}{k_f} + \frac{2L_h}{k_b}}, \\ \frac{\partial T}{\partial z'} \Big|_{z'=L_4-h} &= \frac{\partial T}{\partial z'} \Big|_{z'=L_1+h}, \quad \frac{\partial T}{\partial z'} \Big|_{z'=L_4} = 0. \end{aligned} \tag{5.17}$$

Equation (5.17) is used to solve two coupled lubrication problems. The boundary conditions which replace the adiabatic conditions given in dimensionless form in Equation

(3.60) for the first lubricant film are

$$k \frac{\partial T}{\partial z} \Big|_{z=0}^{n=1} = \frac{h_{\infty} \left( T \Big|_{z=0}^{n=1} - T_{\infty} \right)}{\frac{2h_{\infty}L_s}{k_s} + 1}, \quad k \frac{\partial T}{\partial z} \Big|_{z=h}^{n=1} = \frac{T \Big|_{z=h}^{n=2} - T \Big|_{z=h}^{n=1}}{\frac{2L_f + 2h_o - 2h}{k_f} + \frac{2L_h}{k_b}}, \quad (5.18)$$

and for the second lubricant film are

$$\frac{\partial T}{\partial z} \Big|_{z=h}^{n=2} = -\frac{\partial T}{\partial z} \Big|_{z=h}^{n=1}, \quad \frac{\partial T}{\partial z} \Big|_{z=0}^{n=2} = 0. \quad (5.19)$$

Here,  $n = 1$  denotes the lubrication problem with axial domain  $L_1 \leq z' \leq L_1 + h$ , and  $n = 2$  denotes the lubrication problem with axial domain  $L_4 - h \leq z' \leq L_4$ . For  $n = 1$ ,  $z = z' - L_1$ , and for  $n = 2$ ,  $z = L_4 - z'$ . Note that Equations (5.18) and (5.19) use a consistent notation convention with the axial coordinate,  $z$ , described in chapter 3. That is, in both lubrication problems we have  $z = 0$  on the separator plate surface, and  $z = h$  on the friction plate surface.

In order to solve this problem, iteration was employed. An initial guess was made for the second,  $n = 2$ , lubricant temperature field. Using this guess, the first,  $n = 1$ , lubrication problem was solved as usual substituting Equation (5.18) for Equation (3.60). Then, the second lubrication problem was solved by substituting Equation (5.19) for Equation (3.60). This procedure was continued until the difference between temperature fields between iteration cycles was negligible.

Upon solving the coupled lubrication problems, the moment delivered to the clutch may be found. Referring to Figure 5.36(a) and observing symmetry, the net moment,  $\mathcal{M}_F$ , delivered to the output side of the clutch is the sum of the moments at each interface:

$$\mathcal{M}_F = 2M_F^{n=1} + 2M_F^{n=2}. \quad (5.20)$$

The individual moments,  $\overline{M_F^{n=1}}$  and  $M_F^{n=2}$ , are calculated using Equation (3.84).

An analytical solution was obtained using a zero radial pressure difference,  $p_o = p_i$ , a constant viscosity,  $\mu = \mu_o$ , and a constant film thickness,  $h = h_o$ . Under such conditions, the hydrodynamic variables for the lubricant are

$$v_r = v_z = 0, \quad v_\theta = \Omega_d r \left(1 - \frac{z}{h_o}\right), \quad p = p_i. \quad (5.21)$$

Equation (5.21) applies to both lubricant films. The temperature field for the assembly shown in Figure 5.36(b) is as follows:

$$T - T_\infty = \begin{cases} \frac{2\mu_o\Omega_d^2r^2}{h_o} \left[ \frac{z'}{k_s} + \frac{1}{h_\infty} \right] & ; 0 \leq z' \leq L_1 \\ \frac{\mu_o\Omega_d^2r^2}{h_o} \left[ -\frac{(z'-L_1)^2}{2kh_o} + \frac{2(z'-L_1)}{k} + \frac{2L_1}{k_s} + \frac{2}{h_\infty} \right] & ; L_1 \leq z' \leq L_1 + h_o \\ \frac{\mu_o\Omega_d^2r^2}{h_o} \left[ \frac{z'}{k_f} + \frac{3h_o}{2k} + \frac{2L_1}{k_s} + \frac{2}{h_\infty} - \frac{L_1}{k_f} - \frac{h_o}{k_f} \right] & ; L_1 + h_o \leq z' \leq L_2 \\ \frac{\mu_o\Omega_d^2r^2}{h_o} \left[ \frac{z'}{k_b} + \frac{3h_o}{2k} + \frac{2L_1}{k_s} + \frac{2}{h_\infty} + \frac{L_f}{k_f} - \frac{L_2}{k_b} \right] & ; L_2 \leq z' \leq L_3 \\ \frac{\mu_o\Omega_d^2r^2}{h_o} \left[ \frac{z'}{k_f} + \frac{3h_o}{2k} + \frac{2L_1}{k_s} + \frac{2}{h_\infty} - \frac{L_3}{k_f} + \frac{L_f}{k_f} + \frac{2L_b}{k_b} \right] & ; L_3 \leq z' \leq L_4 - h_o \\ \frac{\mu_o\Omega_d^2r^2}{h_o} \left[ -\frac{(L_4-z')^2}{2kh_o} + \frac{2h_o}{k} + \frac{2L_b}{k_b} + \frac{2L_1}{k_s} + \frac{2}{h_\infty} + \frac{2L_f}{k_f} \right] & ; L_4 - h_o \leq z' \leq L_4 \\ \frac{\mu_o\Omega_d^2r^2}{h_o} \left[ \frac{2L_b}{k_b} + \frac{2h_o}{k} + \frac{2}{h_\infty} + \frac{2L_1}{k_s} + \frac{2L_f}{k_f} \right] & ; L_4 \leq z' \leq L_5 \end{cases} \quad (5.22)$$

For this solution, the temperature condition at  $r = R_i$ , Equation (3.20), is relaxed.

This condition does not effect the temperature field because the energy equation for this case reduces to the following expression:

$$\frac{\partial^2 T}{\partial z^2} = -\frac{\mu_o}{k} \left( \frac{\partial v_\theta}{\partial z} \right)^2.$$

In other words, since the convection terms vanish identically, information at the inner radius is not convected to the rest of the domain.

Relevant dimensional parameters which were held constant for the following results are listed in Table 5.8. Variable viscosity results are presented using the parameters associated with SAE 10 oil. The inlet pressure and groove depth were also varied in this study. The film shape was given by Equation (5.13). In dimensional form, this equation is as follows:

$$h = \begin{cases} h_o & ; 0 \leq \theta < \frac{\theta_o}{2} (1 - \chi_1) \\ h_o + \frac{h_g}{\chi_1 - \chi_2} \left[ 2 \frac{\theta}{\theta_o} - 1 + \chi_1 \right] & ; \frac{\theta_o}{2} (1 - \chi_1) \leq \theta < \frac{\theta_o}{2} (1 - \chi_2) \\ h_o + h_g & ; \frac{\theta_o}{2} (1 - \chi_2) \leq \theta < \frac{\theta_o}{2} (1 + \chi_2) \\ h_o - \frac{h_g}{\chi_1 - \chi_2} \left[ 2 \frac{\theta}{\theta_o} - 1 - \chi_1 \right] & ; \frac{\theta_o}{2} (1 + \chi_2) \leq \theta < \frac{\theta_o}{2} (1 + \chi_1) \\ h_o & ; \frac{\theta_o}{2} (1 + \chi_1) \leq \theta < \theta_o \end{cases} \quad (5.23)$$

Dimensional temperature profiles at the outer radius,  $r = R_o$ , are shown in Figures 5.37-5.41. Figure 5.37 shows a comparison between the analytical and numerical solutions. Here, the viscosity is constant, the pressure difference is zero,  $\frac{p_i}{p_o} = 1$ , and the film thickness is constant,  $\frac{h_g}{h_o} = 0$ . Figure 5.38 shows the effect of increasing the inlet lubricant pressure,  $\frac{p_i}{p_o} = 2$ , while holding all other parameters fixed as in Figure 5.37. Note that increasing the radial inlet pressure increases the flow rate resulting in significant convection to cool the clutch. Figure 5.39 illustrates the effect of using grooves,  $\frac{h_g}{h_o} = 0.5$ . Compared to Figure 5.38, the temperature distribution is lower. The temperature distribution resulting from the assumptions of constant film thickness and variable viscosity is shown in in Figure 5.40. Compared with Figure 5.38, the temperature distribution is slightly less with variable viscosity. The temperature distribution resulting from the assumptions of variable viscosity with

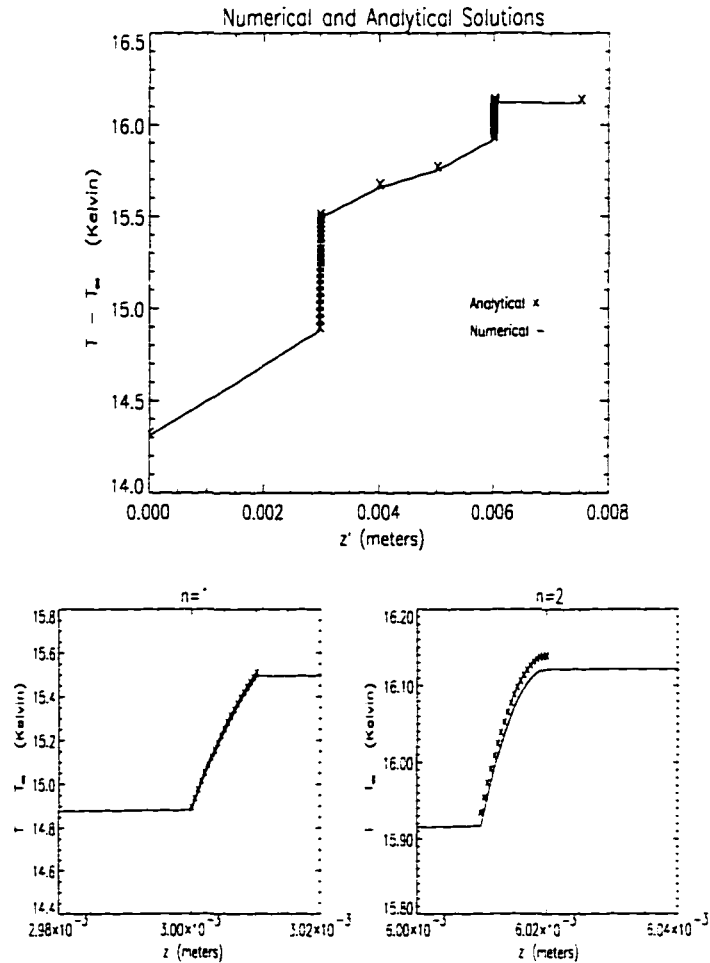


Figure 5.37: Comparison Between Numerical and Analytical Assembly Temperature Distributions at  $r = R_o$  using constant viscosity,  $\frac{p_i}{p_o} = 1$ , and  $\frac{h_2}{h_o} = 0$ .

grooves is shown in Figure 5.41. Here the temperature distribution is the lowest of the results presented.

A summary of the clutch performance is given in Table 5.9. It is noted that while grooving serves to cool the clutch, the frictional moment is reduced. The model assumption of variable viscosity will give more realistic performance predictions. However, at high temperatures, such as in this scenario ( $T_\infty = T_o = 450K$ ), the viscosity-temperature relation is not very sensitive compared to low temperature

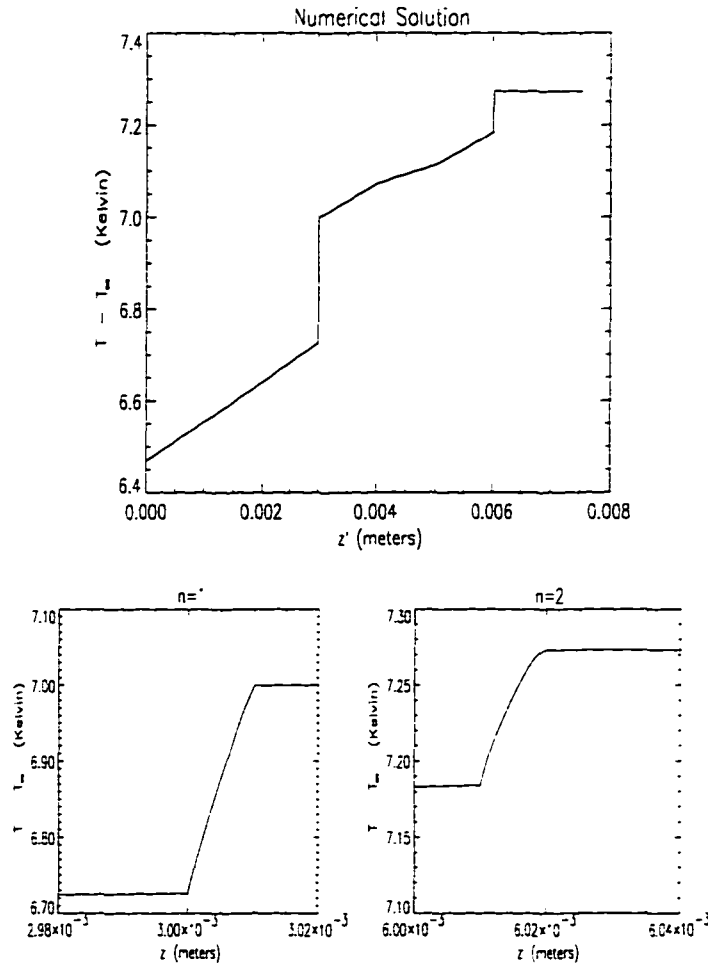


Figure 5.38: Numerical Assembly Temperature Distributions at  $r = R_o$  with constant viscosity,  $\frac{\rho_i}{\rho_o} = 2$ , and  $\frac{h_g}{h_o} = 0$ .

scenarios. In other words,  $\left. \frac{d\mu}{dT} \right|_{\text{high } T} < \left. \frac{d\mu}{dT} \right|_{\text{low } T}$ . This results in approximately the same temperature predictions for equal film shapes as shown in Table 5.9.

In summary, temperature distributions were obtained for a symmetric clutch pack with five disks. It was assumed that the minimum film thickness,  $h_o$ , was constant for all interfaces. The extension of this methodology to incorporate more disks, with or without the assumption of symmetry, is straightforward. One would solve the lubrication problem, as developed here, for each lubricant interface between clutch

plates. The appropriate heat flux and temperature continuity conditions should be used to replace the adiabatic conditions given by Equation (3.60).

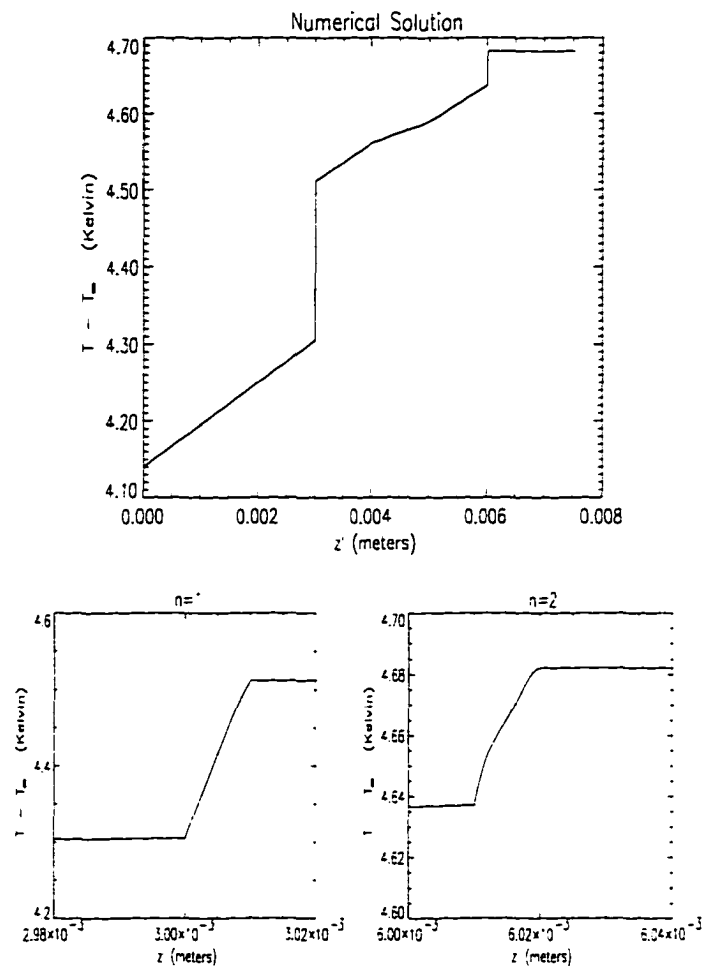


Figure 5.39: Numerical Assembly Temperature Distributions at  $r = R_o$  and  $\theta = 0$  with constant viscosity,  $\frac{\rho_i}{\rho_o} = 2$ , and  $\frac{h_g}{h_o} = 0.5$ .

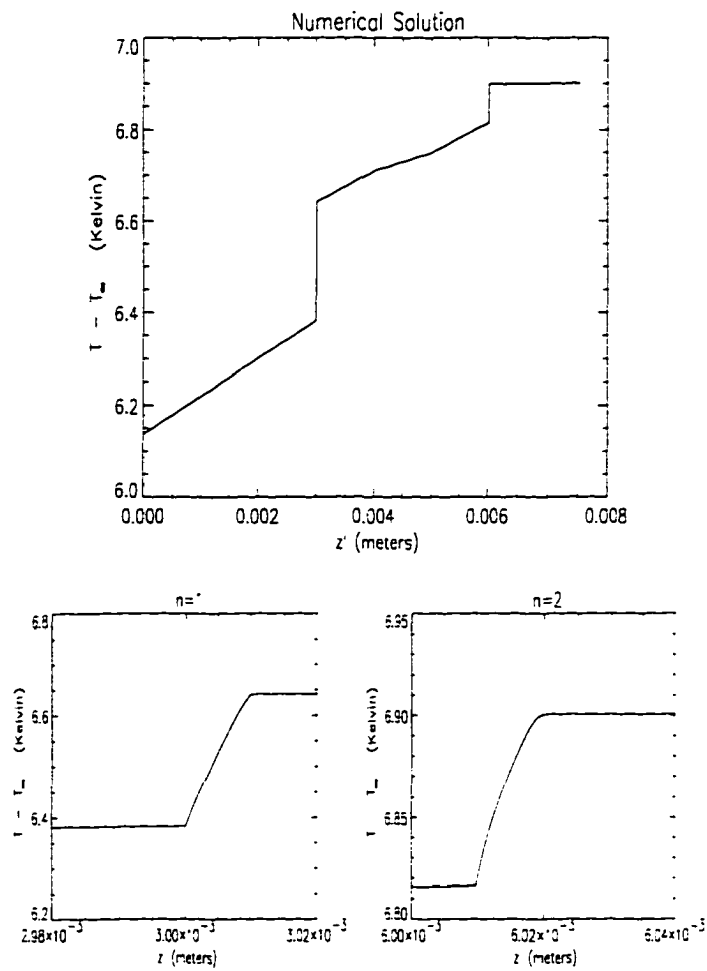


Figure 5.40: Numerical Assembly Temperature Distributions at  $r = R_o$  with variable viscosity,  $\frac{\rho_i}{\rho_o} = 2$ , and  $\frac{h_q}{h_o} = 0$ .



$p_o$	$h_o$	$T_o$	$\Omega_d$		$\mu_F$	$F_z$	$M_F$	$T_{max}$	$Q_r$
$\times 10^{-6}$	$\times 10^6$	$\times 10^2$			$\times 10^5$	$\times 10^{-4}$	$\times 10^2$		$\times 10^4$
(Pa)	(m)	(K)	( $\frac{rad}{s}$ )			(N)	(N - m)	(K)	( $\frac{m^3}{s}$ )
1.5	60	400	-50	VV	6.028	1.059	3.713	401.3	1.768
				CV	6.025	1.060	3.715	401.3	1.762
0.15	60	400	-50	VV	9.601	0.6576	3.670	405.5	4.243
				CV	9.529	0.6625	3.671	404.5	4.191
1.5	6	400	-50	VV	48.22	1.039	28.85	436.6	0.002179
				CV	48.05	1.060	29.63	437.1	0.002210
1.5	60	300	-50	VV	153.2	1.048	92.83	304.3	0.06909
				CV	153.2	1.060	94.44	304.4	0.06932
1.5	60	400	-150	VV	18.08	1.060	11.14	401.3	1.769
				CV	18.07	1.060	11.14	401.3	1.763

Table 5.4: COMPARISON BETWEEN CONSTANT AND VARIABLE VISCOSITY PREDICTIONS FOR THE CONSTANT FILM CASE (CV: CONSTANT VISCOSITY BASED ON AVERAGE TEMPERATURE PREDICTED THROUGHOUT DOMAIN, VV: WORKING VARIABLE VISCOSITY MODEL)

$\epsilon = 2.0 \times 10^{-4}$	$Gr = 0.2628$	$Br = 2.1527 \times 10^{-3}$	$\Omega_* = -1$
$R_* = 1.3$	$p_o^* = -1.4747 \times 10^{-4}$	$\chi_1 = 0.4$	$\chi_2 = 0.2$
$\theta_o = 0.1$	$K_1^* = 165.83$	$K_2^* = 0.663$	$K_3^* = 1.5$
$N_r = 31$	$N_\theta = 31$	$N_z = 31$	$m = 4.6384$

Table 5.5: CONSTANT PARAMETERS FOR RESULTS PRESENTED IN SECTION 5.3.1

$\epsilon = 2.0 \times 10^{-4}$	$Gr = 0.2628$	$Br = 2.1527 \times 10^{-3}$	$\Omega_* = -1$
$R_* = 1.3$	$p_o^* = -7.3735 \times 10^{-2}$	$\chi_1 = 0.4$	$\chi_2 = 0.2$
$\theta_o = 0.1$	$K_1^* = 165.83$	$K_2^* = 0.663$	$K_3^* = 1.5$
$N_r = 31$	$N_\theta = 31$	$N_z = 31$	$m = 4.6384$
$S = 6.7810$			

Table 5.6: CONSTANT PARAMETERS FOR RESULTS PRESENTED IN SECTION 5.3.2

$h_g^*$		$Q_r^*$	$F_z^*$	$F_{\theta,0}^*$	$F_{\theta,h}^*$	$F_{p,h}^*$	$M_F^*$	$\mu_F$	$T_{max}^*$
				$\times 10^2$	$\times 10^2$	$\times 10^3$	$\times 10^2$	$\times 10^2$	
0	CV	0.1472	0.7282	0.1569	-0.1569	0.000	0.1824	0.2154	1.163
	VV	0.1742	0.7134	0.1294	-0.1294	0.000	0.1494	0.1840	1.113
0.5	CV	0.2440	0.7282	0.1476	-0.1323	-0.1530	0.1716	0.2027	1.098
	VV	0.2734	0.7178	0.1296	-0.1161	-0.1345	0.1499	0.1805	1.076
1.0	CV	0.4245	0.7282	0.1458	-0.1157	-0.3009	0.1695	0.2002	1.060
	VV	0.4571	0.7212	0.1336	-0.1060	-0.2760	0.1548	0.1853	1.051
2.0	CV	1.142	0.7282	0.1419	-0.0993	-0.4264	0.1650	0.1949	1.045
	VV	1.166	0.7260	0.1378	-0.0964	-0.4144	0.1601	0.1899	1.043

Table 5.7: RESULTS FOR SECTION 5.3.2 (VV - VARIABLE VISCOSITY, CV - CONSTANT VISCOSITY)

$$\begin{aligned}
R_o &= 6.5 \times 10^{-2} \text{ m} & R_i &= 5.0 \times 10^{-2} \text{ m} & h_o &= 1.0 \times 10^{-5} \text{ m} & \Omega_d &= -100.0 \frac{\text{rad}}{\text{s}} \\
p_o &= 1.0 \text{ MPa} & \rho &= 920.0 \frac{\text{kg}}{\text{m}^3} & \chi_1 &= 0.4 & \chi_2 &= 0.2 \\
k &= 0.14 \frac{\text{W}}{\text{mK}} & k_s &= 60.0 \frac{\text{W}}{\text{mK}} & k_f &= 35.0 \frac{\text{W}}{\text{mK}} & k_b &= 60.0 \frac{\text{W}}{\text{mK}} \\
\theta_o &= 0.1 \text{ rad} & c &= 2.0 \frac{\text{kJ}}{\text{kgK}} & T_o &= 450.0 \text{ K} & T_\infty &= 450 \text{ K} \\
N_r &= 13 & N_\theta &= 19 & N_z &= 21 & h_\infty &= 800.0 \frac{\text{W}}{\text{m}^2\text{K}} \\
L_s &= 1.5 \times 10^{-3} \text{ m} & L_f &= 1.0 \times 10^{-3} \text{ m} & L_b &= 5.0 \times 10^{-4} \text{ m}
\end{aligned}$$

Table 5.8: CONSTANT PARAMETERS FOR RESULTS PRESENTED IN SECTION 5.4

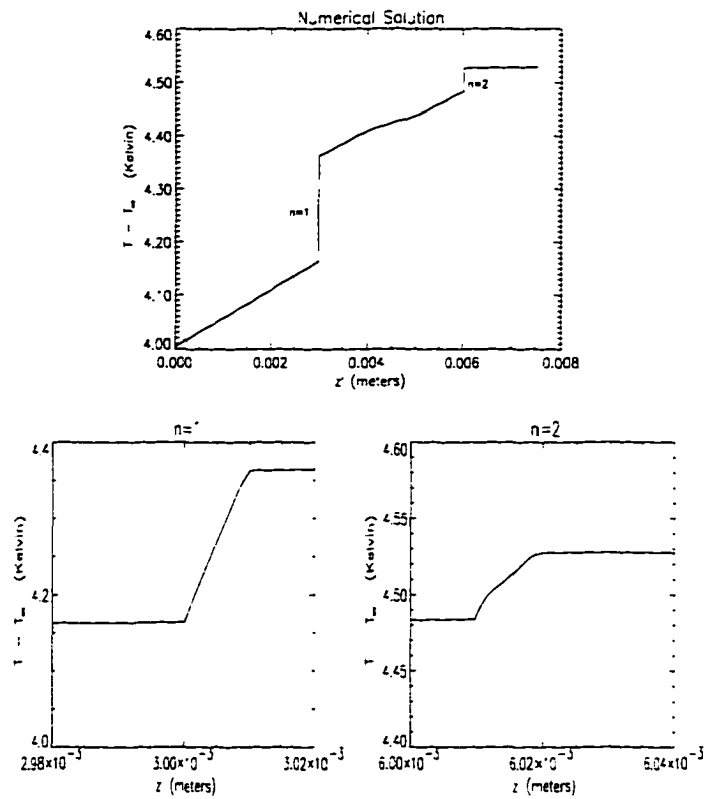


Figure 5.41: Numerical Assembly Temperature Distributions at  $r = R_o$  and  $\theta = 0$  with variable viscosity,  $\frac{p_i}{p_o} = 2$ , and  $\frac{h_g}{h_o} = 0.5$ .

Input Parameters	Maximum Temperature $T_{max}, (K)$	Moment $\mathcal{M}_F, (N - m)$
$\frac{p_i}{p_o} = 1, \frac{h_g}{h_o} = 0, CV$	466.14	0.989
$\frac{p_i}{p_o} = 2, \frac{h_g}{h_o} = 0, CV$	457.27	0.989
$\frac{p_i}{p_o} = 2, \frac{h_g}{h_o} = 0.5, CV$	454.68	0.923
$\frac{p_i}{p_o} = 2, \frac{h_g}{h_o} = 0, VV$	456.90	0.957
$\frac{p_i}{p_o} = 2, \frac{h_g}{h_o} = 0.5, VV$	452.74	0.904

Table 5.9: SUMMARY OF CLUTCH PERFORMANCE (VV - VARIABLE VISCOSITY, CV - CONSTANT VISCOSITY)

## CHAPTER 6

### CONCLUSIONS AND RECOMMENDATIONS

This discussion of the conclusions and recommendations is presented in two sections. In the first section, the results presented in the previous chapter are briefly discussed and critically reviewed. In the second section, recommendations for future research are presented in two parts: experimental research and theoretical research. In the experimental part, benefits and foreseeable difficulties in correlating the hydrodynamic theory are discussed. In the theoretical part, incremental model improvements as well as boundary and mixed film lubrication theories are discussed.

#### 6.1 Discussion of Results

In the previous chapter, results were presented for (1) the constant film, variable viscosity case, (2) groove studies including cavitation and noncavitation, and (3) the conjugate multiple disk model. These results are discussed and critically reviewed below.

In the constant film, variable viscosity case an isoviscous analytic solution was presented for the hydrodynamic variables,  $v_r$ ,  $v_\theta$ ,  $v_z$ , and  $p$ , while a simplified form of the energy equation was given for the temperature,  $T$ . This solution was used to highlight the effects of variable viscosity on six clutch performance parameters (radial flow rate, normal load, frictional force, frictional torque, friction coefficient, and maximum temperature rise) while varying four operating conditions (film thickness, inlet

temperature, radial pressure difference, and relative angular velocity). In general, the results' trends agreed with the expectations of the isoviscous case. Exceptions in the trends were accounted for using arguments involving the viscosity-temperature relation. Further, a limited study comparing variable and constant viscosity models was given for the constant film case. A bulk viscosity, based on the nodal average lubricant temperature was used for the isoviscous results presented. It was found that the difference between the variable viscosity results and isoviscous results was negligible.

In the groove studies, the effects of Gumbel's cavitation assumption on load carrying capacity were presented as functions of Sommerfeld number and dimensionless groove depth. In the noncavitation results, eight dimensionless parameters (radial flow rate, normal load, tangential force due to viscous shearing on the separator plate, tangential force due to viscous shearing on the friction plate, tangential force due to pressure, frictional torque, coefficient of friction, and maximum temperature) were studied as functions of dimensionless groove depth. In both cavitating and noncavitating parts, results were presented for variable and constant viscosity.

Gumbel's cavitation assumption is based on assuming that the film length decreases appropriately in the ambient region such that the continuity equation is satisfied. In such a scenario, the no-slip boundary conditions are inappropriate in the ambient region. Such arguments attacking this ad hoc model are noteworthy. Most importantly, the continuity and momentum equations are elliptic in this formulation. Any change in the nature of the solution will influence the solution throughout

the domain. In other words, setting predicted subambient pressures equal to zero should influence the positive pressures. Gumbel's assumption ignores the nature of the governing equations.

A more general critique of the groove studies concerns the model's claim to handle an arbitrary film thickness. Consider the isoviscous Reynolds equation for this problem:

$$r \frac{\partial}{\partial r} \left( r h^3 \frac{\partial p}{\partial r} \right) + \frac{\partial}{\partial \theta} \left( h^3 \frac{\partial p}{\partial \theta} \right) = 6 \Omega_d \mu_o r^2 \frac{\partial h}{\partial \theta},$$

which may be obtained by integrating the radial and angular momentum equations with respect to  $z$ , enforcing the no-slip boundary conditions on  $v_r$  and  $v_\theta$ , integrating the continuity equation from  $z = 0$  to  $z = h$ , integrating the continuity equation from  $z = 0$  to  $z = h$ , enforcing the no-slip boundary conditions on  $v_z$ , and invoking Leibnitz's integration rule. For a specified film thickness,  $h = h(r, \theta)$ , the above equation is a linear partial differential equation in  $p$ . To guarantee existence and uniqueness the coefficients of the pressure derivatives must be continuous within the domain. This implies that the film thickness must be continuous and differentiable,  $C^1$ , to guarantee a unique solution. Nevertheless, solutions presented in this dissertation which violate this criteria predict smoothly varying pressure distributions in subdomains where  $h$  is  $C^1$ . It is at discontinuities in film thickness where the pressure gradient is not continuous. In conclusion, we note the following constraint on the film thickness for lubrication problems: if the pressure gradient in the direction across the film is taken to be zero, the film shape must be  $C^1$  in order to predict a smoothly varying pressure distribution.

In the multiple disk solutions, two coupled lubrication problems were solved using a straightforward iterative technique. Temperature profiles were presented for grooves and no grooves, variable and constant viscosity, and finite and zero radial convection. The results clearly indicate that the clutch temperature can be significantly reduced with grooves and larger radial pressure gradients. However, the cost of this temperature reduction is a decreased torque level.

While the model shows how this lubrication theory may be used to model multiple disk clutch engagement, a critique is that the problem is fairly cumbersome for only two steady state, scaled lubrication problems. At each iteration level, two lubrication problems are solved which include solving for the pressure, velocity components, and temperature iteratively using the viscosity-temperature relation as a constraint equation. In reality, the physical problem could be significantly more complicated requiring a more robust model. Some suggestions are recommended in the following section.

## **6.2 Recommendations**

The following recommendations for future research are presented in two parts: experimental and theoretical. Recommendations in experimental studies are suggested via stating benefits of correlating theoretical and experimental data. Foreseeable problems in the experimental method are also mentioned. Theoretical recommendations include incremental model improvements as well as mixed and boundary lubrication theory models.



### 6.2.1 Recommendations in Experimental Studies

Before this hydrodynamic theory can be used to model actual clutch engagement, experimental and theoretical data must be correlated. Benefits of such a correlation include the establishment of a range of validity of the theory, as well as discovering new insights concerning the physical problem which may lead to improvements in the model.

The range of validity of this model is restricted in many ways. If the temperature is in excess of  $600\text{ K}$ , the lubricant will vaporize. As the film thickness gets smaller, surface roughness and eventually asperity contact become important. On the other hand, as the film gets larger, different terms, other than those included in this model, become increasingly important in the governing equations. If the pressure falls below the ambient pressure, surface tension and compressibility effects become important. Obviously it would be beneficial to establish a range of validity for this model.

However, a price must be paid to establish such a range. Foreseeable problems in establishing an experimental to theoretical correlation include fixing the experimental domain conditions (film thickness, inlet temperature, inner and outer clutch pressures, slip speed, etc.) to coincide with the input conditions of the theory, as well as installing the measuring components. Fixing the domain conditions is not simple. Setting the radial pressure difference,  $p_d$ , and the film thickness,  $h$ , are two examples. Some type of measuring device, such as pressure transducer, would need to be installed at or near the inner and outer clutch radii. Information would likely need to be acquired remotely for two reasons: (1) the plates move with a relative speed and (2)

splines located at the inner and outer clutch plate radii and connecting hub severely complicate installation. An alternative to pressure measurement would be flow rate measurement. This might be easier depending on instrument availability, cost, and installation. In any case, it should be possible to back out the pressure difference from the measured flow rate using this theory. Fixing and measuring the film thickness are also complicated issues. Perhaps fixing the film size could be accomplished by fabricating separator rings similar to those found in rotating disk couplings [63]. The use of shims would not be recommended for two reasons: clutch plates have a relative motion and the shim's presence would disrupt the flow field. The relative motion of the plates complicates measuring the film size. A distinction between the grooves and the lands of the friction plates should be recognizable. An alternative to film thickness measurement would be torque measurement. Here, strain gages could be installed, the torque could be measured, and the film thickness could be obtained from the theory.

### **6.2.2 Recommendations in Theoretical Studies**

This discussion of the theoretical recommendations is divided into two parts: incremental model improvements as well as mixed and boundary lubrication models. The incremental model improvements part focuses on previous criticisms, while the boundary and mixed film part highlights the relevant mechanisms to be included in future studies and lists pertinent references.

## Incremental Model Improvements

Posing the hydrodynamic theory with additional terms in the governing equations, further boundary and initial conditions, and further constraint conditions would certainly be an improvement from a physical standpoint. Obviously, a greater effort from a computational perspective as well as a theoretical development perspective would be required. Perhaps the most critical benefit of such an exercise would be to show under what conditions the existing theory is valid.

The philosophy used to obtain this dissertation's mathematical model used the following line of reasoning: (1) state a governing set of equations, (2) nondimensionalize the governing equations using the appropriate scales, and (3) transform the nondimensional equations into a domain of manageable form. Clearly, by comparing the final conditions in Equations (3.44) and (3.57), information is lost when the film thickness gradient is infinite. In such a scenario, special treatment should be given to the nondimensional scales and the geometrical domain transformation.

Some of the shortcomings with the existing cavitation model have been discussed. Some recommendations are given here. As a first approach it is recommended to allow for compressibility. This would require an additional equation of state relating the pressure, temperature, and density. Hamrock [22] cites two such equations relating the pressure and density for mineral oils. A second approach would be to use a boundary condition formulation similar to those developed by Swift and Steiber [22, 18], Coyne and Elrod [11], or Birkhoff and Hays [7] for one dimensional pressure distributions. In all of these cases, one could argue that this involves the additional specifications

of a surface tension condition, a flow rate condition, and a gas to liquid interface location condition. It is unknown whether any of the above methods have been generalized to accommodate two dimensional pressure distributions as assumed in this model. A third approach would be to examine the entire three dimensional problem. Here, additional terms in the Navier-Stokes equations and boundary conditions are appropriate. Ryskin and Leal [51, 52, 53] discuss these types of problems in two dimensions.

More efficient iterative procedures, such as Newton's method, exist and could certainly be implemented to satisfy the nonlinearity present due to the viscosity-temperature relation. Similarly, the coupled lubrication problem's iteration procedure could be solved using a Newton-Raphson method. In general, several iterative procedures could be incorporated to improve efficiency by accelerating convergence.

### 6.2.3 Boundary and Mixed Film Lubrication Models

The friction coefficients predicted by this hydrodynamic theory are too low to adequately describe clutch performance. For the simplest case, the friction coefficient increases with decreasing film size as indicated by Equation (5.12). To give an idea of the friction coefficient magnitude predicted by this theory, take  $\Omega_d = 100 \frac{rad}{s}$ ,  $\mu_o = 0.104 \frac{Ns}{m^2}$ ,  $R_o = 0.065 m$ ,  $R_i = 0.05 m$ ,  $h_o = 1.0 \times 10^{-5} m$ , and  $p_i = p_o = 2 \times 10^6 Pa$ . From Equation (5.12), we have  $\mu_F = 0.03$ . First it is noted that this friction coefficient is approximately an order of magnitude larger than typically predicted using this model. This is because (1) the viscosity is based on a small temperature, 293 K, for SAE 10, (2) the slip speed is high, and (3) the film

is small. Notwithstanding, it is noted that the predicted friction coefficient is still nearly an order of magnitude below typical clutch operating conditions,  $\mu_F \approx 0.1 - 0.3$  [32]. To remedy this shortcoming, boundary and mixed film lubrication models are recommended.

As the minimum film size decreases below the clutch plate surface roughness,  $h_o < \sigma$ , boundary lubrication is an applicable theory. Only a limited number of theoretical models have been constructed for this regime of lubrication largely because the friction is nearly completely dependent on the chemistry of the boundary and the lubricant. However, according to Bhushan [6], improvements in computer hardware, increasingly clever algorithms, and recent developments in modeling interatomic interactions are having major impacts on the chemical sciences. This is evidenced by his discussion on molecular dynamic computer simulations. Nevertheless, usually one relies on simple models to describe friction in this regime. For example, in the boundary lubrication regime the normal load is transferred by asperity contact. High wear rates result from such contacts. Models such as the Archard Wear Law [30] are used to describe wear. This model is considered ad hoc because the dominant wear mechanism, such as adhesion, abrasion, or fatigue is rarely discernible [8, 30].

Between the hydrodynamic and boundary lubrication regimes,  $1 < \frac{h_o}{\sigma} < 3$ , lies the mixed lubrication regime. Here, the normal load between surfaces is transferred from one surface to another by both asperity contact and the pressurized lubricant. In general, the friction mechanisms depend on both the chemistry and bulk properties of the lubricant. Unlike the boundary regime, wear is relatively low. Several

mixed film lubrication clutch models, which include surface roughness effects and/or asperity contact, are present in the literature [3, 38, 39, 69]. Models which only include the effect of surface roughness should be incorporated to describe the transition between contacting and noncontacting regimes. However, to predict realistic friction coefficients, it is recommended to include both asperity contact and surface roughness in a mixed lubrication model.

As it stands, the hydrodynamic lubrication theory presented in this dissertation for disk clutches is an integral part of a broader tribology problem. In order to incorporate this theory into the larger problem, first one must take the non-trivial step of modeling asperity contact as indicated above. This will both (1) increase the clutch temperature given realistic operating conditions and (2) increase the predicted friction coefficient. Towards this end, a serious review of contact mechanics [33] is recommended. Second, one must determine the limits of each of the theories. In previous discussions, it was indicated that the film thickness is not known *a priori*. Rather, the normal load, treated as a derived quantity in this dissertation, is known. Typically, given a load, the film thickness is obtained iteratively by solving boundary, mixed, and hydrodynamic lubrication problems. The appropriate regime is determined by comparing the predicted film thickness to the surface roughness.

## APPENDIX A

This appendix will give the derivation of Equation (3.60) using Equations (3.57) and (3.59). For convenience, both equations are restated here:

$$\begin{aligned}
 T_* \Big|_{z_b^*=1} &= T_* \Big|_{z_f^*=0}, & T_* \Big|_{z_f^*=L_f^*+1-h_*} &= T_* \Big|_{z_*=h_*}, \\
 T_* \Big|_{z_s^*=1} &= T_* \Big|_{z_*=0}, & \frac{\partial T_*}{\partial z_b^*} \Big|_{z_b^*=0} &= \frac{\partial T_*}{\partial z_s^*} \Big|_{z_s^*=0} = 0, \\
 \frac{k_b^* L_f^* \partial T_*}{k_f^* L_b^* \partial z_b^*} \Big|_{z_b^*=1} &= \frac{\partial T_*}{\partial z_f^*} \Big|_{z_f^*=0}, & \frac{k_s^* \partial T_*}{L_s^* \partial z_s^*} \Big|_{z_s^*=1} &= \frac{\partial T_*}{\partial z_*} \Big|_{z_*=0}, \\
 \frac{k_f^* \partial T_*}{L_f^* \partial z_f^*} \Big|_{z_f^*=L_f^*+1-h_*} &= -\frac{\partial T_*}{\partial z_*} \Big|_{z_*=h_*},
 \end{aligned} \tag{A.1}$$

$$T_* = C_1^f(r_*, \theta_*) z_f^* + C_2^f(r_*, \theta_*),$$

$$T_* = C_1^b(r_*, \theta_*) z_b^* + C_2^b(r_*, \theta_*), \tag{A.2}$$

$$T_* = C_1^s(r_*, \theta_*) z_s^* + C_2^s(r_*, \theta_*).$$

Substituting the expressions for the temperature fields given in Equation (A.2) into the eight expressions given by (A.1), we have

$$C_1^b + C_2^b = C_2^f, \tag{A.3}$$

$$C_1^f (L_f^* + 1 - h_*) + C_2^f = T_* \Big|_{z_*=h_*}, \tag{A.4}$$

$$C_1^s + C_2^s = T_* \Big|_{z_*=0}, \tag{A.5}$$

$$C_1^b = 0, \tag{A.6}$$

$$C_1^s = 0, \tag{A.7}$$

$$\frac{k_b^* L_f^*}{k_f^* L_b^*} C_1^b = C_1^f, \tag{A.8}$$

$$\frac{k_s^*}{L_s^*} C_1^s = \frac{\partial T_*}{\partial z_*} \Big|_{z_*=0}, \quad (A.9)$$

$$\frac{k_f^*}{L_f^*} C_1^f = -\frac{\partial T_*}{\partial z_*} \Big|_{z_*=h_*}. \quad (A.10)$$

Here, we have eight linear algebraic equations in the ten unknowns:  $C_1^b$ ,  $C_2^b$ ,  $C_1^f$ ,  $C_2^f$ ,  $C_1^s$ ,  $C_2^s$ ,  $T_* \Big|_{z_*=0}$ ,  $T_* \Big|_{z_*=h_*}$ ,  $\frac{\partial T_*}{\partial z_*} \Big|_{z_*=0}$ , and  $\frac{\partial T_*}{\partial z_*} \Big|_{z_*=h_*}$ , which are in general functions of  $r_*$  and  $\theta_*$ . Treating  $T_* \Big|_{z_*=0}$  and  $T_* \Big|_{z_*=h_*}$  as known quantities, the solution to the remaining eight unknowns is as follows:

$$C_1^b = C_1^s = C_1^f = \frac{\partial T_*}{\partial z_*} \Big|_{z_*=0} = \frac{\partial T_*}{\partial z_*} \Big|_{z_*=h_*} = 0, \quad (A.11)$$

$$C_2^b = C_2^f = T_* \Big|_{z_*=h_*}, \quad (A.12)$$

$$C_2^s = T_* \Big|_{z_*=0}. \quad (A.13)$$

From Equation (A.11), the adiabatic conditions listed in Equation (3.60) are evident.

From (A.12) and (A.13), we see that the temperature distribution in both the backing

and friction materials is  $T_* = T_* \Big|_{z_*=h_*}$ , and in the temperature distribution in the

separator plates is  $T_* = T_* \Big|_{z_*=0}$ .



## APPENDIX B

This appendix gives the derivation of the variable viscosity Reynolds equation. This derivation is based on the validity of Equations (3.45)-(3.48) and (3.54). For convenience, these equations are presented in dimensional form here:

$$\frac{\partial (rv_r)}{\partial r} + \frac{\partial v_\theta}{\partial \theta} + r \frac{\partial v_z}{\partial z} = 0, \quad (B.1)$$

$$\frac{\partial p}{\partial r} = \frac{\partial}{\partial z} \left( \mu \frac{\partial v_r}{\partial z} \right), \quad (B.2)$$

$$\frac{1}{r} \frac{\partial p}{\partial \theta} = \frac{\partial}{\partial z} \left( \mu \frac{\partial v_\theta}{\partial z} \right), \quad (B.3)$$

$$\frac{\partial p}{\partial z} = 0, \quad (B.4)$$

$$\text{on } z = 0 : \quad v_r = v_z = 0, \quad v_\theta = \Omega_d r, \quad (B.5)$$

$$\text{on } z = h(r, \theta) : \quad v_r = v_\theta = v_z = 0.$$

First, Equation (B.1) is integrated from  $z = 0$  to  $z = h$ :

$$\int_0^h \left[ \frac{\partial (rv_r)}{\partial r} + \frac{\partial v_\theta}{\partial \theta} + r \frac{\partial v_z}{\partial z} \right] dz = 0. \quad (B.6)$$

Making use of Leibnitz's rule and enforcing the no-slip conditions given in Equation (B.5), Equation (B.6) may be written as follows:

$$\frac{\partial}{\partial r} \left( r \int_0^h v_r dz \right) + \frac{\partial}{\partial \theta} \left( \int_0^h v_\theta dz \right) = 0. \quad (B.7)$$

Second, the velocity components,  $v_r$  and  $v_\theta$ , are obtained. From Equation (B.4), the pressure is independent of  $z$ . This allows one to integrate Equations (B.2) and (B.3) with respect to  $z$  holding  $\frac{\partial p}{\partial r}$  and  $\frac{\partial p}{\partial \theta}$  fixed. Enforcing the no-slip conditions

again, the velocity components may be written as follows:

$$v_r = \frac{\partial p}{\partial r} \left[ \int_0^z \frac{z'}{\mu} dz' - \frac{\int_0^h \frac{z}{\mu} dz}{\int_0^h \frac{1}{\mu} dz} \int_0^z \frac{1}{\mu} dz' \right], \quad (B.8)$$

$$v_\theta = \frac{1}{r} \frac{\partial p}{\partial \theta} \left[ \int_0^z \frac{z'}{\mu} dz' - \frac{\int_0^h \frac{z}{\mu} dz}{\int_0^h \frac{1}{\mu} dz} \int_0^z \frac{1}{\mu} dz' \right] + \Omega_d r \left[ 1 - \frac{\int_0^z \frac{1}{\mu} dz'}{\int_0^h \frac{1}{\mu} dz} \right]. \quad (B.9)$$

Third, the integrals in Equation (B.7) may be found using Equations (B.8) and (B.9):

$$\begin{aligned} \int_0^h v_r dz &= \frac{\partial p}{\partial r} \left[ \int_0^h \int_0^z \frac{z'}{\mu} dz' dz - \frac{\int_0^h \frac{z}{\mu} dz}{\int_0^h \frac{1}{\mu} dz} \int_0^h \int_0^z \frac{1}{\mu} dz' dz \right], \\ \int_0^h v_\theta dz &= \frac{1}{r} \frac{\partial p}{\partial \theta} \left[ \int_0^h \int_0^z \frac{z'}{\mu} dz' dz - \frac{\int_0^h \frac{z}{\mu} dz}{\int_0^h \frac{1}{\mu} dz} \int_0^h \int_0^z \frac{1}{\mu} dz' dz \right] \\ &\quad + \Omega_d r \left[ h - \frac{\int_0^h \int_0^z \frac{1}{\mu} dz' dz}{\int_0^h \frac{1}{\mu} dz} \right]. \end{aligned}$$

Finally, substituting these expressions into (B.7), the variable viscosity Reynolds equation is as follows:

$$\begin{aligned} &r \frac{\partial}{\partial r} \left( r \frac{\partial p}{\partial r} \left[ \int_0^h \int_0^z \frac{z'}{\mu} dz' dz - \frac{\int_0^h \frac{z}{\mu} dz}{\int_0^h \frac{1}{\mu} dz} \int_0^h \int_0^z \frac{1}{\mu} dz' dz \right] \right) \\ &\quad + \frac{\partial}{\partial \theta} \left( \left[ \int_0^h \int_0^z \frac{z'}{\mu} dz' dz - \frac{\int_0^h \frac{z}{\mu} dz}{\int_0^h \frac{1}{\mu} dz} \int_0^h \int_0^z \frac{1}{\mu} dz' dz \right] \right) \\ &= -\Omega_d r^2 \frac{\partial}{\partial \theta} \left[ h - \frac{\int_0^h \int_0^z \frac{1}{\mu} dz' dz}{\int_0^h \frac{1}{\mu} dz} \right]. \end{aligned} \quad (B.10)$$

For the isoviscous case,  $\mu = \mu_o$ , Equation (B.10) simplifies to the following expression:

$$r \frac{\partial}{\partial r} \left( r h^3 \frac{\partial p}{\partial r} \right) + \frac{\partial}{\partial \theta} \left( h^3 \frac{\partial p}{\partial \theta} \right) = 6 \Omega_d \mu_o r^2 \frac{\partial h}{\partial \theta}.$$

## APPENDIX C

This appendix will give the velocity, pressure, and stream function for an arbitrary film shape. Emphasis is placed on the continuity and differentiability of film shapes. The simplified lubrication problem studied here is two-dimensional and isoviscous. The relevant governing equations and boundary conditions are taken as follows:

$$\begin{aligned}
 \text{mass :} \quad & \frac{\partial u}{\partial x} + \frac{\partial w}{\partial z} = 0, \\
 x\text{-momentum :} \quad & \frac{\partial p}{\partial x} = \mu \frac{\partial^2 u}{\partial z^2}, \\
 z\text{-momentum :} \quad & \frac{\partial p}{\partial z} = 0, \\
 \text{no - slip conditions :} \quad & \text{on } z = 0 : \quad u = U, \quad w = 0, \\
 & \text{on } z = h(x) : \quad u = w = 0. \\
 \text{pressure conditions :} \quad & \text{on } x = 0 : \quad p = p_o, \\
 & \text{on } x = L : \quad p = p_o.
 \end{aligned}$$

Here the velocity is specified on the surfaces  $z = 0$  and  $z = h(x)$ , and the pressure is specified at the inlet,  $x = 0$ , and the outlet,  $x = L$ . Since the pressure and film thickness depend on  $x$  only, partial derivatives will be replaced by ordinary derivatives where appropriate.

The  $x$ -component of velocity may be stated in terms of the pressure gradient as follows:

$$u = \frac{1}{2\mu} \frac{dp}{dx} (z^2 - hz) + U \left(1 - \frac{z}{h}\right).$$

To obtain the pressure, it is convenient to use the following integral form of the continuity equation:

$$\frac{\partial}{\partial x} \int_0^h u \, dz = \frac{d}{dx} \left[ -\frac{h^3}{12\mu} \frac{dp}{dx} + \frac{Uh}{2} \right] = 0,$$

which may be written as the following Reynolds equation:

$$\frac{d}{dx} \left( h^3 \frac{dp}{dx} \right) = 6\mu U \frac{dh}{dx}.$$

The  $z$ -component of velocity may be obtained from the continuity equation:

$$w = -\frac{1}{2\mu} \left[ \frac{d^2 p}{dx^2} \left( \frac{z^3}{3} - \frac{hz^2}{2} \right) - \frac{dp}{dx} \frac{dh}{dx} \frac{z^2}{2} \right] - \frac{Uz^2}{2h^2} \frac{dh}{dx}.$$

Streamlines may be obtained once a stream function has been defined. A suitable stream function may satisfy the following conditions:

$$\frac{\partial \psi}{\partial z} = u, \quad -\frac{\partial \psi}{\partial x} = w.$$

The stream function for this generalized lubrication problem is as follows:

$$\psi = \frac{1}{2\mu} \frac{dp}{dx} \left( \frac{z^3}{3} - \frac{hz^2}{2} \right) + U \left( z - \frac{z^2}{2h} \right).$$

Clearly, the velocity components and stream function depend on the film thickness, pressure, and their derivatives.

In order to justify some of the statements made at the end of Chapter 4, consider the following continuous, non-differentiable film shape:

$$h = \begin{cases} s_h \left( 1 - \frac{x}{nL} \right) + h_o & ; \quad 0 \leq x \leq nL \\ h_o & ; \quad nL \leq x \leq L \end{cases}.$$

This is shown in Figure C.1. The pressure may be found in each continuous zone using the Reynolds equation. Since the Reynolds equation is a second order differential equation, two boundary conditions must be supplied for each zone. This requires a total of four conditions. The standard assumptions [18, 22] are to require continuity of flow rate per unit length and pressure as additional conditions.

$$p|_{x=nL^+} = p|_{x=nL^-},$$

$$\left[ \frac{h^3}{12\mu} \frac{dp}{dx} + \frac{hU}{2} \right]_{x=nL^+} = \left[ \frac{h^3}{12\mu} \frac{dp}{dx} + \frac{hU}{2} \right]_{x=nL^-}.$$

Given these conditions, the pressure may be stated in parts as follows:

$$P(X) = \begin{aligned} & 6n \left[ \frac{1}{1 + H_o - \frac{X}{n}} \right. \\ & \left. - \frac{H_o(1 + H_o)(-1 - H_o + n)}{(-2 - 4H_o - 2H_o^2 + 2n + 3nH_o) \left(1 + H_o - \frac{X}{n}\right)^2} \right] \quad ; \quad 0 \leq X \leq n \\ & \left. + \frac{2 + H_o - 2n}{-2 - 4H_o - 2H_o^2 + 2n + 3nH_o} \right] \\ & \frac{6n(X - 1)}{H_o(-2 - 4H_o - 2H_o^2 + 2n + 3nH_o)} \quad ; \quad n \leq X \leq 1 \end{aligned}$$

where,

$$P = \frac{(p - p_o) s_h^2}{\mu UL}, \quad X = \frac{x}{L}, \quad H_o = \frac{h_o}{s_h}.$$

We find that the pressure and its derivative are continuous at  $x = nL$ . Further, the velocity,  $u$ , and stream function,  $\psi$ , are continuous. However, the  $z$ -component of velocity is not continuous across  $x = nL$ . These results are in keeping with the general remarks at the end of Chapter 4. Streamlines using a dimensionless stream function,  $\psi_* = \frac{\psi}{s_h U}$ , with  $n = 0.7$  and  $H_o = 1.0$ , are given in Figure C.2. Here,  $Z = \frac{z}{s_h}$ .

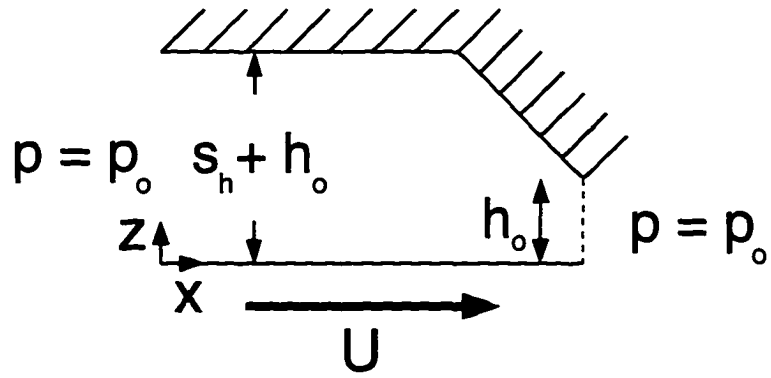


Figure C.1: Continuous, non-differentiable film shape

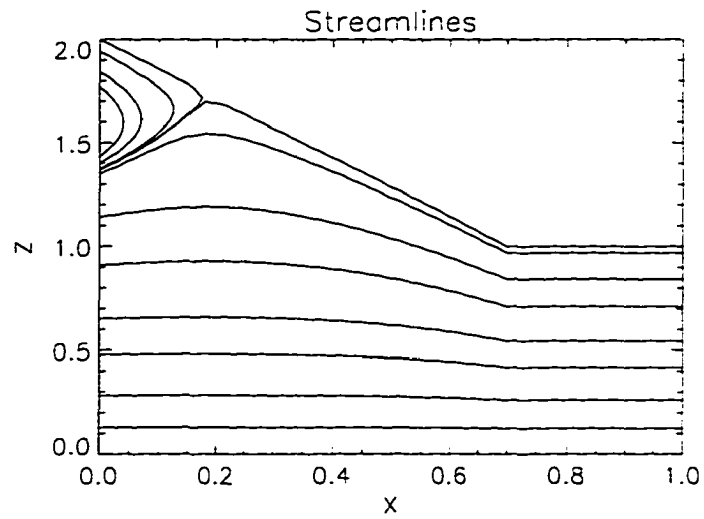


Figure C.2: Dimensionless streamlines using  $n = 0.7$  and  $H_o = 1.0$

## BIBLIOGRAPHY

- [1] Barcilon, V. and Pedlosky, J. (1967) "Linear theory of rotating stratified fluid motions," *Journal of Fluid Mechanics*, vol. 29, part 1, pp. 1-16.
- [2] Barcilon, V. and Pedlosky, J. (1967) "On the steady motion produced by a stable stratification in a rapidly rotating fluid," *Journal of Fluid Mechanics*, vol. 29, pp. 673-690.
- [3] Bardzimasvili, N. G. and Yashvili, S. G. (1987) "Study of Multi-disk Oil Friction Clutch Engagement," *Soviet Journal of Friction and Wear*, vol. 8, no. 2, pp. 57-64.
- [4] Batchelor, G. K. (1967) *An Introduction to Fluid Dynamics*, Cambridge University Press, Cambridge.
- [5] Batchelor, G. K. (1951) "Note on a Class of Solutions of the Navier-Stokes Equations Representing Steady Rotationally-Symmetric Flow," *The Quarterly Journal of Mechanics and Applied Mathematics*, vol. 4, pp. 29-41.
- [6] Bhushan, Bharat (1995) *Handbook of Micro/Nano Tribology*, CRC Press, Boca Raton.
- [7] Birkhoff, G. and Hays, D. F. (1963) "Free Boundaries in Partial Lubrication." *Journal of Mathematical Physics*, vol. 42, no. 2, pp. 126-138.
- [8] Briscoe, B. J. and Evans, P. D. (1989) "The Influence of Asperity Deformation Conditions on the Abrasive Wear of Gamma Irradiated Polytetrafluoroethylenes," *Wear*, vol. 133, pp. 47-64.
- [9] Chew, J. W. (1985) "Computation of convective laminar flow in rotating cavities," *Journal of Fluid Mechanics*, vol 153, pp. 339-360.
- [10] Cole, J. A. (1974) "Taylor Vortices with Short Rotating Cylinders," *Journal of Fluids Engineering*, vol. 96, pp. 69-70.
- [11] Coyne, J. C. and Elrod, H. G. (1971) "Conditions for the Rupture of a Lubricating Film - Part 2 New Boundary Conditions for Reynolds Equation," *Journal of Lubrication Technology*, Series F, pp. 156-167.
- [12] Di Prima, R. C. and Swinney, H. L. (1985) "Instabilities and Transition in Flow Between Concentric Rotating Cylinders," *Hydrodynamic Instabilities and the Transition to Turbulence*, H. L. Swinney and J. P. Gollub, eds., pp. 139-180, Springer, Berlin.
- [13] Dorinson, A. and Ludema, K. C. (1985) *Mechanics and Chemistry in Lubrication* Elsevier Science Publishers B. V., Amsterdam.
- [14] Eringen, A. C. (1967) *Mechanics of Continua*, Wiley, New York.
- [15] Evans, G. and Grief, R. (1987) "A Numerical Model of the Flow of Heat Transfer in a Rotating Disk Chemical Vapor Deposition Reactor," *Journal of Heat Transfer*, vol. 109, pp. 928-935.

- [16] Fletcher, C. A. J. (1991) *Computational Techniques for Fluid Dynamics*, vol. 1. Springer-Verlag, Berlin.
- [17] Fletcher, C. A. J. (1991) *Computational Techniques for Fluid Dynamics*, vol. 2. Springer-Verlag, Berlin.
- [18] Gross, W. A. and Matsch, L. A. and Castelli, V. and Eshel, A. and Vohr, J. H. and Wildmann, M. (1994) *Fluid Film Lubrication*, John Wiley & Sons, New York.
- [19] Gümbel, L. and Everling, E. (1925) *Reibung und Schmierung im Maschinenbau*. M. Drayn, Berlin, 1925.
- [20] Guo, Z. Y. and Zhang, C. M. (1992) "Thermal drive in centrifugal fields - mixed convection in a vertical rotating cylinder," *International Journal of Heat and Mass Transfer*, vol. 35, no. 7, pp. 1635-1644.
- [21] Hadid, A. H. (1993) "Chaotic flow in rotating lid cavities," *Physics of Fluids A*, vol. 5, no. 8, pp. 1939-1947.
- [22] Hamrock, B. J. (1994) *Fundamentals of Fluid Film Lubrication*, Mc-Graw Hill, New York.
- [23] Hamrock, B. J. and Jacobson, B. O. (1984) "Elastohydrodynamic Lubrication of Line Contacts," *ASLE Transactions*, vol. 27, no. 4, pp. 275-287.
- [24] Hersey, M. D. (1966) *Theory and Research in Lubrication*, John Wiley and Sons Inc., New York.
- [25] Hirsch, C. (1988) *Numerical Computation of Internal and External Flows*, vol. 1, John Wiley and Sons, Chichester.
- [26] Høglund, E. and Jacobson, B. (1986) "Experimental Investigation of the Shear Strength of Lubricants Subjected to High Pressure and Temperature," *Journal of Tribology*, vol. 108, pp. 571-578.
- [27] Homsy, G. M. and Hudson, J. L. (1969) "Centrifugally driven thermal convection in a rotating cylinder," *Journal of Fluid Mechanics*, vol. 35, part 1, pp. 33-52.
- [28] Houpert, L. G. and Hamrock, B. J. (1986) "Fast Approach for Calculating Film Thicknesses and Pressures in Elastohydrodynamically Lubricated Contacts at High Loads," *Journal of Tribology*, vol. 108, no. 3, pp. 411-420.
- [29] Hussain, A. and Biswas, S. and Athre, K. (1992) "A new viscosity-temperature relationship for liquid lubricants," *Wear*, Vol. 156, pp. 1-18.
- [30] Hutchings, I. M. (1992) *Tribology: Friction and Wear of Engineering Materials*. CRC Press, Boca Raton.
- [31] Ichihashi, T. (1994) "Recent Developments in Lubricating Oils for Wet Clutches and Brakes," *Japanese Journal of Tribology*, vol. 39, no. 12, pp. 1461-1470.
- [32] Ito, H. and Fujimoto, K. and Eguchi, M. and Yamamoto, T. (1993) "Friction Characteristics of a Paper-Based Facing for a Wet Clutch under a Variety of Sliding Conditions," *STLE Tribology Transactions*, vol. 36, no. 1, pp. 134-138.
- [33] Johnson, K. L. (1985) *Contact Mechanics*, Cambridge University Press, London.



- [34] Johnson, K. L. and Tevaarwerk, J. L. (1977) "Shear behaviour of elastohydrodynamic oil films," *Proceedings of the Royal Society of London A.*, vol. 356, pp. 215-236.
- [35] Lance, G. N. and Rogers, M. H. (1962) "The axially symmetric flow of a viscous fluid between two infinite rotating disks," *Proceedings of the Royal Society of London A.*, vol. 266, pp. 109-121.
- [36] Millsaps, K. and Pohlhausen, K. (1952) "Heat Transfer by Laminar Flow From a Rotating Plate," *Journal of Aeronautical Sciences*, vol. 19, pp. 120-126.
- [37] Minkowycz, W. J. and Sparrow, E. M. and Schneider, G. E. and Pletcher, R. H. (1988) *Handbook of Numerical Heat Transfer*, John Wiley and Sons, New York.
- [38] Natsumeda, S. and Miyoshi, T. (1994) "Numerical Simulation of Engagement of Paper Based Wet Clutch Facing," *Transactions of the ASME*, vol. 116, pp. 232-237.
- [39] Osani, H. and Ikeda, K. and Kato, K. (1990) "Relations Between Temperature in Friction Surface and Degradation of Friction Materials During Engaging of Wet Friction Paper," *SAE Transactions*, vol. 99, sect. 6, pp. 724-731.
- [40] Panton, R. L. (1984) *Incompressible Flow*, Wiley, New York.
- [41] Patir, N. and Cheng, H. S. (1978) "An Average Flow Model for Determining Effects of Three-Dimensional Roughness on Partial Hydrodynamic Lubrication," *ASME Journal of Lubrication Technology*, vol. 100, pp. 12-17.
- [42] Patir, N. and Cheng, H. S. (1979) "Application of Average Flow Model to Lubrication Between Rough Sliding Surfaces," *ASME Journal of Lubrication Technology*, vol. 101, pp. 220-230.
- [43] Payvar, P. (1991) "Laminar heat transfer in the oil groove of a wet clutch" *Int. J. Heat Mass Transfer.*, vol. 34, no. 7, 1792-1798.
- [44] Payvar, P. and Lee, Y. N., and Minkowycz, W. J. (1994) "Simulation of heat transfer to fluid flow in radial grooves of friction pairs," *International Journal of Heat and Mass Transfer*, vol. 37, pp. 313-319.
- [45] Pearson, C. E. (1965) "Numerical solutions for the time-dependent viscous flow between two rotating coaxial disks," *Journal of Fluid Mechanics*, vol. 21, pp. 623-633.
- [46] Peyret, R. and Taylor, T. D. (1983) *Computational Methods for Fluid Flow*, Springer-Verlag, New York.
- [47] Quast, P. and Smith, A. (1993) "Experimental Design and Analysis of Clark-Hurth Clutch Systems", Technical Report, University of Notre Dame, Notre Dame, Indiana.
- [48] Robertson, B. J. (1935) *An Investigation of Motor Oils*. (Bulletin of the University of Minnesota, Engineering Experimental Station, Bulletin No. 10), Minneapolis.

- [49] Robertson, B. J. (1936) *Motor Oils for Winter Use*. (Bulletin of the University of Minnesota, Engineering Experimental Station, Bulletin No. 11), Minneapolis.
- [50] Roelands, C. J. A. (1966) *Correlational Aspects of the Viscosity-Temperature-Pressure Relationship of Lubricating Oils*, Druk, V.R.B., Groingen, Netherlands.
- [51] Ryskin, G. and Leal, L. G. (1984) "Numerical solution of free-boundary problems in fluid mechanics. Part 1. The finite-difference technique," *Journal of Fluid Mechanics*, vol 148, pp. 1-17.
- [52] Ryskin, G. and Leal, L. G. (1984) "Numerical solution of free-boundary problems in fluid mechanics. Part 2. Buoyancy-driven motion of a gas bubble through a quiescent liquid," *Journal of Fluid Mechanics*, vol 148, pp. 19-35.
- [53] Ryskin, G. and Leal, L. G. (1984) "Numerical solution of free-boundary problems in fluid mechanics. Part 3. Bubble deformation in an axisymmetric straining flow," *Journal of Fluid Mechanics*, vol 148, pp. 1-17.
- [54] Schlichting, H. (1960) *Boundary Layer Theory*, McGraw Hill, New York.
- [55] Schulz, N. (1990) "Physical Relationship Between the Axial Gas-Lubricated Plain Bearings and a Clutch," *SAE Transactions*, vol. 99, sect. 2, pp. 567-580.
- [56] Scott, W. and Suntiwattana, P. (1995) "Effect of Oil Additives on the Performance of a Wet Friction Clutch Material," *Wear*, vol. 181-183, no. 2, pp. 850-855.
- [57] Shigley, J. E. (1977) *Mechanical Engineering Design*, Third Edition, McGraw Hill, New York.
- [58] Singh, H. and Gulati, I. B. (1986) "Influence of Base Oil Refining on the Performance of Viscosity Index Improvers," *Wear*, Vol. 118, pp 33-56.
- [59] Solt, M. B. (1990) "Optimizing Automatic Transmission Lining Load Distribution Using Finite Element Analysis," *SAE Transactions*, vol. 99, sect. 6, pp. 777-787.
- [60] Stebar, R. F. and Davison, E. D. and Linden, J. L. (1990) "Determining Frictional Performance of Automatic Transmission Fluids in a Band Clutch," *SAE Transactions*, paper no. 902146, vol. 99, sect. 4, pp. 914-927.
- [61] Stewartson, K. (1953) "On the Flow Between Two Rotating Coaxial Disks," *Proceedings of the Cambridge Philosophical Society*, vol. 49, pp. 333-341.
- [62] Sullivan, P. and Peroshin, V. and Hooke, C. (1992) "Application of a Three-Dimensional Surface Analysis System to the Prediction of Asperity Interaction in Metallic Contacts," *International Journal of Machine Tools and Manufacture*, vol. 32, no. 1-2, pp. 157-169.
- [63] Takemuro, T. and Niikura, Y. (1990) "An Analysis of Viscous Coupling Torque Transmission Characteristics and Hump Phenomenon," *SAE Transactions*, vol. 99, sect. 6, pp. 767-776.
- [64] Whittle, M. and Atkin, R. J. and Bullough, W. A. (1995) "Fluid dynamic limitations on the performance of an electrorheological clutch," *Journal of Non-Newtonian Fluid Mechanics*, vol. 57, pp. 61-81.

- [65] Wilkinson, W. L. (1960) *Non-Newtonian fluids, Fluid Mechanics, Mixing and Heat Transfer*, Pergamon Press, London.
- [66] Wilson, W. R. D. (1991) "Friction Models for Metal Forming in the Boundary Lubrication Regime," *Journal of Engineering Materials and Technology*, vol. 113, pp. 60-68.
- [67] Wirz, H. J. and Smolderen, J. J. (1978) *Numerical Methods in Fluid Dynamics*, McGraw-Hill, New York.
- [68] Yevtushenko, A. and Ivanyk, E. (1994) "Determination of heat and thermal distortion in braking systems," *Wear*, vol. 185, pp. 159-165.
- [69] Zagrodzki, P. (1990) "Analysis of thermo mechanical phenomena in multidisc clutches and brakes," *Wear*, vol. 140, pp. 291-308.
- [70] Zhu, D. and Cheng, H. S. (1988) "Effect of Surface Roughness on the Point Contact EHL," *Transactions of the ASME*, vol. 110, pp. 32-37.